論文 / 著書情報
Article / Book Information

題目(和文)	
Title(English)	Damage Limit States for Infill Walls Subjected to In-Plane Cyclic Loading
著者(和文)	付翔
Author(English)	Xiang Fu
出典(和文)	学位:博士（工学）, 学位授与機関:東京工業大学, 報告番号:甲第11831号, 授与年月日:2022年3月26日, 学位の種別:課程博士, 審査員:吉敷 祥一,元結 正次郎,河野 進,西村 康志郎,佐藤 大樹
Citation(English)	Degree:Doctor (Engineering), Conferring organization: Tokyo Institute of Technology, Report number:甲第11831号, Conferred date:2022/3/26, Degree Type:Course doctor, Examiner:,,,,
学位種別(和文)	博士論文
Type(English)	Doctoral Thesis

Damage Limit States for Infill Walls Subjected to In-Plane Cyclic Loading

A thesis submitted in partial fulfilment of
the requirements for the Degree of
Doctor of Engineering
by

Xiang Fu

Academic Supervisor:
Prof. Shoichi Kishiki

Graduate Major in Urban Design and Built Environment
Departments of Architecture and Building Engineering
School of Environment and Society
Tokyo Institute of Technology
Tokyo, Japan

February 2022

CONTENTS

1 INTRODUCTION

2 EXPERIMENTAL STUDY ON NON-STRUCTURAL LIGHT-GAUGE STEEL FRAME DRYWALL PARTITION

2.2 **Test Plan**

2.3 **Test Results**

2.4 **The Connection Between the Concrete Slab and Track of the LGS Wall**

3 EXPERIMENTAL STUDY ON MASONRY INFILLED TIMBER FRAMES

3.2 **Test Plan**

3.3 **Test Results**

3.4 **Discussions**

4 CONCLUSIONS

Abstract

Wall is a vertical component that is widely used in many types of constructions. According to their functionality, it can be classified as structural or non-structural walls. A typical structural wall is the shear wall, which is often constructed of reinforced concrete or steel plates nowadays. The purpose of structural walls is to resist gravity loads, overturning moments, as well as shear forces. On the other hand, the non-structural wall is usually used to separate a room. For non-structural walls, although their load-bearing capacity is not required, buildings may no longer be functional for entrance or may even need to be demolished as a result of the damage of non-structural components in recent earthquakes, even though the structural components remain intact. Such damage may prove to be a major burden on the economy. Accordingly, the importance of non-structural components in seismic performance is widely recognized by both researchers and practitioners. Light-Gauge-Steel partition (LGS partition) and masonry infilled wall are non-structural interior wall systems that are widely used in the construction market. The present study intends to characterize the in-plane seismic performance of infill walls, with light-gauge steel (LGS) partition drywalls and unreinforced masonry infill walls as research subject. To achieve the objective, a series of experimental tests were conducted by in-plane cyclic loading.

Firstly, Light-Gauge-Steel drywall is an interior non-structural partition system widely used for frame building across the globe. In Japan, this system is featured by the sliding track-stud connection of base frame. To investigate the in-plane seismic performance of a typical LGS partition constructed in accordance with Japanese practice. An experimental was conducted on Light-Gauge-Steel partition drywall (LGS partition). Fifteen LGS partition subassemblies were subjected to in-plane cyclic loading. Base on the test results, the characteristic points of the envelope curve are defined, in order to generate the performance level of the LGS partition. By evaluating the characteristic points, equations for their strength, stiffness, and story drift ratio are proposed. As a result, the prediction results from the equations of drift ratio lay on the safe side. The equations are then adopted to define the damage limit states. Moreover, the observed damage during the test is reported and correlated with the respective damage limit states.

Secondly, the use of masonry infills has been found to be one of the most appropriate solution to meet architectural needs because of the durability, fire resistance and sound insulation provided by the masonry, along with the ease-of-construction and cost-effectiveness. they are generally recognized as vulnerable to seismic activity and have often been observed in field experience after damaging earthquakes. In spite of the widespread recognition of the critical role of specific damage control measures for masonry infills, code procedures for determining whether the elements should be repaired and the design of new buildings contain only a limited number of recommendations for non-structural elements which are widely regarded as inadequate, incomplete or unclear. To investigate the seismic behavior of the structural system, six full-scale Chuandou timber frame subassemblies were subjected to in-plane cyclic loading, four of which were infilled with masonry walls. Base on the test results, the contribution of masonry infill is obtained by an approximate approach. The characteristic points of the envelope curve of masonry infill is defined, in order to generate the performance level of the masonry infill. By evaluating the characteristic points, equations for their strength, stiffness, and story drift ratio are proposed. The equations are then adopted to define the damage limit states. Moreover, the observed damage during the test is reported and correlated with the respective damage limit states.

Although two different construction systems are employed for gypsum board walls and masonry infill walls, they are both filled in the frame structure and both are compressed by the surrounding structural frame when subjected to horizontal loads. In the study of their seismic performance, it should be evaluated from their compression areas. In an LGS wall, the base frame does not contribute much to the lateral force since the studs may slide and its lateral force comes mainly from the compression damage of the gypsum board, which is a relatively uniform construction material, so the focus should only be on its effective compression area. On the other hand, the masonry infill wall is constructed from two materials, mortar and brick, each of which has highly variable material properties, with the complicated frame-panel interaction, making the evaluation of its load-carrying capacity challenging. In this study, its lateral force mainly comes from the weaker mortar of the two building material, while the strength of the brick has a certain contribution to its stiffness, so the failure areas corresponding to the two materials needs to be taken into account when considering the masonry infill wall. Finally, a case study is conducted to compare LGS partition wall and masonry infill wall. It is found that LGS partition is hardly damaged within the design limit, while masonry infill represent high initial stiffness.

Acknowledgements

Although writing is a solitary activity, research is not. During my five years of research in Tokyo Tech, I received support from many people, without whom this doctoral thesis would not have been possible. I would like to express my sincere thanks to many people who have assisted me in completing this thesis.

First of all, I would like to express my deepest appreciation to my supervisor, **Shoichi Kishiki**. Throughout my five years of studies, he has played a vital role in my growth as a researcher, teaching me a great deal of research knowledge ranging from the most basic definition of positive and negative signs to logical thinking about research topics, to how to write an attractive research proposal and how to make a fluent academic presentation. In many of the discussions, he not only helped me in clarifying my thoughts when I was perplexed, but also cheered me up when I was disheartened. He deeply influenced me with his great patience and extraordinary passion for research. It is a great honor to be his doctoral student.

I would like to sincerely thank the reviewers of this thesis: Prof. **Shojiro Motoyui**, Prof. **Susumu Kono**, Assoc. Prof. **Daiki Sato**, Assoc. Prof. **Koshiro Nishimura**. Thanks to them for their time and efforts in providing valuable advice concerning this thesis. It is especially grateful to Prof. **Kono** for his advice and guidance in areas that I did not understand very well, and he even spent several weekends with me in academic seminars and provided a series of important questions and suggestions for my research.

I would also like to thank the provider of the Chuandou project, Prof. **Zhe Qu** at the Institute of Engineering Mechanics, who provided me with a wonderful opportunity to learn more about the unique structure of my hometown. I would like to thank him for carrying out experiments with us during the heat wave in Beijing. Furthermore, I am grateful for his rapid critiquing and patient instruction regarding not only my study, but also my ability to write an English paper. His patience, enthusiasm, hard work, and optimism for research have deeply influenced me.

Thanks to Assistant Prof. **Nobuhiko Tatsumi** at Kishiki Lab. for patiently teaching me many research software and experimental equipment. His attentiveness to research is also of benefit to me. I would also like to thank Assoc. Prof. **Yang Xiang** at Tongji university for teaching me the knowledge about manuscript review. Prof. **Satoshi Yamada** at Tokyo University provided the valuable advice in the seminar and support in Los Angeles for international conference NCEE, is gratefully acknowledged.

Thanks to Assoc. Prof. **Takanori Ishida** at Yokohama National University for the advice in seminar and teaching me valuable interview experience when I was going to apply for the JSPS scholarship. I am grateful to Prof. **Yao Cui** at Dalian University of Technology for her support during my experiments in Beijing, and for providing advice with the Chuandou project. I would also like to express my sincere thanks to Assoc. Prof. **Yu Jiao** at Tokyo City University for her constant kindness, she not only helps me greatly in academics, but also looks after me during my study abroad period. she can listen to my concerns and provides various of applicable advice, which helps me feel at home in a foreign country.

I would also like to express my most sincere gratitude to the secretaries of the lab: **Otone Ibayashi**, secretary in Yamada lab, **Yuko Endo**, clerk in SOFTech, **Motoko Okubo** and **Eiko Nagami**, secretary in Kishiki Lab. It was appreciated that they helped me dealing with the documents of my business trips and experiments, as well as provided me warm care and encouragement regarding academic and life in Japan.

I am very grateful to all the students in Kishiki lab , Yamada lab at Tokyo tech, Qu lab at Institute of Engineering Mechanics and Cui lab at Dalian University of Technology. Without their excellent contributions and technical experiences, the designs and procedures on paper would not be realized. I really appreciate **Xiaoyu Yang**, we often discuss academic issues together, and he is always able to offer logical thinking suggestions. Meanwhile, he also helps me to improve my English writing and pronunciation. I am also grateful to **Shotaro Nakada** and **Miku Kurosawa**, as they are always willing to assist me with my experiments and can anticipate some of my work and process it. Also, I would like to thank **Haowen Zheng**, **Jiaxi Li**, **Yang Dong** and **Yuchen Liu** for not only supporting me a lot with my experiments, but also giving me valuable academic advice. I miss those days that we had “friendly” academic discussions. Thanks to **Thaileang Touch** for sharing some scholarship-related and job hunting -related information with me.

Finally, I appreciate my parents **Lifeng Fu** and **Bo Hou** for always being there for me. Thanks to their financial support and understanding throughout the years, as well as for providing me with the motivation and courage to keep moving forward. Moreover, I really appreciate my fiancée **Ziyuan Tang**, for all the support and concern. Thank her for being with me on this journey through thick and thin together. Her endless support has made me a stronger person.

February 2022
Xiang Fu

Notation

α = the amplification factor for bearing strength of the metal track

α' = the coefficients for Q_S

A_n = the net area of the mortar section

A_d = effective area of the equivalent diagonal strut of the masonry infill

B = the distance between the two transducers C1 and C2 in **Chapter 3**

c = clearance between the gypsum panels and loading frame

δ = deformation of the PAF specimen

δ_N = the uplift of the column base

d_{max} = deformation at the maximum strength

d_p = screw spacing of the inner layer

d_s = diameter of the PAF

d_{stud} = stud spacing of the base frame

d_y = deformation at the yield strength

D = the horizontal distance between the centroid of gravity force to the axis of the column

DL = dead load

Δ = the lateral displacement at the top-end of the wall

$\Delta_{C1\sim C6}$ = displacements recorded by corresponding displacement transducers

Δ_{CE} = the uplift at the east column bases

Δ_{CW} = the uplift at the west column bases

$\Delta_{D1\sim D6}$ = displacements recorded by corresponding displacement transducers

$\Delta_{E1\sim E9}$ = displacements recorded by corresponding displacement transducers

Δ_L = horizontal deformation of the wall

ΔL_d = the deformation of the equivalent diagonal strut of the masonry infill

Δ_{ro} = the rocking displacement

Δ_{se} = separation between the gypsum panel and loading frame

Δ_{slip} = lateral slip of gypsum panel

Δ_V = measured vertical displacement of the wall

ε_y = average strain at the point of σ_y

ε_u = average strain at the point of σ_u

E = elastic modulus of gypsum board

E_B = elastic modulus of the timber material coupon at bending test

E_C = elastic modulus of the concrete (or column of the frame)

E_{com} = elastic modulus of the timber material coupon at compression test

E_M = the elasticity modulus of masonry prism

F_C = design compression strength of the concrete

γ = the weight of concrete per volume

g = the dimension from the bottom of the head of the embedded pin to the top of the web of the metal track

G = the gravity force on the specimen including its self-weight and the additional gravity load on the top of the specimens and the masonry infill

h = the effective height of the compression side of the gypsum panel

h_0 = the height of the compression side of the gypsum panel

H = span height of the wall

H_f = the vertical distance from the lower pin to the upper pin

I_B = the moments of inertia of the timber beam

I_C = the moments of inertia of the timber column

j = the distance between axial force N and the reaction force

k_0 = clearance stiffness

k_1 = initial contact stiffness of the specimen

k_2 = secondary contact stiffness of the specimen

k_{CB} = the rotation stiffness of the column base joint

k_J = the rotation stiffness of the beam-column joint

k_{MI} = lateral stiffness of the masonry infill

λ_H = dimensionless parameter expressing the relative stiffness of the infill panel to the frame

l_e = the effective length of the gypsum panel

l_{em} = embedment length of the PAF

L = span length of the wall

L_d = length of the masonry panel diagonal line

L_f = the horizontal distance from the lower pin to the upper pin of LGS wall

L_P = length of the PAF

LL = live load

μ = average of the corresponding value

μ' = the coefficients for Q_S

μ_m = the coefficient of internal friction of the brick-mortar interface

M_{CB} = the moment of the column base

n = gypsum panel layer number

n_s = number of the stud of the base frame

N = axis force

p = deflection factor

θ = the diagonal angle of the panel

θ_{CB} = rotation angle of the column base joint

$Q\ (=V)$ = lateral force of the specimen

Q_B = the bearing strength of the metal track

Q_{BF} = lateral strength of the base frame

Q_d = the shear force of masonry infill transmitting along diagonal direction

Q_{max} = maximum strength of the specimen

Q_{MI} = lateral strength of the masonry infill

Q_P = pryout strength of the PAF

Q_{ro} = the lateral force corresponding to the initiation of rigid-body rocking

Q_u = ultimate strength of the specimen

Q_S = the shear strength of the masonry infill wall

Q_y = yield strength of the specimen

r = the radius of the circular column section

R = story drift ratio of the specimen

R_B = reaction force of the PAF in the opposite direction below the PAF

R_{BF} = story drift ratio of the specimen at the point where the intersection of clearance stiffness k_0 and contact stiffness k_1

R_{Qy} = story drift ratio of the specimen reached Q_y

R_{Qu} = story drift ratio of the specimen reached Q_u

R_{Qmax} = story drift ratio of the specimen reached Q_{max}

R_{ro} = rotation angle of the rocking

R_U = reaction force of the PAF in the forward side of the applied force on the concrete slab

σ_B = compression strength of the concrete in material test

σ_c' = the bearing compression strength

σ_m = compression strength of the mortar

σ_M = compression strength of the masonry prism

σ_N = the normal stress in the masonry panel

σ_u = mean of the ultimate compressive stress of the gypsum board of the grain in the perpendicular and parallel direction, equal to 0 in this study

σ_y = mean of the maximum compressive stress of the gypsum board of the grain in the perpendicular and parallel direction

s = standard deviation of the corresponding value

$\tau_0(=\tau)$ = the bond-slip strength of the masonry prism

t = wall thickness

t_B = gypsum board thickness

t_r = thickness of the metal track

$v_{te}\,(=\tau_{MI})$ = shear strength of the mortar joint

v_{me} = equivalent mortar shear strength

V = volume of the gypsum panel

w = the effective width of the diagonal strut

x = stress range of the R_U

x_0 = length of the compression side of the column base joint

1. Introduction

1.1 Background

A wall is a vertical component that is widely used in many types of constructions. According to their functionality, walls can be classified as structural or nonstructural. A typical structural wall is a shear wall, which is often constructed by using reinforced concrete or steel plates. The purpose of structural walls is to resist in-plane lateral force (e.g.: wind and seismic loads). These walls are very effective in reducing the deformation of buildings, which results in less damage to the nonstructural components. Various studies have been conducted to investigate the behavior of shear walls subjected to different load conditions. Riva P. et al.[1-1] conducted experimental tests on a full-scale reinforce concrete (RC) structural wall subjected to cyclic loading to investigate its load-carrying capacity. Tasnimi A.A. [1-2] conducted a series of tests of one- to eight-scale models of prototype shear walls subjected to cyclic loading and evaluated various indices of the wall specimens, such as crack pattern, strength, deformation, stiffness and stress distribution. Saeid S. et al.[1-3] developed a simple analytical model of steel plate shear walls through a theoretical study and verified it with the experimental results of previous studies. To summarize the research method of structural walls, many researchers have derived the results of each characteristic value (e.g., strength and stiffness) of their walls based on experiments and evaluated their capacity to resist horizontal loads through a series of theoretical analyses. For structural walls, it is crucial to ensure its load-bearing capacity.

On the other hand, non-structural walls are usually used to separate a room. For non-structural walls, although their load-bearing capacity is not needed, buildings may no longer be functional for access or may even need to be demolished as a result of the damage of these non-structural components in earthquakes, even though the structural components remain intact (Fig.1-1). Such damage may prove to be a major burden on the economy, considering the breakdown of the cost of office buildings, hotels, and hospitals, as reported by Taghavi et al. [1-5]. They found that interior construction is one of the significant sources of cost. Moreover, the damage of non-structural components results in economic losses and a threat to life safety[1-6]. Accordingly, the importance of non-structural components in seismic performance is widely recognized by both researchers and practitioners. A light-gauge-steel partition (LGS wall) is a non-structural interior wall system that is widely used in the construction market. This interior wall system may benefit from its lightweight and quick construction compared to heavier infill walls (e.g., clay bricks and concrete blocks). It consists of a base frame and gypsum board, and the base frame is made up of metal tracks, studs, and other metal components. However, design details (e.g., the construction method of the base frame, the number of layers of gypsum board, and the connection between gypsum board layers) differ from country to country. Several studies have been conducted on this partition system. In the early stages of LGS wall experimental studies, the emphasis has been on its load-carrying capacity under quasi-static loads, such as in investigations by Freeman[1-7], Rihal[1-8], and Asham et al.[1-9]. Recently, studies have begun to concentrate more on the damage of the LGS wall. Restrepo et al. [1-10] conducted several tests of LGS walls constructed in accordance with U.S. practice, in which the metal stud was fastened to the metal tracks at the top and bottom. Based on the observations, the damage limit state was defined and generally categorized into three stages. Davies et al. [1-11] conducted several tests in different wall configurations during which damage observations and a seismic fragility database were obtained. On the other hand, Magliulo et al. [1-12] evaluated an alternative LGS wall using shaking table tests. This system is characterized by a sliding track-stud joint, i.e., the stud is inserted into the metal track without using screws, and the gypsum panel clearances are prepared along the perimeter. As a result of the test, the seismic performance of the LGS wall can be substantially improved through the modification of the LGS wall. In other studies involving

Fig. 1-1. Damage of non-structural LGS wall during Kumamoto earthquake[1-4].

similar modified systems, in-plane cyclic loading tests were conducted by Tasligedik et al. [1-13], Pali et al. [1-14] and Mulligan et al. [1-15], who evaluated an LGS wall with a sliding joint and clearance between the panel and surrounding frame in accordance with their local construction practice. These researchers found the horizontal clearance between the wall and the frame to be an important factor affecting in-plane damage to the wall. To summarize the research method of non-structural walls, it has widely been recognized that specific measures are necessary to minimize damage to non-structural walls. In other words, for non-structural walls, it is essential to assess their structural drift demands and corresponding damage.

However, as a special type of wall, masonry infill walls have a wide range of applications around the world. These walls are commonly placed only after the surrounding frame is constructed, and several design codes classify them as non-structural components. However, the application of masonry infill walls is considered to increase the lateral resistance of some weak frames (e.g., timber frames). Although they can be used as earthquake resisting components, masonry infills are especially vulnerable to earthquakes and have been extensively observed in field experiences reported after damaging earthquakes, such as the 1999 Turkey earthquake[1-16], the 2003 Greece earthquake[1-16], the 2010 Haiti earthquake[1-17], and the 2013 Lushan earthquake in China[1-18] (Fig. 1-2). Several numerical and experimental investigations related to the seismic performance of masonry infilled frames have been previously conducted. Mansouri et al.[1-19] investigated the lateral behavior of low-shear strength masonry infilled reinforced concrete frames, and seismic indices such as strength and failure modes were discussed. An experimental investigation of the influence of the aspect ratio of masonry infill with RC frames was conducted by Schwarz S. et al.[1-20], who found that the influence of the aspect ratio on load-capacity appears to be small. Emami S. et al. [1-21] conducted a series of tests on masonry infilled steel frames and verified analytical methods to evaluate the stiffness of the masonry infill. As a summary of the infill wall research method, previous studies have focused on their load capacity.

Fig. 1-2. Damage to masonry-infilled timber frame after 2013 Lushan earthquake in China[1-18].

1.2 Statement of Problems

First, for non-structural partitioning, there have been many numerical and experimental studies related to the general seismic performance of LGS walls, especially the structural drift demand, but these studies have been focused on the analysis and assessment of partitions built in accordance with local construction practice. There are reports of significant differences in seismic performance among partitions constructed with the same construction techniques and materials in several LGS wall studies [1-11][1-14]; therefore, construction detail is recognized as a key issue. LGS walls have also been widely used in Japanese construction, but little research has been conducted on their seismic performance. In Japan, this system features the slip joint of the stud-track connection of the base frame. Lee et al. [1-22] conducted a series of cyclic loading tests to investigate the seismic performance of LGS walls used in typical Japanese buildings as well as the associated repair cost. Tamura et al. [1-23] performed several tests without clearance. These very few studies have rarely focused on the structural drift demands of LGS walls and the corresponding damage, which are widely regarded as one of the most critical paths for non-structural component research.

Second, masonry infills are generally recognized as vulnerable to seismic activity and have often been observed in field experience after damaging earthquakes. Despite the widespread recognition of the critical role of specific damage control measures for masonry infills, code procedures for determining whether the elements should be repaired and the design of new buildings contain only a limited number of recommendations for non-structural elements; these recommendations are widely regarded as inadequate, incomplete or unclear. As a consequence, in recent decades, a large number of investigations have been conducted with respect to the seismic performance of masonry infilled frames. However, many of the previous studies on masonry infill walls have used the method of studying structural walls; i.e., most of these studies have focused on their load-carrying capacity rather than their structural drift demands. In addition to these studies focusing on the seismic performance of masonry infills, a small number of studies have focused on their structural drift demand. Morandi P. et al.[1-24] investigated several specimens with hollow bricks subjected to in-plane cyclic loading and defined limit states of hollow masonry infill framed with RC members. Drift levels at the different limit states were evaluated. Reggia A. et al. [1-25] used a similar method to develop the performance level of insulating light weight fiber reinforced concrete infill. It should be noted, however, that previous studies have focused primarily on the analysis and assessment of RC frames and steel frames. Masonry infilled timber frames have been widely used for detached houses in seismic prone areas. These frames were reported to exhibit various levels of damage but did not easily collapse in past earthquakes [1-16]-[1-18]; however, in most cases, they were nonengineered and built following the local rules of thumb. Despite the different details of timber sections, joints and types of infills, infilled timber frames generally fall into two categories by their lateral load resisting systems. In a braced timber frame with infills, most lateral loads are resisted by single- or cross-diagonal timber braces, whereas the infills are provided primarily for thermo-hygrometric performance [Fig. 1-3(a)]. Many studies have been carried out on this category of infilled braced timber frames, including the Kay-Peyi in Haiti[1-17], Dhajji-Dewari in Kashmir[1-26], Paianta in Romania[1-27], Gaiola Pombalino in Lisbon[1-28][1-29], Pombalino in Portugal[1-30] and Himis in Turkey[1-31]. In the other category, the timber frames are bare frames without timber bracing and the lateral resistance is primarily provided by the infills [Fig. 1-3(b)]. Typical systems in this category include the Pombalino in Romania[1-32] and Baraccata in Italy[1-33]. In addition, there is a building system of timber frame infilled with blay brick masonry, namely Chuandou timber frames, fall into the latter category [Fig. 1-3(c)]. This system is distinguished by the following features: (1) the timber beams and columns are joined by penetration tenons, where the full section of a beam goes through the mortise on the column; (2) it uses no timber braces but is infilled with masonry or wood panels as the partitions; and (3) the columns stand freely on independent base stones, and there are neither sills nor mechanical anchors at the column bases. Although a considerable number of papers have reported on timber frame buildings, most of them have focused on architectural

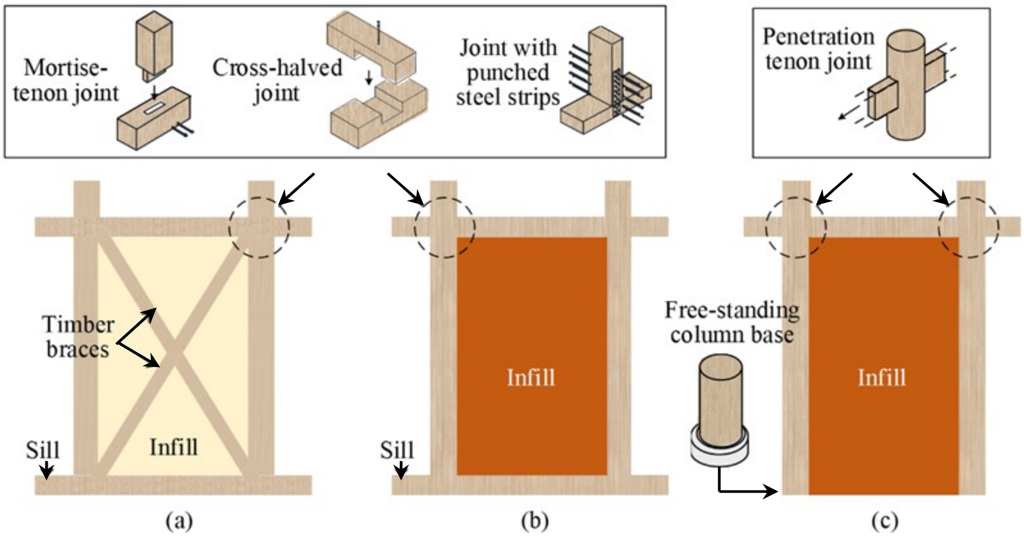

Fig. 1-3. Comparison of masonry-infilled timber frame buildings: (a) braced masonry-infilled timber frame, (b) masonry-infilled timber frame, (c) Chuandou timber frame.

forms, and only a very few studies have focused on seismic performance. In general, compared to RC frames and steel frames, little is known about the horizontal load-carrying capacity and structural drift demands of timber frames with masonry infills.

The above two types of walls, non-structural walls and masonry infill walls, lack an understanding of their limitations with regard to the story drift ratio and corresponding damage. This study addresses these issues within the following scope.

1.3 Objectives and Scope of Research

For non-structural partition walls, in the present study, the in-plane seismic performance of light-gauge steel drywall partition (LGS wall) is characterized as a research subject. More specifically, the purpose of the study is to investigate the in-plane seismic performance of a typical LGS wall built in accordance with Japanese practice and to provide a quantitative definition of the related damage limit states based on the test results, particularly the drift ratio capacity of the system. In addition, the horizontal clearance between a gypsum panel and surrounding frame is regarded as an important factor for damage control of the LGS wall (Fig. 1-3); the clearance is usually set at 5-10 mm on Japanese construction sites in consideration of fire resistance and soundproofing. Thus, the scope of the research subject is listed as follows:

- LGS walls are surrounded by steel frames and are built following Japanese construction practice.
- The system features the slip joint of the stud-track connection of the base frame.
- The clearance is positioned horizontally between the structural frame and gypsum panel and ranges between 5 and 10 mm in width.

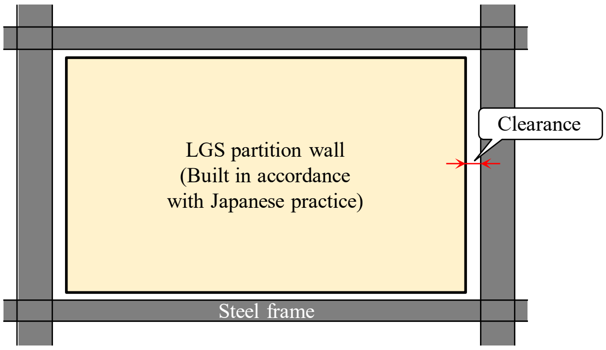

Fig. 1-4. LGS wall with clearance.

For the safe and efficient application of masonry infills, appropriate analysis and verification are of considerable importance, and safety checks of masonry infill for in-plane deformation are also an important subject. During the design of new buildings, it is necessary to understand the different levels of structural drift, representing relevant performance limit state conditions, to assess and verify the expected structural drift demands; these demands are associated with the extent of damage caused by in-plane actions [1-24]. Consequently, the evaluation of the load-carrying capacity and the structural drift demands for masonry infills is the research subject of this study. More specifically, this study focuses on an infilled frame that uses a solid clay brick or a solid concrete block without openings. No reinforcement (e.g., longitudinal steel) is adopted in the specimens; thus, the masonry infills for this study are limited to URM (unreinforced masonry). The scope of masonry infill is illustrated in Fig. 1-5. Regarding framing, this study is focused on timber-framed masonry infill walls, with some previous studies on RC- and steel-framed infill walls. Additionally, the scope of this study is limited to building structures that do not require diagonal bracing to simply understand their masonry infill wall contributions. Because a bare timber frame does not provide sufficient lateral strength, shear damage caused by mortar joints is regarded as the dominant pattern of damage for numerous masonry infill walls. Thus, the scope of the research subject is listed as follows:

- Masonry infill walls with mortar bond failure is the main damage pattern.
- The material of the frame is not limited; that is, the material can be timber, concrete or steel. However, the structure is limited to a form that can ensure that the load is transferred along the diagonal direction; thus, diagonal braces are not applied in this study.
- For specimens with masonry infill or not (i.e., bare frame), the failure modes of their frames are similar.

Additionally, a more detailed scope will be given in **Chapter 3**.

Although this study focuses on the in-plane seismic performance of non-structural and masonry infill walls, it is worth noting that these results must be combined with their out-of-plane limit states for practical application. The damage pattern of the frames of masonry infill walls, in particular, must be considered.

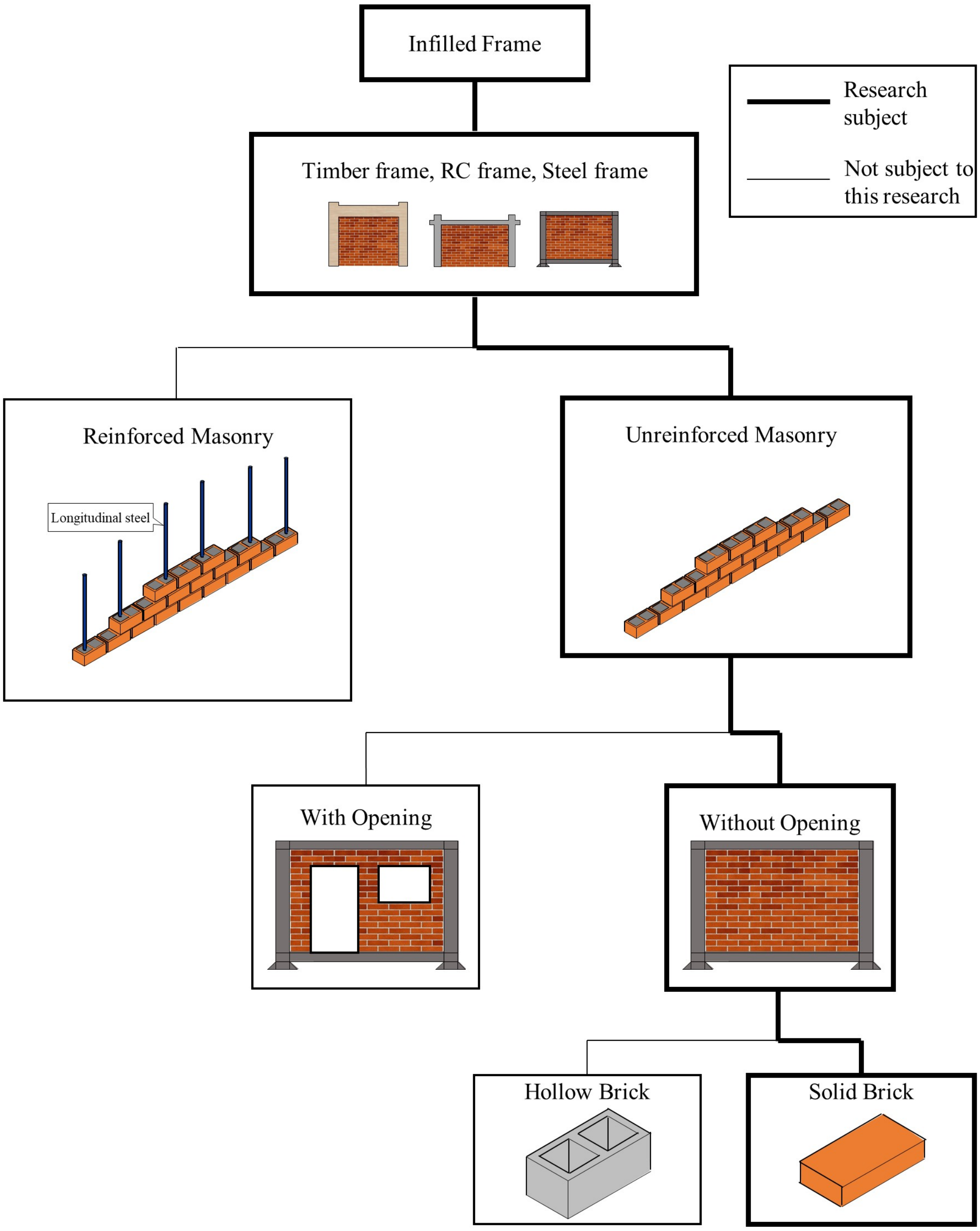

Fig. 1-5 Scope of the masonry infill.

1.4 Research scheme

In this study, in-plane static cyclic tests are conducted on full-scale, single-story, single-bay LGS walls in Japan and timber frames with masonry infill structures in China. Based on the test results, the characteristic points of the envelope curve are defined to generate the performance level of the wall. By evaluating the characteristic points, equations for the wall strength, stiffness, and story drift ratio are proposed. The equations are then adopted to define the damage limit states. Moreover, the observed damage during the test is reported and correlated with the respective damage limit states. The research scheme is illustrated in Fig. 1-6.

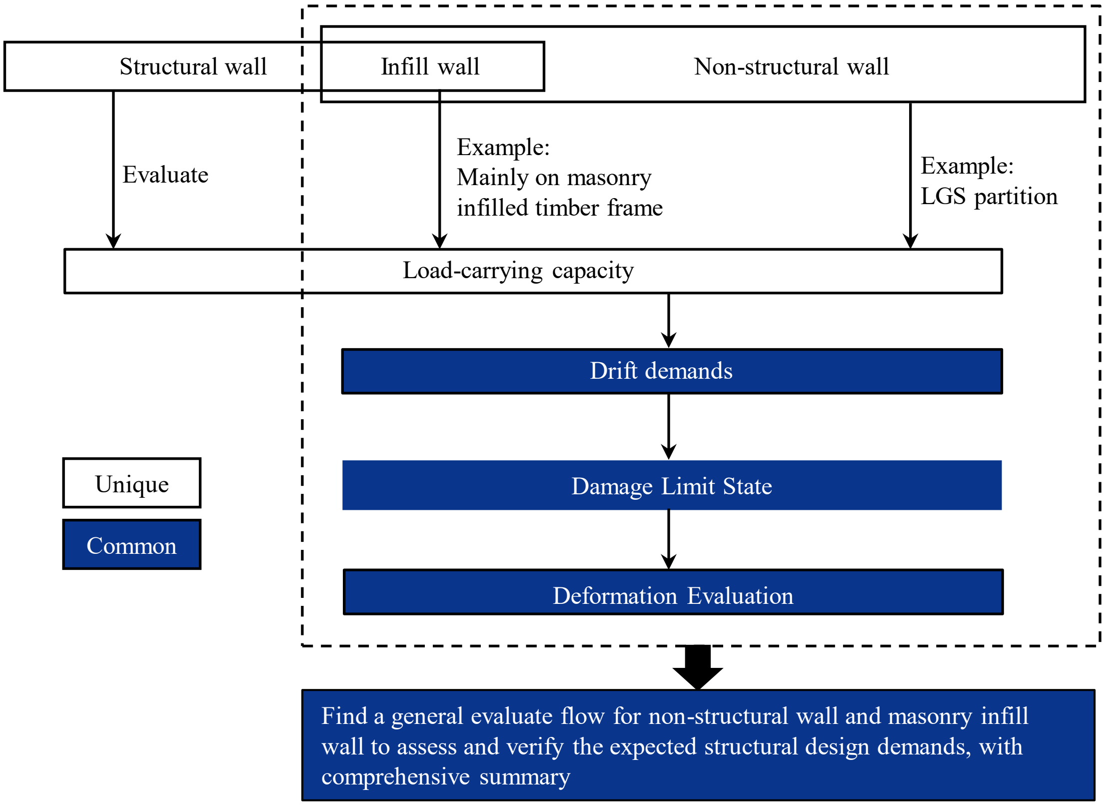

Fig. 1-6. Research scheme.

1.5 Systematics of the Thesis

The organization of this thesis is mainly divided into four chapters.

Chapter 1 provides an overview of the study. This chapter consists of background, statement of problems, objectives, scope, research scheme, and systematics of the thesis.

In **Chapter 2**, fifteen LGS wall subassemblies subjected to in-plane cyclic loading are tested. Based on the test results, the characteristic points of the skeleton curve are defined to generate the performance level of the LGS wall. By evaluating the characteristic points, equations for the strength, stiffness, and story drift ratio of the structure are proposed. The equations are then adopted to define the damage limit states. Moreover, the observed damage during the test is reported and correlated with the respective damage limit states.

In **Chapter 3**, six full-scale Chuandou timber frame subassemblies subjected to in-plane cyclic loading are tested, four of which are infilled with masonry walls. The observed failure modes are reported. An appropriate solution is adopted for obtaining the experimental stiffness and strength of the infill wall. The characteristic points of the skeleton curve of the infill wall are defined to generate the performance level of the infill wall. The expected structural drift demands, which are associated with the level of damage due to in-plane action, are evaluated after obtaining the strength and stiffness of the infill.

In **Chapter 4**, as a summary of all the obtained results, the developed performance level of the LGS wall and masonry infill wall is represented, and a simple design recommendation and the overall conclusion of non-structural walls and infill walls subjected to in-plane loading are reported.

Reference

[1-1] Riva P., Meda A., Giuriani E., Cyclic behaviour of a full scale RC structural wall, Engineering Structures, Volume 25, Issue 6, May 2003, pp. 835-845. https://doi.org/10.1016/S0141-0296(03)00020-8

[1-2] Tasnimi A., Strength and deformation of mid-rise shear walls under load reversal, Engineering Structures, Volume 22, Issue 4, April 2000, pp. 311-322. https://doi.org/10.1016/S0141-0296(98)00110-2

[1-3] Sabouri-Ghomi S., Ventura C., and Kharrazi M., Shear Analysis and Design of Ductile Steel Plate Walls, Journal of Structural Engineering, Volume 131, Issue 6, June 2005, https://doi.org/10.1061/(ASCE)0733-9445(2005)131:6(878)

[1-4] Building Research Institute, National Institute for Land and Infrastructure Management, 14th Survey report on damage to building caused by the 2016 Kumamoto earthquake, Nov., 2016 (in Japanese).

[1-5] Taghavi S. and Miranda E. Response Assessment of Nonstructural Building Elements. Report 2003/05, Pacific Earthquake Engineering Research (PEER) Centre, Berkley, p.64.

[1-6] Whittaker A., Soong T. An overview of non-structural research at three U.S. earthquake engineering research centers. Proceedings of seminar on seismic design, performance, and retrofit of non-structural components in critical facilities. Applied Technology Council, Multidisciplinary Center for Earthquake Engineering Research, 2003.

[1-7] Freeman S. Third progress report on racking tests of wall panels. Report JAB-99-54, University of California, Berkeley.

[1-8] Rihal S.S. Racking building tests of non-structural building partitions. Report ARCE R90-1, California Polytechnic State University, San Luis Obispo.

[1-9] Adham S., Avanessian V., Hart G., Anderson R., Elmlinger J. and Gregory J.. Shear wall resistance of lightgage steel stud wall systems. Earthquake Spectra, 6(1): 1-14. https://doi.org/10.1193/1.1585555

[1-10] Restrepo J. and Bersofsky A. Performance characteristics of light gage steel stud partition walls. Thin-walled Structures, 49(2): 317-324. https://doi.org/10.1016/j.tws.2010.10.001

[1-11] Davies R., Retamales R., Mosqueda G. and Filiatrault A. Experimental seismic evaluation, model parameterization and effects of cold-formed steel-framed gypsum partition walls on the seismic performance of an essential facility. Technical Report MCEER-11-0005, University at Buffalo, New York.

[1-12] Magliulo G., Petrone C., Capozzi V., Maddaloni G., Lopez P., and Manfredi G. Seismic

performance evaluation of plasterboard partitions via shake table tests. Bulletin of Earthquake Engineering, 12(4): 1657-1677. https://doi.org/10.1007/s10518-013-9567-8

[1-13] Tasligedik A., Pampanin S., and Palermo A. Low damage seismic solutions for non-structural drywall partitions. Bulletin of Earthquake Engineering, 13(4):1029-1050. https://doi.org/10.1007/s10518-014-9654-5

[1-14] Pali T., Macillo V., Terracciano M., Bucciero B., Fiorino L., and Landolfo R. In-plane quasi-static cyclic tests of non-structural lightweight steel drywall partitions for seismic performance evaluation. Earthquake Engineering and structural dynamics, 47(6): 1566-1588.

[1-15] Mulligan J., Sullivan T., and Dhakal R. Experimental study of the seismic performance of plasterboard partition walls with seismic gaps. Bulletin of Earthquake Engineering, 53(4): https://doi.org/175-188. 10.5459/bnzsee.53.4.175-188

[1-16] Langenbach, R.. From “Opus Craticium” to the “Chicago Frame”: earthquake resistant traditional construction.” Int J Archit Herit 2007;1:29-59.

[1-17] Vieux-Champagne F, Sieffert Y, Grange S, Polastri A, Ceccotti A, Daudeville L. Experimental analysis of seismic resistance of timber-framed structures with stones and earth infill. Eng Struct 2014;69:102-15.

[1-18] Qu Z, Dutu A, Zhong J, Sun J. Seismic damage to masonry-infilled timber houses in the 2013 M7.0 Lushan, China, Earthquake. Earthq Spectra 2015;31:1859-74.

[1-19] Mansouri A., Marefat M., and Khanmohammadi M., Experimental evaluation of seismic performance of low-shear strength masonry infills with openings in reinforced concrete frames with deficient seismic details, Struct. Design Tall Spec. Build. 23, 1190–1210 (2014), DOI: 10.1002/tal.1115

[1-20] Schwarz S., Hanaor A., Yankelevsky D., Experimental Response of Reinforced Concrete Frames With AAC Masonry Infill Walls to In-plane Cyclic Loading, Structures 3 (2015) 306–319, https://doi.org/10.1016/j.istruc.2015.06.005

[1-21] Emami S. and Mohammadi M., Effect of frame connection rigidity on the behavior of infilled steel frames, Earthquakes and Structures, Vol. 19, No. 4 (2020) 227-241 DOI: https://doi.org/10.12989/eas.2020.19.4.227

[1-22] Lee T., Kato M., Matsumiya T., Suita K. and Nakashima M. Seismic performance evaluation of non-structural components: Drywall partitions. Earthquake Engineering and Structural Dynamics, 36(3): 367-382. https://doi.org/10.1002/eqe.638.

[1-23] Tamura K., Kaneko M., Kambara H., Shiohara H., Terada T. Static Loading Tests on Partition walls with Light Gage Steel. Architectural Institute of Japan National Conference, Sep. 2006,

pp.985-986. (in Japanese)

[1-24] Morandi P., Hak S., Magenes G., Performance-based interpretation of in-plane cyclic tests on RC frames with strong masonry infills, Engineering Structures, Volume 156, 1 February 2018, pp. 503-521

[1-25] Reggia A., Morbi A., Preti M., Plizzari G., Lightweight FRC infill wall: in-plane and out-of-plane loading tests. Materials and Structures (2020) 53:135. https://doi.org/10.1617/s11527-020-01569-7

[1-26] Ali Q, Schacher T, Ashraf M, Alam B, Naeem A, Ahmad N et al. In-plane behavior of the Dhajji-Dewari structural system (Wooden braced frame with masonry infill). Earthq Spectra 2012;28:835-58.

[1-27] Dutu, A., Niste, M., Spatarelu, I., Dima, D. I., & Kishiki, S. Seismic evaluation of Romanian traditional buildings with timber frame and mud masonry infills by in-plane static cyclic tests. Engineering Structures 2018, 167(February), 655–670.

[1-28] Vasconcelos, G. et al., In-plane shear behaviour of traditional timber walls, Engineering Structures, 56, 1028–48.2013.

[1-29] Meireles, H., Bento, R., Cattari, S. and Lagomarsino, S. 2012. “A hysteretic model for frontal walls in Pombalino buildings”. Bulletin of Earthquake Eng., 10(5), 1481–502.

[1-30] Poletti, E., & Vasconcelos, G. Seismic behaviour of traditional timber frame walls: experimental results on unreinforced walls. Bulletin of Earthquake Engineering 2015, 13(3), 885–916.

[1-31] Gulkan P., Langenbach R. 2004. “The earthquake resistance of traditional timber and masonry dwellings in Turkey”. In 13th World Conference on Earthquake Engineering, Paper 2297, Vancouver, Canada.

[1-32] Dutu A, Sakata H, Yamazaki Y, Shindo T. In-plane behavior of timber frames with masonry infills under static cyclic loading. J Struct Eng 2016;142:04015140.

[1-33] Ruggieri, N., Tampone, G. and Zinno, R. 2015. “In-Plane Versus Out-of-Plane “Behavior” of an Italian Timber Framed System - The Borbone Constructive System: Historical Analysis and Experimental Evaluation”. Inter. Journal of Arch. Heritage, 9(6), 696-711.

2. Experimental Study on Non-structural Light-Gauge Steel Frame Drywall Partition

2.1 Introduction

The aim of the study is to investigate the in-plane seismic performance of a typical LGS wall built according to the Japanese practice and provide a qualitative definition of the related damage limit states based on the test results, particularly for the drift ratio capacity of the system. Fifteen full-scale specimens of single-story one-bay LGS walls were subjected to in-plane cyclic loading. Section 2.2 introduces the detailed experimental program such as the specimens, testing method. Section 2.3 mainly provides the observed damage during the test. Section 2.4 presents how to derive the damage limit state of LGS wall. The detailed information about the specimens, testing method, and main findings, including the failure mode and observed damage, is presented in the following sections.

2.2 Test Plan

2.2.1 Specimens

The configuration of the specimens that were designed and constructed in a laboratory according to the construction practice of LGS walls in Japan [2-1] is shown in Fig. 2-1. The building materials used in the construction of the specimens were made in accordance with the Japanese Industrial Standards (JIS) [2-2]. The specimens consisted of a base frame and gypsum panels [Fig. 2-1(a)]. All specimens had an identical height of H =1760 mm, taken as the distance from the bottom of the metal track to its top. Three different gypsum panel lengths were employed in this experiment to represent the S span (L= 2730 mm), M span (L= 3640 mm), or L span (L= 4550 mm) of the panel. (Fig. 2-2).

The base frame was constructed by inserting studs between the upper and lower metal tracks and attaching them to a bridging channel (Fig. 2-3). The bridging channel, which serves as a link between the studs, was positioned at a height of 1200 mm above the lower end of the studs. There were two standard spacings for the studs (303 mm and 455 mm) (Fig. 2-4). For the base frame (Fig. 2-5), both the upper and lower steel beams of the loading frame were fitted with metal tracks. According to the Japanese practice, metal tracks were fastened to the structural component at 900 mm intervals using a power-actuated fastener. However, to evaluate the in-plane seismic response of the LGS wall, the connection with the surrounding frame was designed to be intact, and the metal tracks were fixed to the loading frame using steel bolts

Gypsum panels are comprised of multiple gypsum boards. Two gypsum boards are typically used in Japan, namely, regular and reinforced gypsum boards. The reinforced board has a higher density and fire resistance than the regular board. For this study, reinforced gypsum boards with thicknesses t_B of 12.5 mm and 21 mm are used. The standard dimensions of these boards were 1820×910 mm and 1820×606 mm, respectively. Their size can be adjusted by cutting the board to fit the required size of the gypsum panel. The configuration of each specimen is shown in Fig. 2-6. According to the Japanese construction practice, gypsum panels can be fixed on one or both sides of the stud [Figs. 2-7(b) and (c)]. The gypsum panel on each side had two layers, an inner layer and an outer layer, and the layer connected to the base frame was called the inner layer, while the other layer was called the outer layer. The inner layer is introduced firstly, it (Fig. 2-1) was positioned horizontally, and the lower layer was named the lower panel, while the upper layer was named the upper panel. Layers were attached only to the studs of the base frame using self-tapping screws (M3.5×22 mm or M3.5×32 mm), depending on the thickness of the gypsum board, at standard spacings of 290 mm. The outer layer is then introduced, it was attached vertically to the inner layer using an adhesive (JIS 5538 [2-12]), 24 h of curing was applied

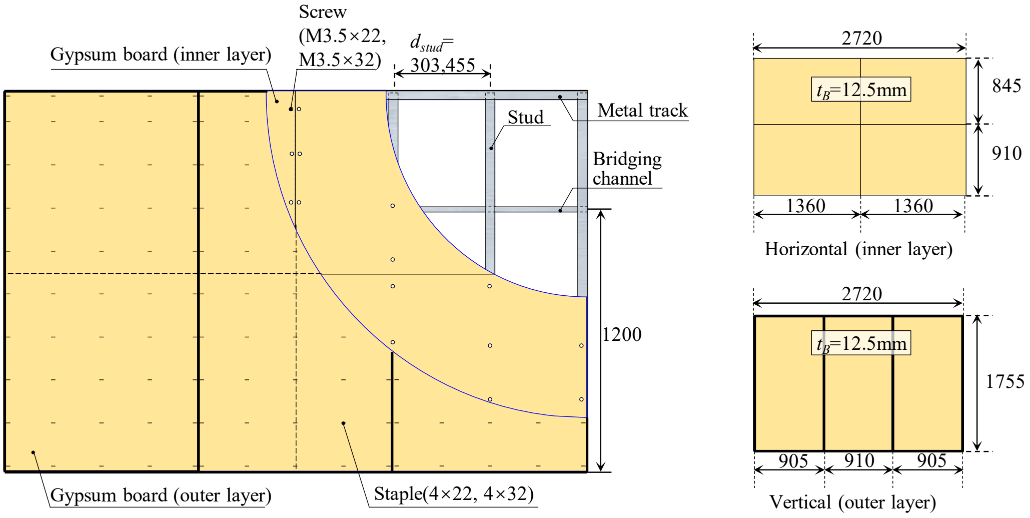

(a) (b)

Fig. 2-1 Specimen: (a) outline of specimen, (b) arrangement of gypsum board (Unit:mm).

to each specimen to combine the inner and outer layers to form a whole. Staples of 4 mm width and 22 mm or 32 mm height, depending on the thickness of the panel, were then used to fix the outer layer to the inner layer temporarily until the adhesive sets. The staples were fix at a spacing of approximately 200 mm. The configuration of the specimen with an S span gypsum panel is illustrated in [Fig. 2-1(b)]. In addition, there was a clearance (c = 5 mm) between the gypsum panels and loading frame, apart from the margin-bottom, which is designed to be directly attached to the loading frame. Although there is no stipulation on the clearance in the construction practice, it is usually set to 5–10 mm on construction sites in consideration of fire resistance and soundproofing. In most cases, the clearance of the inner layer is filled with insulation (e.g., mineral wool), and the clearance of the outer layer is sealed using an adhesive sealant. To observe the damage to the gypsum panel along the perimeter, no insulation or adhesive sealant was applied in this experiment (i.e.: the clearance remained empty).

The parameters of the experiment are listed as follows (Table 1): (1) span length was L= 2730, 3640, or 4550 mm, (2) screw spacing of the inner layer was d_p = 100 or 290 mm, (3) configuration of the inner layer gypsum panel was horizontal or vertical, (4) board thickness was t_B =12.5 or 21 mm, (5) number of panel layers were n =1, 2, or 4 (Fig. 2-7), and (6) stud spacing of the base frame was d_{stud} = 303 or 455 mm. Each parameter is briefly described below. For parameter (2), a comparison is made between the standard screw spacing (d_p = 290 mm) and modified spacing (d_p = 100 mm) in which the screw consumption is almost tripled compared with that of the standard spacing. As parameter (3), in the Japanese practice, the inner layer is usually placed horizontally, while a vertical specimen was designed to study the difference. The number of layers in parameter (5) had three configurations: one-sided single layer (n = 1) [Fig. 2-7(a)], one-sided double layer (n = 2) [Fig. 2-7(b)], and two-sided double layer (n

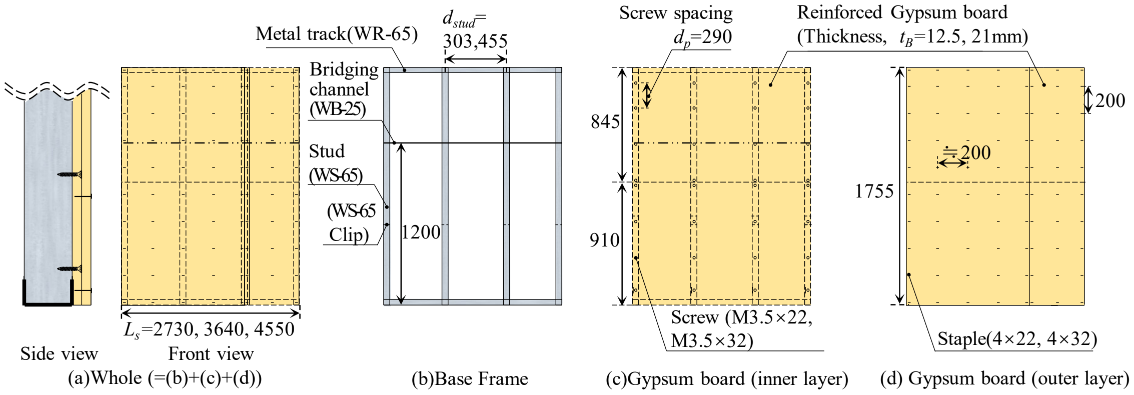

Fig. 2-2. Outline of specimen: (a) whole (=(b)+(c)+(d)), (b) base frame, (c) inner layer of gypsum board, (d) outer layer of gypsum board. (Unit: mm).

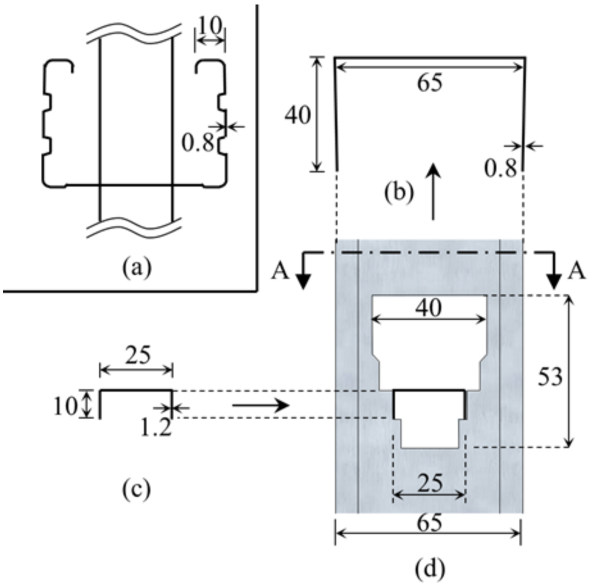

Fig. 2-3. Cross-sectional size of base frame materials: (a) section A-A, (b) metal track, (c) bridging channel, (d) hole for bridging channel on stud.

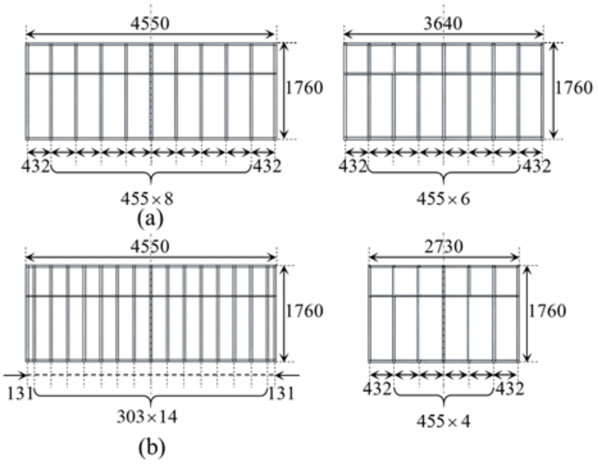

Fig. 2-4. Stud spacing in different span length: (a) L span @455 (b) L span @303, (c) M span @455, (d) S span @455 (unit: mm).

Fig. 2-5. Base frame.

= 4) [Fig. 2-7(c)], The Japanese practice usually uses n = 2 and n = 4, whereas several n = 1 specimens were designed to study the seismic behavior of the inner layer. Fifteen specimens were evaluated based on the parameters mentioned above. Furthermore, the ID of the specimen was determined using the rule "Span length – Panel thickness (t_B) × layer number of the panel (n)" (e.g., S12.5*1 represents an S span, L = 2730 mm, specimen with only one layer of thickness t_B = 12.5 mm). Parameters (2) and (3) are marked at the end of the ID as (*dp100*) and (*V*), more detail, (*dp100*) is screw spacing in Fig. 2-1(a), (*V*) is vertical configuration of inner layer. The specimens with a base frame using stud spacing 303 are marked '@303' at the end of their ID.

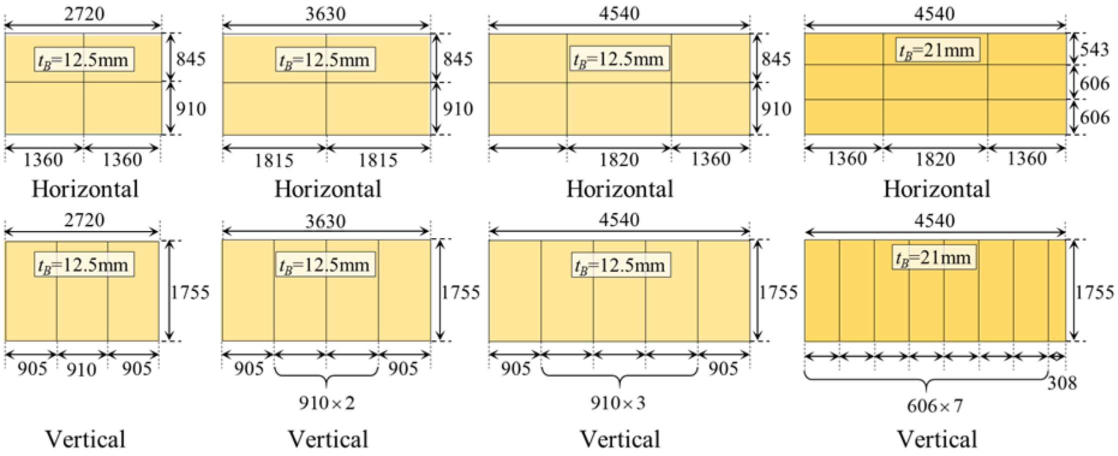

Fig. 2-6. Configuration of gypsum board: (a) S span, (b) M span, (c) L span t_B=12.5, (d) L span t_B=21 (Unit:mm).

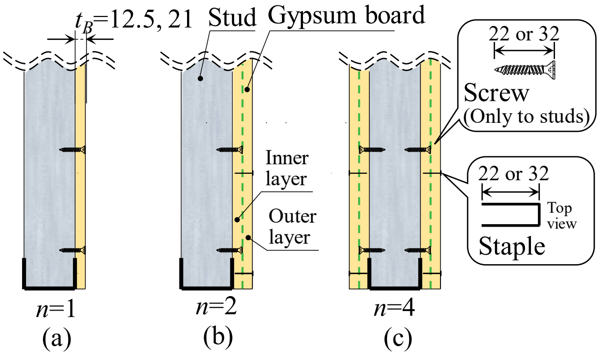

Fig. 2-7. Gypsum board layer number: (a) one side single layer n=1, (b) one side double layer n=2, (c) two side double layer n=4.

Table 2-1. List of specimens.

ID	Span	L	H	c	d_p	d_{stud}	Inner layer	Outer layer	t_B	n
S12.5*1	S	2730	1755	5	290	455	Horizontal	-	12.5	1
S12.5*2	S	2730	1755	5	290	455	Horizontal	Vertical	12.5	2
S12.5*4	S	2730	1755	5	290	455	Horizontal	Vertical	12.5	4
M12.5*1	M	3640	1755	5	290	455	Horizontal	-	12.5	1
M12.5*2	M	3640	1755	5	290	455	Horizontal	Vertical	12.5	2
M12.5*4	M	3640	1755	5	290	455	Horizontal	Vertical	12.5	4
L12.5*1	L	4550	1755	5	290	455	Horizontal	-	12.5	1
L12.5*1(dp100)	L	4550	1755	5	100	455	Horizontal	-	12.5	1
L12.5*1(V)	L	4550	1755	5	290	455	Vertical	-	12.5	1
L12.5*2	L	4550	1755	5	290	455	Horizontal	Vertical	12.5	2
L12.5*2@303	L	4550	1755	5	290	303	Horizontal	Vertical	12.5	2
L12.5*4	L	4550	1755	5	290	455	Horizontal	Vertical	12.5	4
L12.5*4@303	L	4550	1755	5	290	303	Horizontal	Vertical	12.5	4
L21*1	L	4550	1755	5	290	455	Horizontal	-	21	1
L21*2	L	4550	1755	5	290	455	Horizontal	Vertical	21	2

2.2.2 Test Setup

The test setup is illustrated in Fig. 2-8 using specimen L21*1 as an example. Setup in different span length is represented in Fig. 2-9. The loading frame is composed of steel columns and beams. All four beam-column joints are connected using pin jigs to protect the loading frame from horizontal forces. The length of the loading frame can be adjusted by replacing the beams to match the length of the specimen. The loading frame is installed with a reaction frame to make it a self-balanced reaction system; the lower beam of the loading frame is fixed to the foundation beam of the reaction frame; and the upper beam is connected to the reaction frame through a hydraulic jack. In addition, the columns and beams of the loading frame and floor surface, respectively, are designed with a minimum gap to ensure that they do not come into contact when experiencing large deformations.

The specimen is assembled in the loading frame, and the distance between the loading frame and the gypsum board is measured at the point shown in Fig. 2-9 in order to manage the clearance in the experiment. The measured clearance values are recorded in Appendix I.

Figure. 2-10 shows the details of the connection between the loading frame and metal track. The upper track is fixed to the loading frame by a steel block that is inserted between a pair of C-channel steels. The steel block is connected to the upper track by M12 bolts. [Fig. 2-10(a)]. The lower track is

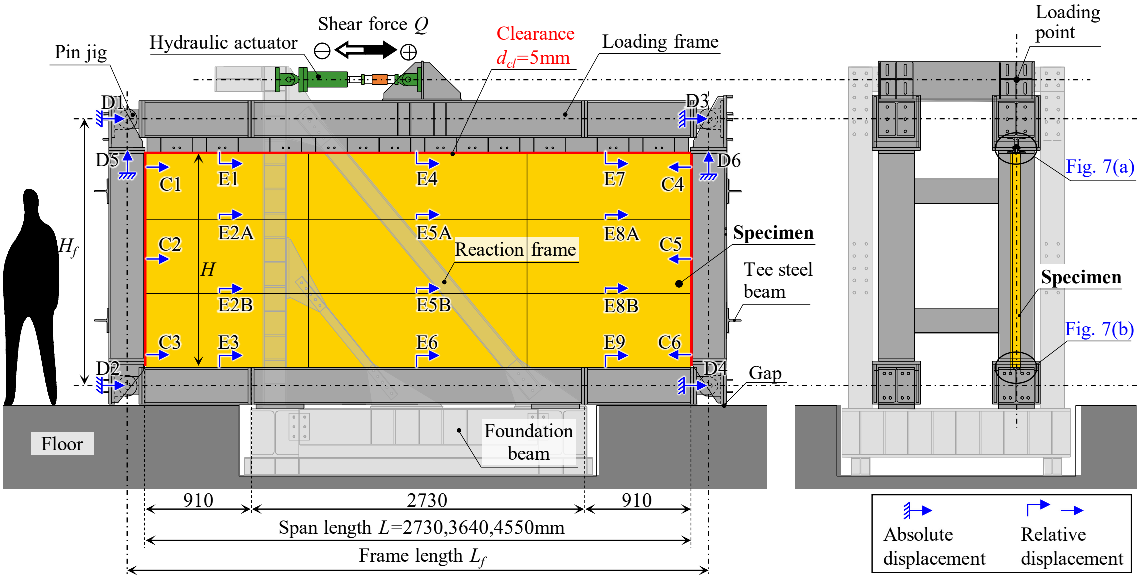

Fig. 2-8. Test setup (unit: mm).

L span

M span

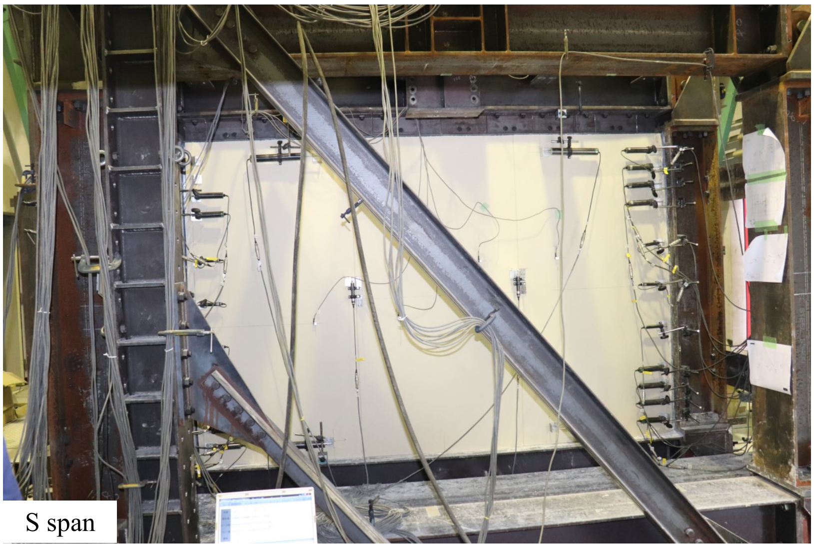

S span

Fig. 2-9. Setup of different span.

directly fixed to the lower steel beam of the loading frame using M10 bolts [Fig. 2-10(b)].

The locations of the displacement transducers are also shown in Fig. 2-8. The four displacement transducers (D1–D4) were mounted near the pin jig to measure the lateral drift (Δ_L) of the frame, which was calculated using Eq. (2-1). The vertical drift (Δ_V) of the loading frame was obtained using Eq. (2-2),

$$\Delta L = \frac{(\Delta_{\mathrm{D1}} - \Delta_{\mathrm{D2}}) + (\Delta_{\mathrm{D3}} - \Delta_{\mathrm{D4}})}{2} \qquad (2\text{-}1)$$

$$\Delta V = \Delta_{\mathrm{D5}} - \Delta_{\mathrm{D6}} \qquad (2\text{-}2)$$

where Δ_{D1}-Δ_{D4} are the lateral displacements recorded by displacement transducers D1-D4, Δ_{D5} and Δ_{D6} are the vertical displacements recorded by displacement transducers D5 and D6, as shown in Fig. 2-8.

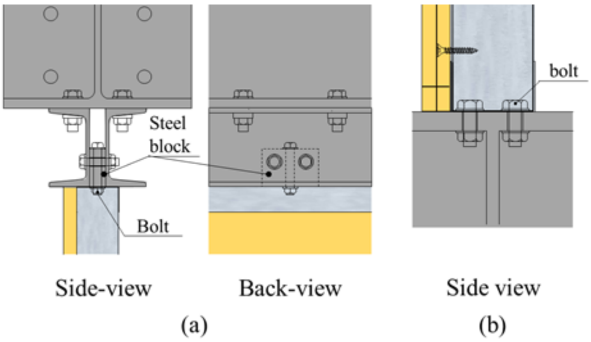

Fig. 2-10. Details about the joint between metal track and loading frame: (a) upper metal track (b) lower metal track.

measured by transducers D5 and D6. Transducers C1–C6 were installed horizontally to measure the displacement between the gypsum panel and loading frame. Transducers E1–E9 were installed horizontally to measure the sliding of the gypsum panel.

Cyclic loading from 0.001 rad to 0.045 rad was performed with increasing amplitudes of story drift ratios (R) (Fig. 2-11), and R was calculated using Eq. (2-3). For each amplitude, two cycles of loading were performed from 0.001 rad to 0.02 rad, and then one loading cycle was applied in the rest of the cycles until the end of the test. The maximum R was 0.04 rad in the negative loading direction because of the limitation of the stroke of the jack.

$$R = \frac{\Delta L}{H_f} - \frac{\Delta V}{L_f} \qquad (2\text{-}3)$$

where H_f is the vertical distance from the lower pin to the upper pin, L_f is the horizontal distance from left pin to right pin in Fig. 2-8.

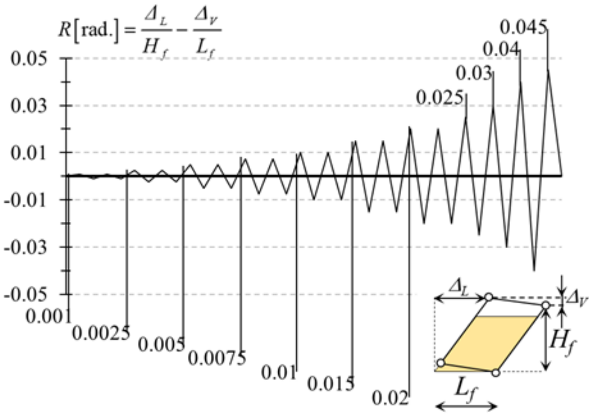

Fig. 2-11. Loading protocol.

2.3 Test Results

2.3.1 Hysteresis behavior

Fig. 2-12 shows the hysteretic curves of the lateral force (*Q*) and story drift ratio (*R*) for the specimens, as well as their envelope curves, where the lateral force (*Q*) in the vertical axis is measured by the load cell in Fig. 2-8 and horizontal axis is the story drift ratio (*R*). The envelope curves are marked in thick black line. The *P-Δ* effect on the lateral force is compensated by pre-loading the bare loading frame. The common findings of all specimens are first introduced. In the initial stages, the lateral force of the specimens remained constant (approximately 2 kN). The entire gypsum panel slid into the metal tracks through studs, which was deemed to be attributed to the clearance on the horizontal ends. A significant stiffness improvement was observed on the envelope curves after story drift ratios of approximately 0.6%. Meanwhile, the corner of the gypsum panel was squeezed by the loading frame, and local compression wrinkles can be observed in the corner. The promotion of lateral force *Q* continued until a story drift ratio of approximately 1.5% was reached, beyond which the panel continued

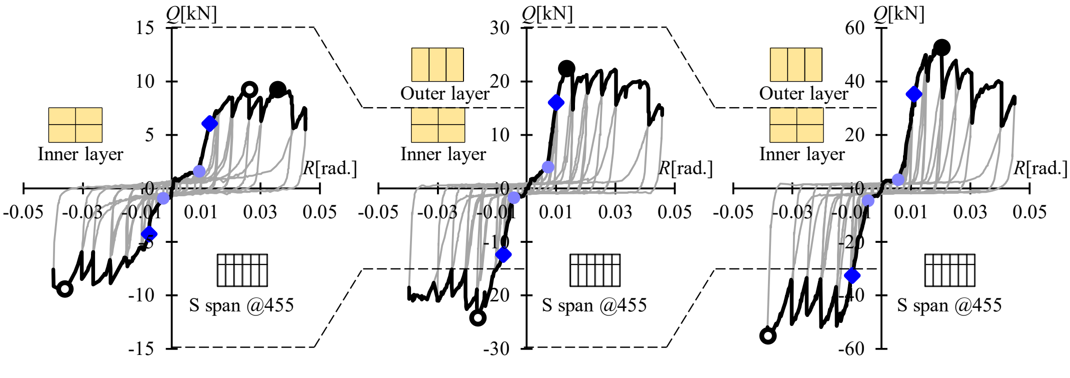

S12.5*1 S12.5*2 S12.5*4

Figure continue on the next page

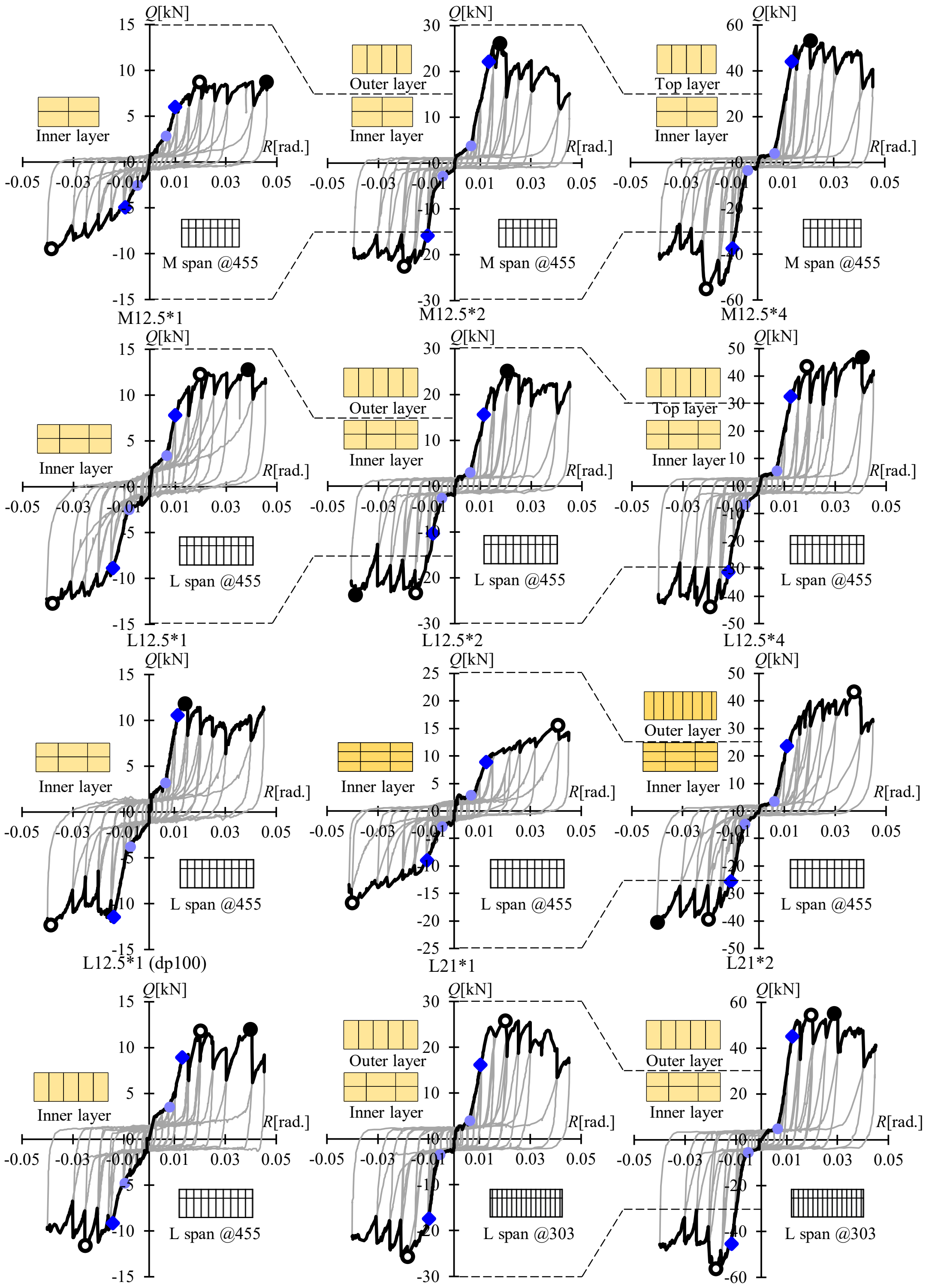

M12.5*1 M12.5*2 M12.5*4

L12.5*1 L12.5*2 L12.5*4

L12.5*1 (dp100) L21*1 L21*2

L12.5*1(V) L12.5*2@303 L12.5*4@303

Fig. 2-12. Hysteretic and envelope curves of specimens.

to sustain its lateral strength without losing stability until the end of the test.

Fig. 2-14 illustrates the definition of the envelope curve of the LGS wall. The characteristic points of the envelope curve, namely the yield strength (Q_y) and ultimate strength (Q_u), were defined to generate the performance level of the LGS wall. For the first part of the envelope curve, the clearance area is defined as the area along which the LGS wall slides due to the clearance at both ends of the gypsum panel in the initial loading cycles (i.e., origin point to point A in the figure). When the gypsum panel initially contacts the column of the loading frame, the stiffness characterized as contact stiffness (k_1), significantly increases. The intersection of clearance stiffness k_0 and contact stiffness k_1 is defined as the contact point (i.e., point A). The yield strength (Q_y) was determined when the gypsum panel was in complete contact with the loading frame (i.e., point B). Q_y is defined as the point at which the stiffness was 80% of k_1. From this point onwards, the specimen entered the plastic stage. After the stiffness deteriorated post the yield strength (Q_y), 90% of the maximum strength (Q_{max}) was reached, defined as ultimate strength (Q_u) (i.e., point C). The line between Q_y and Q_u was defined as the secondary contact stiffness (k_2). Some specimens exhibited a slow increase or maintained constant strength after Q_u, and the maximum strength (Q_{max}) was reached (i.e., point D). For the other specimens, the force decreased after Q_u; point D was not defined for these specimens (i.e., the gray solid line in the figure). The characteristic points are updated in Fig. 2-12.

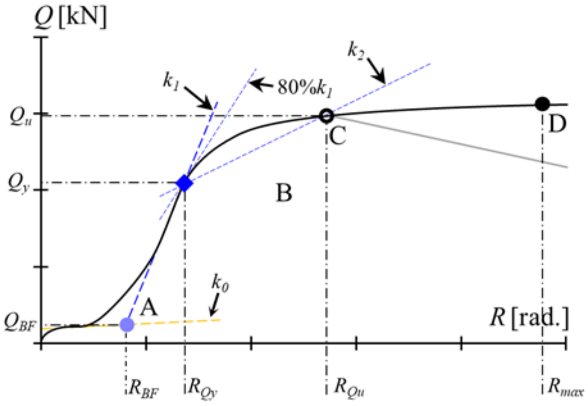

Fig. 2-13. Definition of envelope curve.

2.3.2 Damage Observation

The observed damage during the test varied with the number of layers (n) of the gypsum panel. The typical observed damage during the tests of specimens $n = 1$ and specimens $n = 2$ and 4 with the corresponding story drift ratios (R) is shown in Figs. 2-14 and 2-15, respectively.

On specimens $n = 1$, no significant damage was observed until the story drift ratio (R) reached 0.75%, and only a slight bearing deformation was observed at the ends of the metal track [Fig. 2-14(a)]. The corner of the gypsum panel then contacted the loading frame, which caused local compression wrinkles [Fig. 2-14(b)]. As the story drift ratio increased, the wrinkles became local compressive damage [Figs. 2-14(c), (d)], and the gypsum dust dropped. Rigid body rotation of the gypsum panel was not observed during the experiment; only relative slip between the upper and lower layers of the gypsum panel was observed [Fig. 2-14(e)]. When the story drift ratio (R) was increased to 4%, the edge of the gypsum panel contacted the loading frame, causing compressive damage due to the sliding of the upper and lower gypsum panels [Figs. 2-14(f) and (g)], as well as more severe compressive damage at each corner [Fig. 2-14(h)]. It is noteworthy that the out-of-plane deformation of the entire gypsum panel was observed at story drift ratios of approximately 4%[Fig. 2-14(i)].

On the $n = 2$ and $n = 4$ specimens, in the initial loading cycles, the observed damage was similar to that of $n = 1$ specimens, that is, bearing deformation on the metal track [Fig. 2-15(a)], and local compression wrinkles [Fig. 2-15(b)] were observed. As the story drift ratio increased, local compression on the gypsum panel was observed [Fig. 2-15(c)], and the wrinkle became local compressive damage [Fig. 2-15(d)]. It was observed that during the test, no rigid body rotation occurred, apart from specimen L-21*2, where it was found that the gypsum boards of the outer layer rotated independently. Out-of-plane deformation was only observed partially at the ends of the gypsum panel [Fig. 2-15(e)], accompanied by corner crushing of the gypsum panel [Fig. 2-15(f)].

For both $n = 1$ and $n = 2$ or 4 specimens, the degree of damage is considered to be related to the envelope curves. No significant damage was observed on the specimens at the initial stage when the gypsum panel was not in contact with the loading frame. During subsequent increase in stiffness, only minor damage, such as compressive wrinkles on the gypsum panel, was observed. As the stiffness began to decrease, significant damage was gradually observed.

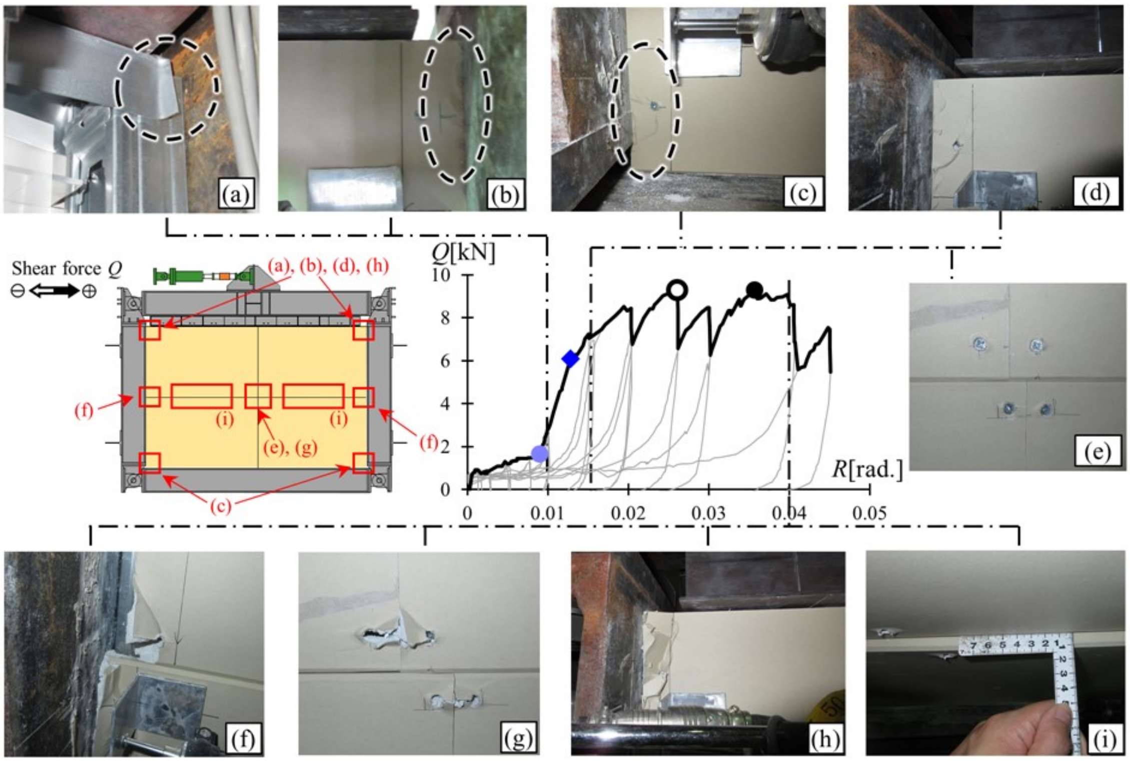

Fig. 2-14. Observed damage on n = 1 specimens.

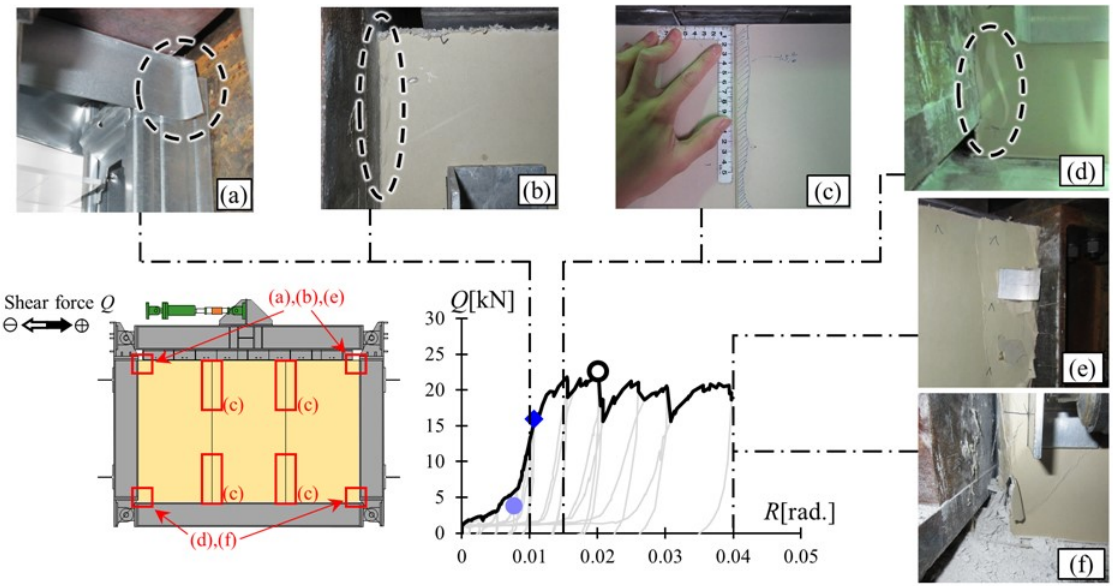

Fig. 2-15. Observed damage on n=2 or 4 specimens.

An observation on the same location of the same specimen further verified that the degree of damage of the specimen was related to the envelope curve. For specimens with outer layers (i.e., *n* = 2 and *n* = 4), where the main failure mode was deemed to be the compressive damage of the gypsum panel, similar damage was observed on each specimen at similar loading displacements, and the damage associated with each displacement was recorded. Figure 2-15 illustrates a typical example of damage to the left upper corner of the gypsum panel of specimen S12.5*2 during the first loading cycle of each amplitude of story drift ratio *R* from +0.005 to +0.03 rad. Figure 2-15 shows that as the *R* increases, there is a clearance between the gypsum panel and loading frame from the beginning (+0.005 rad). Subsequently, the clearance disappears (+0.0075 rad, point A in Fig. 2-13), followed by a slight compression wrinkle (+0.01 rad, point B in Fig. 2-13), and then the wall is crushed by compression (after +0.015 rad, point C in Fig. 2-13).

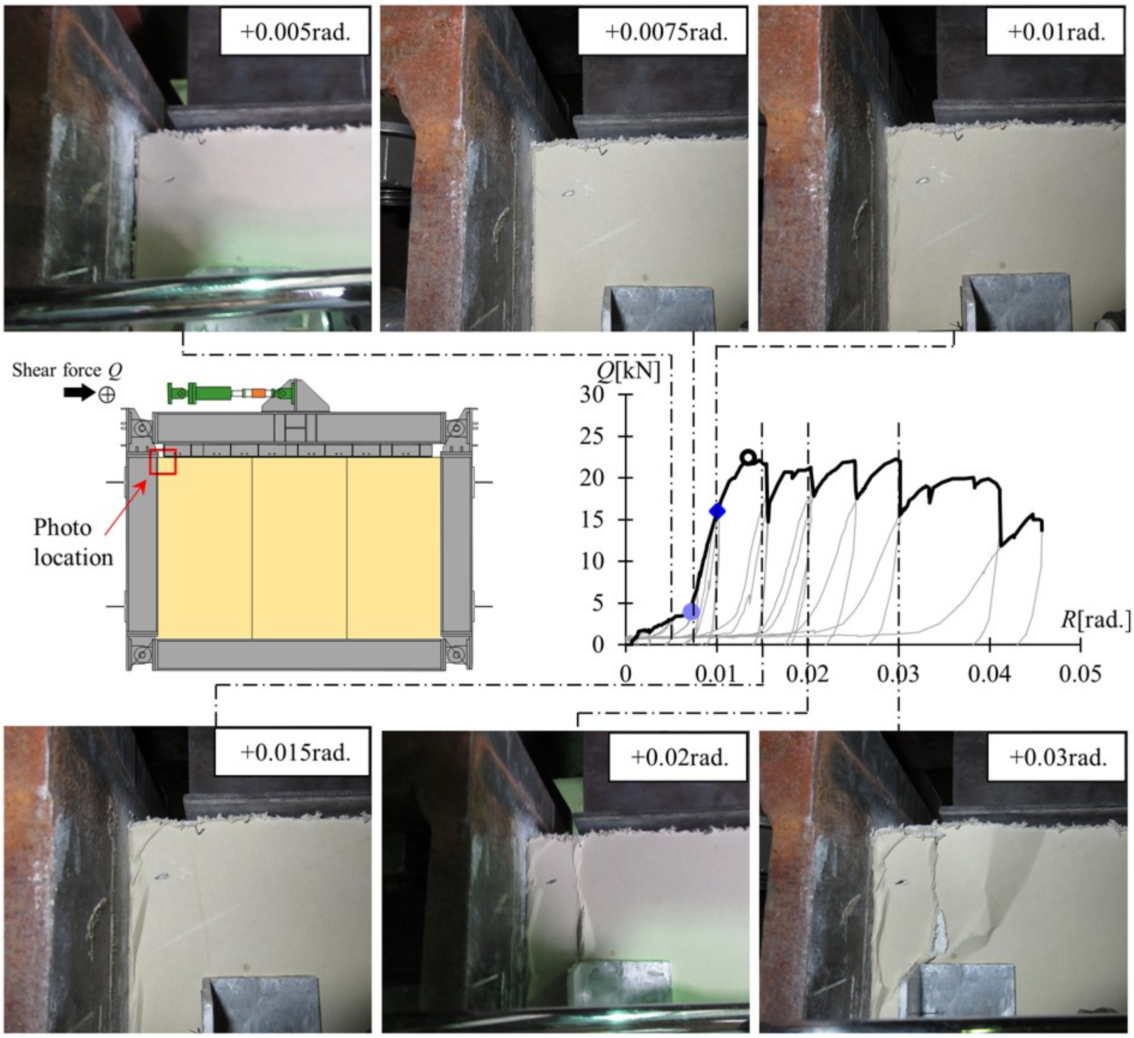

Fig. 2-16. Damage development of the gypsum panel at the loading cycle from 0.005 rad to 0.03 rad (with specimen S12.5*2 as an example).

The deformations measured by the transducers are reported next. The lateral displacement at the top-end of the gypsum panel (Δ) can be calculated using Eq. (2-4) [Fig. 2-17(a)]; and is comprised of three characteristics of the gypsum panel: separation between the gypsum panel and loading frame (Δ_{se}) [Fig. 2-17(b)]; lateral slip of gypsum panel (Δ_{slip}), calculated using Eq. (2-5) [Fig. 2-17(c)], and the rocking displacement Δ_{ro}[Fig. 2-17(d)]. In addition, the lateral displacement of each horizontal joint is calculated by Eq. (2-5).

$$\Delta = R \times H = \Delta_{se} + \Delta_{slip} + \Delta_{ro} \tag{2-4}$$

$$\Delta_{slip} = \Delta_{slip-1} + \Delta_{slip-2} + \Delta_{slip-3} \tag{2-5}$$

where Δ_{se} is obtained by the transducers C1-C6 in Fig. 2-8, Δ_{ro} is obtained by transducer E1, E3, E4, E6, E7 and E9 in Fig.2-18, $\Delta_{slip-i(i=1,2,3)}$ is calculated by the data of transducers E2-E3, E5-E6, E8-E9.

The separation Δ_{se} can be calculated by Eq.(2-6) ,

$$\Delta_{SE} = \Delta_{C1} \text{ or } \Delta_{C4} \tag{2-6}$$

where the subscript of Δ corresponds to its displacement transducer, i.e.: the corresponding D Δ_{C1} and Δ_{C4} is the data of transducer C1 and C4, respectively.

The slip Δ_{slip-1}, Δ_{slip-2}, Δ_{slip-3} can be calculated by Eq.(2-7) ,

$$\Delta_{slip-1} = \frac{\Delta_{E3} + \Delta_{E6} + \Delta_{E9}}{3} \tag{2-7a}$$

$$\Delta_{slip-2} = \frac{\Delta_{E2B} + \Delta_{E5B} + \Delta_{E8B}}{3} \tag{2-7b}$$

$$\Delta_{slip-3} = \frac{\Delta_{E2A} + \Delta_{E5A} + \Delta_{E8A}}{3} \tag{2-7c}$$

where the subscript of Δ corresponds to its displacement transducer.

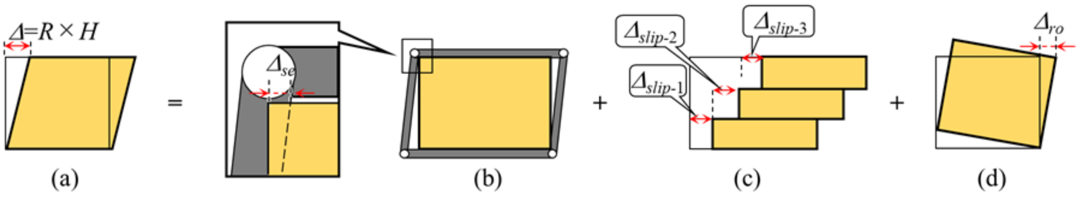

Fig.2-17. Gypsum shear behavior: (a) total, (b) separation, (c) slip, (d) rigid body rotation.

For vertical configuration, the rigid body rotation angle $\mathit{\Delta}_{ro}$ can be calculated by Eq. (2-8), the calculation of $\mathit{\Delta}_{ro\text{-}34}$, $\mathit{\Delta}_{ro\text{-}56}$ is similar to $\mathit{\Delta}_{ro\text{-}12}$.

$$\mathit{\Delta}_{ro-12} = (R \times H_f - \mathit{\Delta}_{EN1}) - \mathit{\Delta}_{EN2} \qquad (2\text{-}8a)$$

$$\mathit{\Delta}_{ro} = \frac{\mathit{\Delta}_{ro\text{-}12} + \mathit{\Delta}_{ro\text{-}34} + \mathit{\Delta}_{ro\text{-}56}}{3} \qquad (2\text{-}8b)$$

where the subscript of $\mathit{\Delta}$ corresponds to its displacement transducer.

For vertical configuration, the rigid body rotation angle $\mathit{\Delta}_{ro}$ can be calculated by Eq. (2-8), the calculation of $\mathit{\Delta}_{ro\text{-}34}$, $\mathit{\Delta}_{ro\text{-}56}$ is similar to $\mathit{\Delta}_{ro\text{-}12}$. When there are two configurations (i.e.: horizontal and vertical configuration) at the same time, the $\mathit{\Delta}_{ro}$ of vertical one will be calculated.

$$\mathit{\Delta}_{ro-123} = (R \times H_f - \mathit{\Delta}_{E1}) - (\mathit{\Delta}_{E3} + \mathit{\Delta}_{E2A} + \mathit{\Delta}_{E2B}) \qquad (2\text{-}9a)$$

$$\mathit{\Delta}_{ro} = \frac{\mathit{\Delta}_{ro\text{-}123} + \mathit{\Delta}_{ro\text{-}456} + \mathit{\Delta}_{ro\text{-}789}}{3} \qquad (2\text{-}9b)$$

where the subscript of $\mathit{\Delta}$ corresponds to its displacement transducer.

Fig.2-19 represents the deformation of each factor in Eq. (2-4) of the gypsum panels in the first cycle at different amplitudes of story drift ratios from 0.25% to 1.5%. The vertical axis is the story drift ratio R, the horizontal axis is the data of corresponding transducers. Their percentages are indicated next to the corresponding bars. All the specimens in this test are predominated by a slip of the gypsum panel; however, the slip (i.e., $\Delta_{slip\text{-}1}$, $\Delta_{slip\text{-}2}$, and $\Delta_{slip\text{-}3}$ of Fig.2-16(c)) differs according to the configuration. The separation (Δ_{se}) is considered to be related to the compressive damage on both ends of the gypsum panel. The gypsum panel is squeezed by the loading frame if Δ_{se} exceeds 5 mm; Δ_{se} is the clearance on both

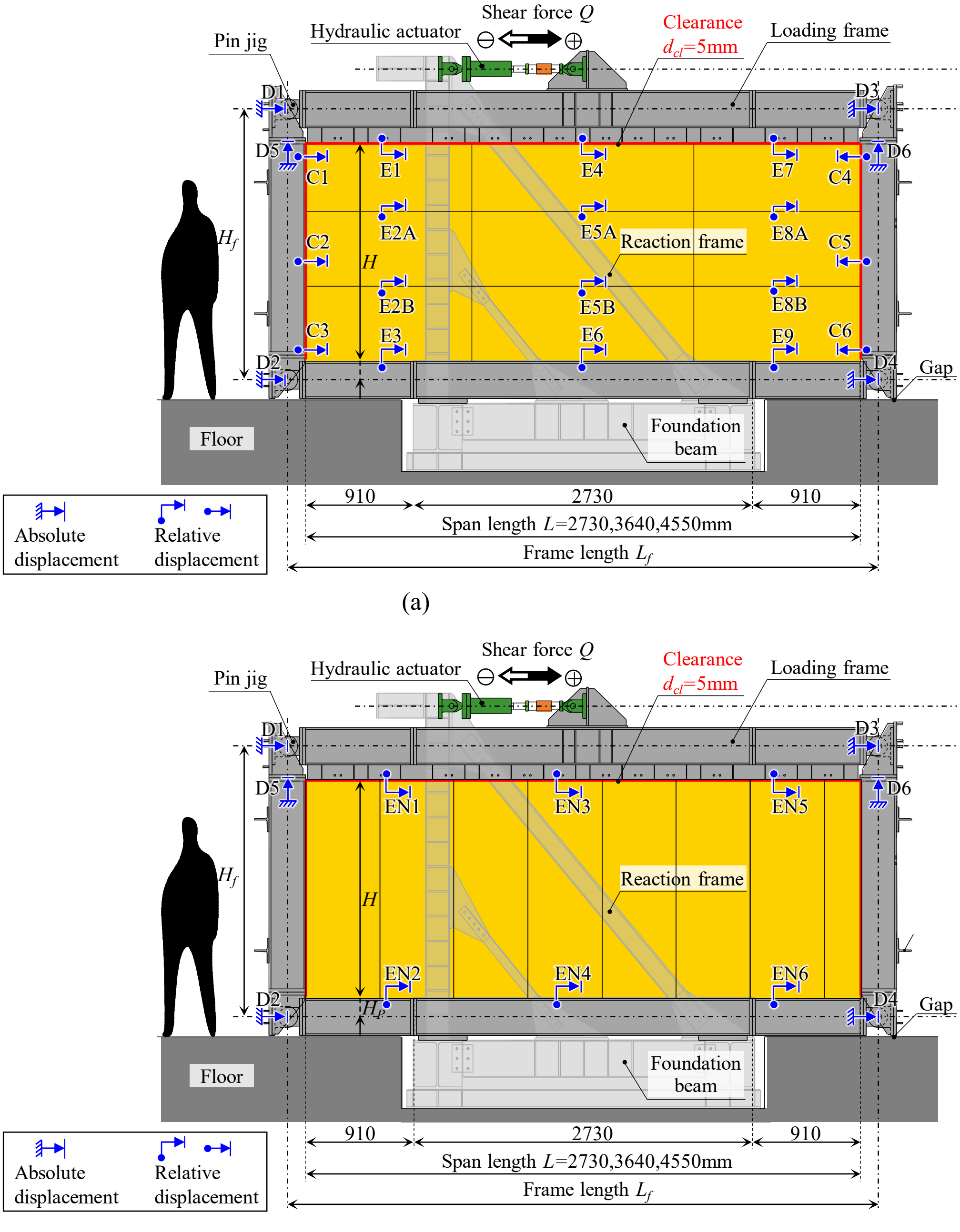

(a)

(b)

Fig.2-18. Measurement setup: (a) horizontal configuration, (b) vertical configuration.

ends of the gypsum panel, marked in Fig.2-19.

The analysis of each parameter is described as follows.

(1) As the degree of damage is almost identical among the specimens of spans S, M, and L, only the results of span L are discussed.

(2) If the consumption of the screw of the inner layer is increased, it can be deduced from [Fig.2-19(a) and (b)] that the slip (Δ_{slip}) of the gypsum panel would decrease. However, this would result in greater compressive damage (Δ_{se}) at the ends of the gypsum panel. By comparing the hysteresis curves of the two specimens (Fig. 2-12), specimen L12.5*1 (dp100) reached the maximum force at a small story drift ratio and exhibited a significant decline in the force thereafter. Based on these results, it is apparent that as non-structural components, increasing the consumption of the screws does not result in an enhanced ductility; thus, this design is undesirable.

(3) For a horizontal or vertical design configuration of the panel, by comparing the test results illustrated in [Fig.2-19(a) and (c)], the compressive damage (Δ_{se}) of the vertically placed gypsum panel was higher, which can be explained by the fact that the vertical gypsum panel had no horizontal joints, and the deformation could only be balanced by compressing the two ends of the panel. Therefore, it can be concluded that the compressive damage of the gypsum panel decreases with an increase in the number of horizontal joints.

(4) The same phenomenon can be revealed by comparing specimens L12.5*1 and L21*1, which differ in board thickness. As the thicker board was smaller in dimensions, more gypsum boards were used for the same wall height in the construction process; thus, the number of horizontal joints was increased.

(5) For the layer number, the separation (Δ_{se}) of specimens n = 2 and n = 4 [Fig.2-19(e)-(g)] was higher than that of specimen n = 1 [Fig.2-19(a)-(d)], except for specimen L21*2 [Fig.2-19 (h)]; the reason is considered to be that the outer and inner layers of specimens n = 2 and n = 4 remained unified during the test. Consequently, the behavior of the specimens is similar to that of vertically placed specimens, and they sustain more compressive damage. Additionally, the outer layer of specimen L21*2 was separated from the inner layer during the loading, and its outer layer presented a significant rigid body rotation, while its inner layer showed a slight relative horizontal slip between the upper and lower gypsum panels.

(6) Reduced spacing between the studs results in an increase in the stud number, and an increase in the number of studs is considered to reduce the relative slip between the upper and lower gypsum panels. However, the outer and inner layers remained unified, and the increase in the number of studs did not have an obvious effect on preventing the relative slip[Fig.2-19(e)-(f)].

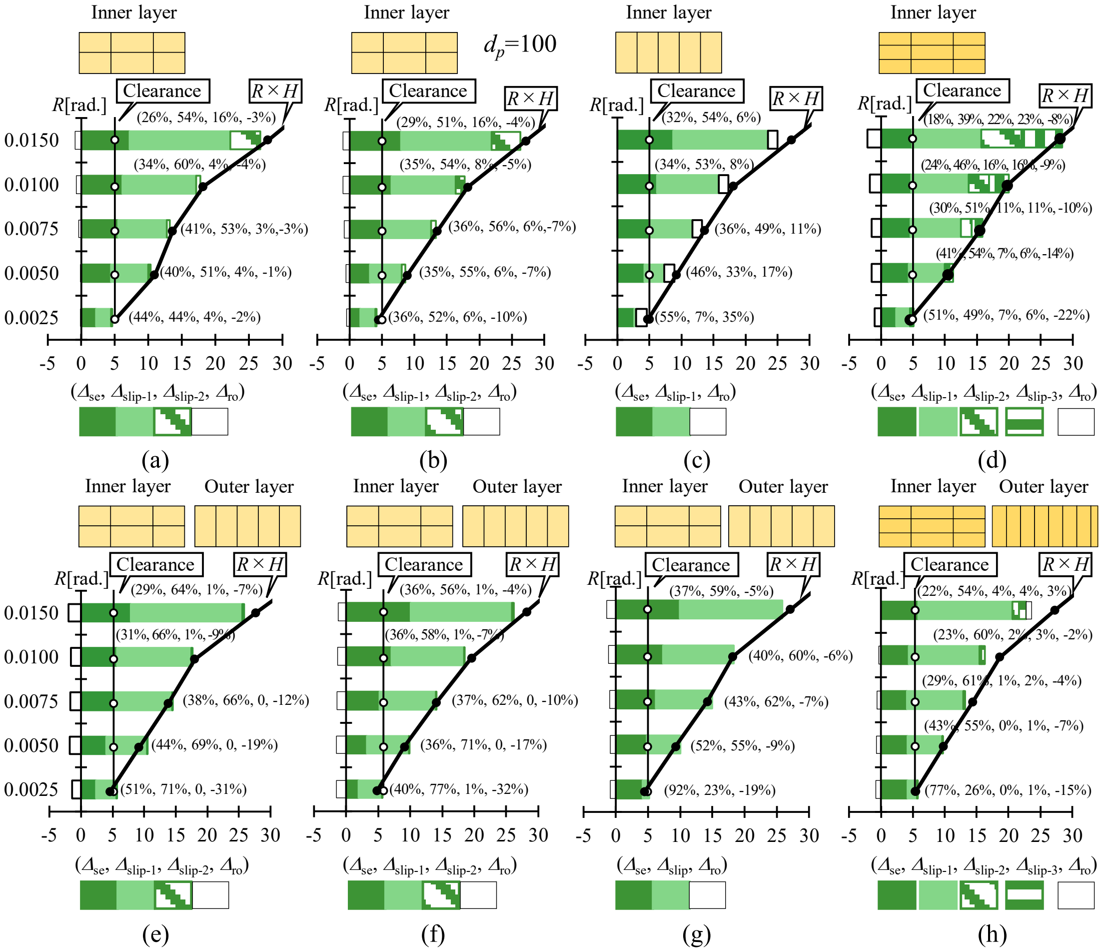

Fig.2-19. Decomposition of deformation: (a) specimen L12.5*1, (b) specimen L12.5*1(dp100), (c) specimen L12.5*1(V), (d) specimen L21*1, (e) specimen L12.5*2@303, (f) specimen L12.5*2@455, (g) specimen L12.5*4, (h) specimen L21*2.

Two failure modes of the LGS wall were observed during the test: (a) the relative slip between the upper and lower gypsum panels, which was observed for the n = 1 specimens with a horizontal configuration, and (b) the local compression of the gypsum panel, which was observed for the n = 2 and n = 4 specimens. Although the clearance can delay compressive damage on the ends of the panel, n = 1 specimens with a horizontal configuration will exhibit out-of-plane deformation of the entire panel at larger story drift ratios. In consideration of human safety, the $n = 1$ LGS wall with a horizontal configuration is not recommended for design or use.

2.3.3 Performance levels for LGS partition

Considering that the degree of damage is related to the envelope curve, a qualitative definition of the damage states of the LGS wall is provided in this study. According to the change in stiffness, some characteristic points were marked on the envelope curve. Subsequently, this study provides a detailed description of each characteristic point on the envelope curve and presents characteristic-point-specific equations, followed by a comparison with the experimental results. In addition, to verify the usability of these equations, experimental results from previous studies are evaluated for comparison, a few experimental results from previous studies introduced in Chapter 1 are evaluated for comparison: Scholars have investigated LGS partition built in accordance with Japanese practice through large-scale experiments, Tamura et al. [2-7], Kumazawa et al. [2-8] and Mitani et al. [2-9] conducted a series of experimental about LGS partition with opening, Suzuki et al. [2-10] conducted large experiments with many construction details (e.g.: consumption of the staple) as parameter. The details of the previous studies are listed in Table 2-2. Among these previous studies is another experimental project conducted by the same research laboratory as this study [2-3]; the specimens and loading frames used are almost identical, with the exception of the size of the specimens. Two additional details are worth noting: (1)

Table 2-2. Envelope curve detail (Unit: mm).

Specimen	panel height *H*	panel length *L*	panel thickness *t*	clearance c	Standard size of single gypsum board
Specimen No.1 (Isoda et al. [2-3])	3000	5010	12.5×4	5×2	1820×910
Specimen No.1 (Lee et al. [2-4])	2800	3950	12.5×4	15×2	1820×910
MIF1-STFD (Tasligedik et al. [2-5])	2550	2900	13×2	(15+5)×4	2550×950*
Specimen #7 & #8 (Pali et al. [2-6])	2700	2400	12.5×4	20×2	2700×1200*

*: Assumed according to the corresponding configuration figure.

the specimen in [2-3] was filled with insulation and adhesive sealant in the clearance of the panel, and (2) it was loaded until 2% of the story drift ratio. Additionally, although Tamura et al. [2-7] and Suzuki et al. [2-10] conducted experiments of LGS subjected to in-plane cyclic loading, they didn’t set clearance at the specimen. Kumazawa et al. [2-8] and Mitani et al. [2-9] conducted a series of experiments of LGS partition with opening. Their experiment is out of scope of this study.

Analysis of the characteristic points of envelope curve

A definition of the specific performance levels suitable for an in-plane response of a LGS wall with local compression failure (i.e., $n = 2$ and $n = 4$ specimens and specimen L12.5*1(V)) is proposed in this study. The limiting state definition relies on the performance of the LGS wall obtained from the results of this experimental study. A description of each characteristic point and the corresponding stiffness is provided below.

Contact Point A

The strength of contact point A (Q_{BF}) is considered to involve two parts, self-weight of the gypsum panel and friction of the track-stud connection. The self-weight factor is associated with the volume of the gypsum panel, as the density of the gypsum boards are the same in this experiment. Owing to the change in contact area, the friction is considered to be related to the number of studs. Therefore, an empirical equation, i.e., Eq. (2-10) is derived through a linear regression analysis. The Q_{BF} obtained from the experiment was compared to that obtained from the calculation [Fig. 2-20(a)]. The calculation results were almost the same as the experimental results; thus, the former is used in the following discussion.

$$Q_{BF} = 8.04 \times V + 0.15 \times n_s \qquad (2\text{-}10)$$

where V is the volume of gypsum boards (Unit: m^3), n_s is the number of the studs.

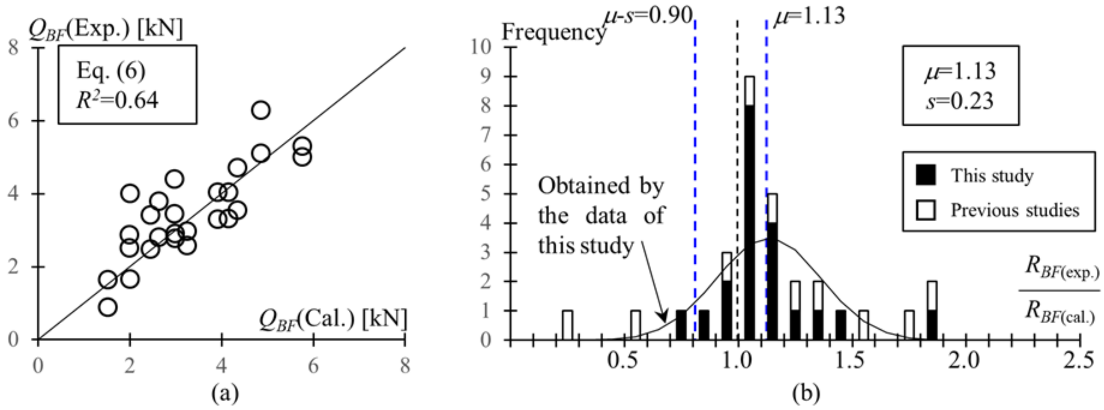

(a) (b)

Fig. 2-20. Experimental results versus calculation results of point A: (a) strength, (b) drift ratio.

In addition, the deformation of point A (R_{BF}) can be obtained using Eq. (2-7) (Fig. 2-22). It is worth noting that the height of the compression side of the gypsum panel (h_0) is assumed to be 45% of the height of the specimen. A comparison ratio is derived by dividing the calculation results by the corresponding experimental results, and its frequency distribution is shown in [Fig. 2-20(b)], where μ is the mean value, s is the standard deviation, and the ratio value of 1 (i.e., experimental results are equal to the calculation results) is close to μ-s; thus, the equation can be used to evaluate the safe-side story drift ratio. It is considered that the clearance of the gypsum panel and sliding joint of the base frame substantially delays the contact between the loading frame and gypsum panel. Additionally, the estimated values of R_{BF} for several specimens of previous studies are considerably smaller than those of this study, indicating that the clearance value (c) is influenced by filling materials such as an adhesive sealant.

Moreover, the relationship between the values of each clearance measured in the experiment and the hysteresis curve is described in detail in Appendix III.

Yield strength (point B)

The stress-strain relationship for gypsum board was developed based on the results of material tests conducted by Sato. et al. [2-11] who tested various directions of several types of gypsum boards commonly used in Japanese construction, and the results of these experiments are parametrically analyzed in this study. The final proposed relationship is represented in Fig. 2-21. The detailed parametrically analyses are introduced in Appendix IV. Fig. 2-21 illustrates the local compression deformation geometric relationship at R_{Qy}. The local deformation (d_y), corresponding story drift ratio (R_{Qy}), and contact height (h) can then be calculated using Eqs. (2-11)-(2-13). By assuming a triangular compressive stress distribution within the compression zone, the yield strength (Q_y) can be calculated using Eq. (2-14). The contact stiffness can be obtained using Eq. (2-15), where $k=Q/R$.

A comparison of the experimental and calculated results of the strength of point B, stiffness, and story drift ratio is shown in [Fig.2-22(a), (b) and (c)], respectively. The experimental results of the strength and stiffness of point B differed by multiples in the range of 0.5–1 to those of this study. This may be because the clearance of the gypsum panel varied between the inner and outer layers, or the clearance (c) may differ from the design value of 5 mm owing to a construction error. Fig.2-23 shows an example where the inner layer is constructed to the design value; however, the clearance of the outer layer is shorter than the design value. Because the clearance in this study remained empty, that is, it did not contain an adhesive sealant, the loading frame contacts the outer layer first. Consequently, the strength and stiffness may be lower than expected. In the subsequent figure, half layer means that one of the inner layer or outer layer is in contact with the loading frame (i.e.: the panel thickness t_B in the equation is half of the actual value). And full-layer means that both inner layer and outer layer are in contact with the loading frame. For the previous studies, assuming that the specimens had material properties similar to those of the specimens in this study and all used an adhesive sealant in the clearance, the

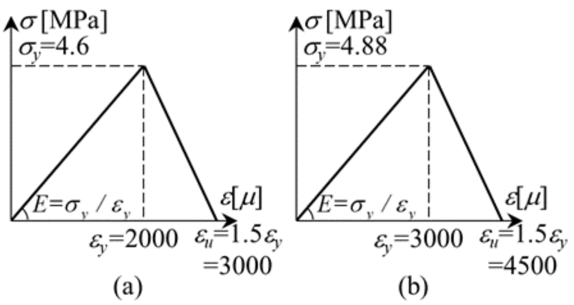

Fig. 2-21. Stress-strain relation of gypsum board: (a) t_B=12.5 mm board, (b) t_B=21 mm board.

(Modified according to Sato Y. [2-11]'s results) clearance (c) is lower than the design values, which results in their higher calculated values. The frequency distribution of the comparison of the story drift ratio in Fig.2-17(c) demonstrates that the equation can estimate a safe story drift ratio.

$$d_y = l_e \times \varepsilon_y \tag{2-11}$$

$$R_{Qy} = \frac{d_y + c}{h_0} \tag{2-12}$$

$$h = \frac{d_y}{R_{Qy}} = \frac{h_0 \times (l_e \times \sigma_y)}{l_e \times \sigma_y + c \times E} \tag{2-13}$$

$$Q_y = \frac{1}{2}\sigma_y \times t \times h = \frac{1}{2}\sigma_y \times t \times h_0 \times \frac{l_e \times \sigma_y}{l_e \times \sigma_y + c \times E} \tag{2-14}$$

$$k_1 = \frac{Q_y}{R - c / h_0} = \frac{1}{2}\sigma_y \times t \times h_0 \times \frac{E \times h_0^2}{l_e \times \sigma_y + c \times E} \tag{2-15}$$

where l_e is the effective length of the gypsum panel, assumed as an average of the combination of the length and width of a gypsum board (i.e., l_e= 1365 mm for t_B = 12.5 mm specimens, and l_e= 1213 mm for t_B= 21 mm specimens); σ_y is the average maximum compressive stress of the grain in the perpendicular and parallel direction, which has values of 4.6 MPa and 4.88 MPa for gypsum boards of t_B = 12.5 mm and t_B = 21 mm, respectively; and E is the elastic modulus of gypsum board, assumed to have values of 2300 N/mm^2 and 1627 N/mm^2 for gypsum boards having t_B = 12.5 mm and t_B = 21 mm, respectively.

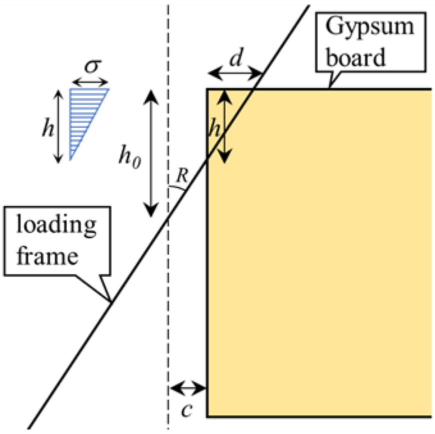

Fig. 2-22. Calculation of local compression.

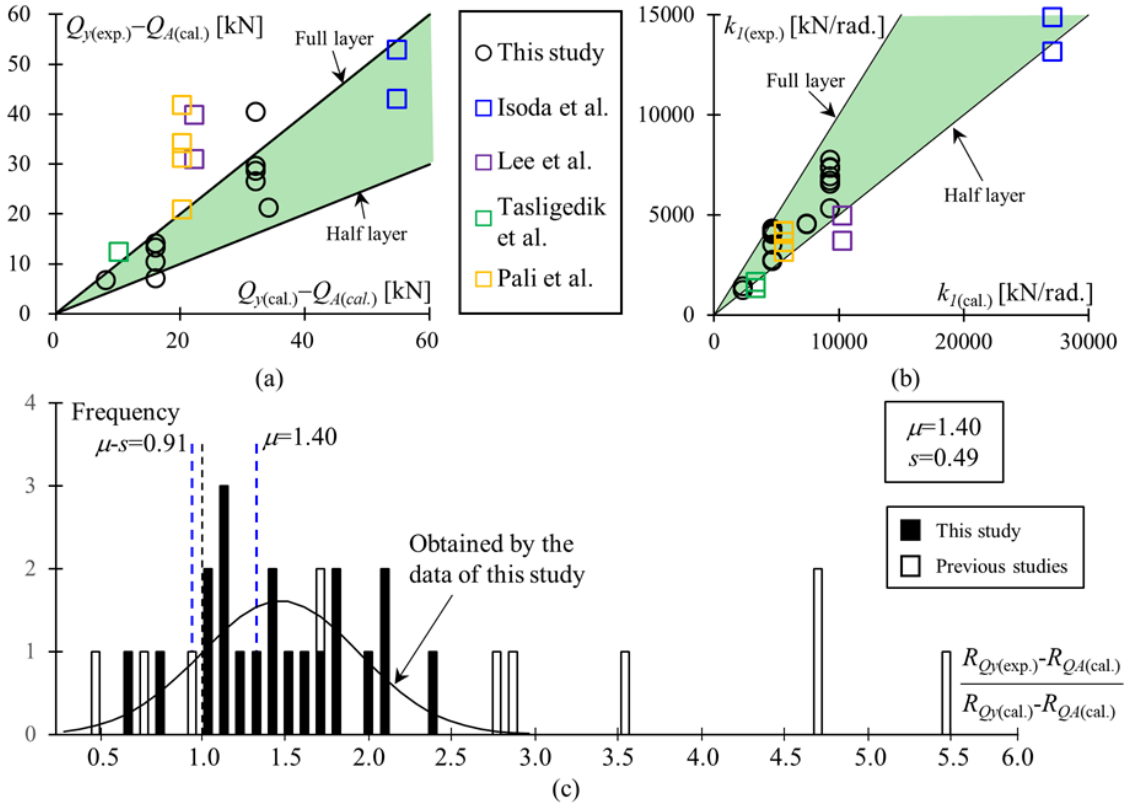

Fig. 2-23. Experimental results versus calculation results of point B: (a) strength, (b) stiffness, (c) drift ratio.

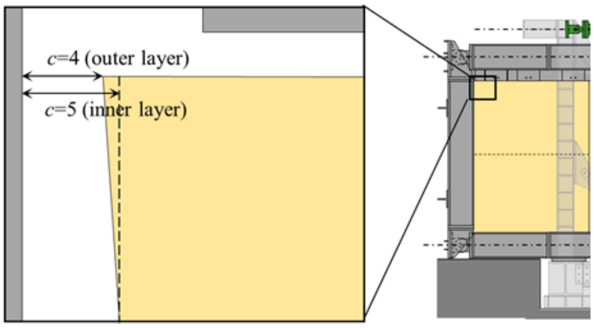

Fig. 2-24. Example of construction error of clearance (half layer).

Ultimate strength (point C)

After reaching the yield stage, the compression stress of the gypsum panel is considered to decrease according to the material test conducted by Sato et al. [2-11], and the stress deteriorates to the ultimate point when the strain reaches 1.5 times the yield strain (i.e., $\varepsilon_u = 1.5\varepsilon_y$). The ultimate strength (Q_u), which is regarded as the maximum strength of the gypsum panel, can be estimated by the ultimate point in Fig. 2-21, which is derived using Eq. (2-16). It is worth noting that when the specimens are at yield point [Fig. 2-23(a)], most of the specimens are calculated between half layer and full layer due to construction errors. When the specimens are at the maximum point [Fig. 2-25(a)], most of the specimens are close to the full layer. The secondary contact stiffness is determined by averaging the ratio of the calculated initial contact stiffness to the experimental value of the secondary stiffness Fig.2-24(b) , thus $k_2 = 0.21k_1$. Eq. (2-17) can then be used to calculate the story drift ratio using $R = Q/k$.

$$Q_u = \frac{1}{2}\sigma_y \times t \times h = \frac{1}{2}\sigma_y \times t \times h_0 \times \frac{3l_e \times \sigma_y}{3l_e \times \sigma_y + 2c \times E} \tag{2-16}$$

$$R_{Qy} = R_{Qy} + \frac{Q_u - Q_y}{k_2} \tag{2-17}$$

The results for point C are similar to those for point B. As the value of the ratio of experimental to estimated displacement at point C is notably less than μ–s, the equation provides a lower bound for the tested specimens. (Fig.2-24)

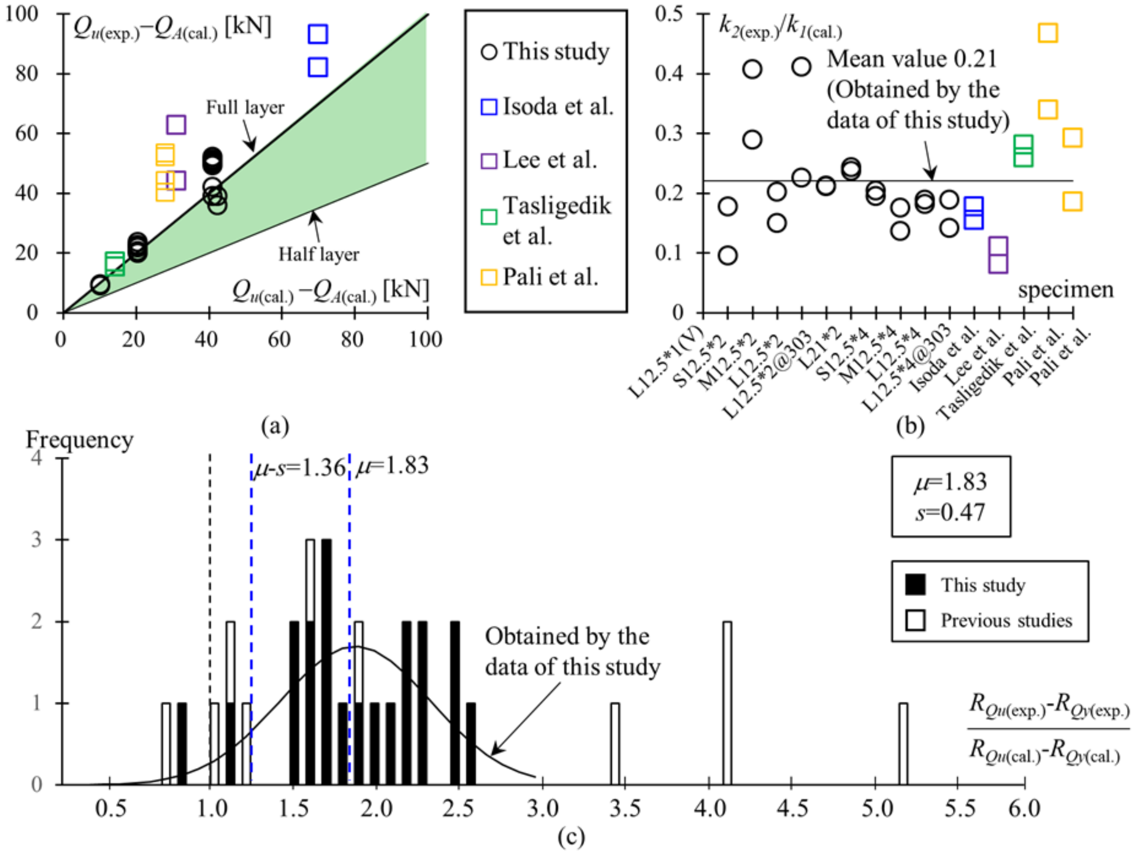

Fig. 2-25. Experimental results versus calculation results of point C: (a) strength, (b) stiffness, (c) drift ratio.

Maximum strength Q_{max}

For some specimens, the lateral force decreases after point C, while it does not decrease for the other specimens. The load remains constant or increases until the jack reaches its limit. This phenomenon is considered to be caused by experimental variations. The displacement of the specimens at point D was recorded and compared with that at point C (Fig. 2-26). According to the results, the displacement of point D / point C was in the range 1.68–3.75. The displacement at point D (R_{max}) can be presented as follows.

$$R_{BF} + 1.68(R_{Qu} - R_{BF}) \le R_{max} \le R_{BF} + 3.75(R_{Qu} - R_{BF}) \tag{2-18}$$

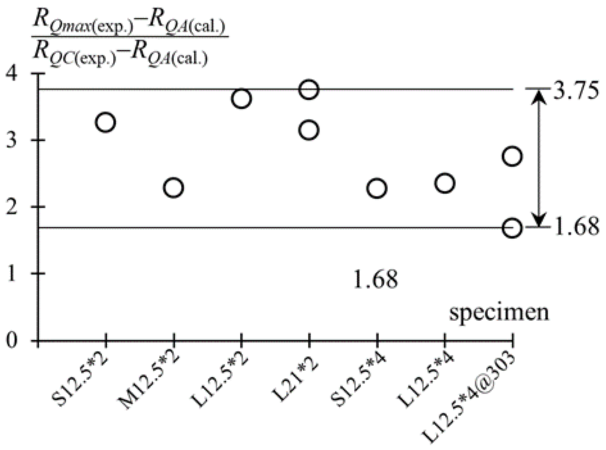

Fig. 2-26. Range of point D

2.3 Performance level of LGS partition

According to the damage observed during the test, for the LGS wall, performance levels may be described as the story drift ratio (R) associated with a given degree of damage, based on in-plane cyclic tests on LGS wall specimens. Therefore, three LGS-wall-specific limit states are introduced based on the growing level of infill damage due to the in-plane story drift ratio (Fig. 2-15 and Fig. 2-16):

(DS1) LGS wall can be used continually from origin to the story drift ratio of yield strength R_{Qy}. As the gypsum panel does not collide with the surrounding frame, only little visible damage can be found on the partition [Fig. 2-15(a)]. The gypsum panel is attached using studs, which slide in the metal track. The gypsum panel is regarded as intact, and the LGS wall can be used continuously.

(DS 2) LGS wall should be repaired partially from the story drift ratio of yield strength R_{Qy} to the story drift ratio of ultimate strength R_{Qu}. Local compressive damage to the gypsum panel and metal track of the base frame is expected as a result of the contact between the gypsum panel and surrounding frame [Fig. 2-16(b)–(d)] but can be repaired effectively and economically.

(DS 3) It is recommended that the partition wall be replaced when the story drift ratio of the frame has exceeded the story drift ratio at the ultimate strength (R_{Qu}). As the story drift ratio increases, the surrounding frame begins to squeeze the gypsum panel until it is severely damaged and reparability becomes uneconomical [Fig. 2-15(e)–(f)], even though the lateral resistance of the gypsum panel may

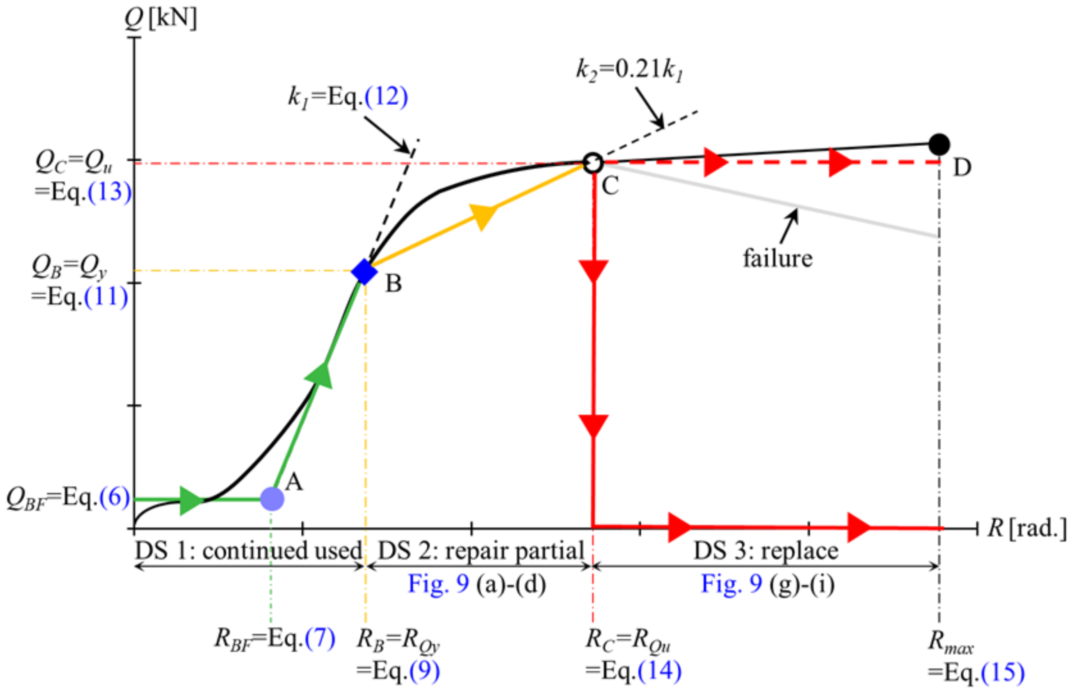

Fig.2-26. Performance levels for LGS partition wall.

remain at a fairly high level. It is worth noting that the damage corresponding to the story drift ratios at 0.015 rad, 0.02 rad, and 0.03 rad in Fig. 2-16 should be classified as DS2 according to the damage observation; however, the specimen-stiffness deterioration indicates that the gypsum panel sustained severe damage; therefore, when the story drift ratio of the frame has exceeded the story drift ratio at the ultimate strength R_{Qu}, the damage is classified as DS3. Moreover, Fig. 2-27 illustrates the LGS-wall force-displacement contribution along with the drift levels associated with the various limit states.

To further verify the applicability of the equations for the performance level, the results of the calculation were applied to the hysteresis curves of the six specimens, as illustrated in Fig. 2-28. As can be seen, the calculated curves closely match the hysteresis curves.

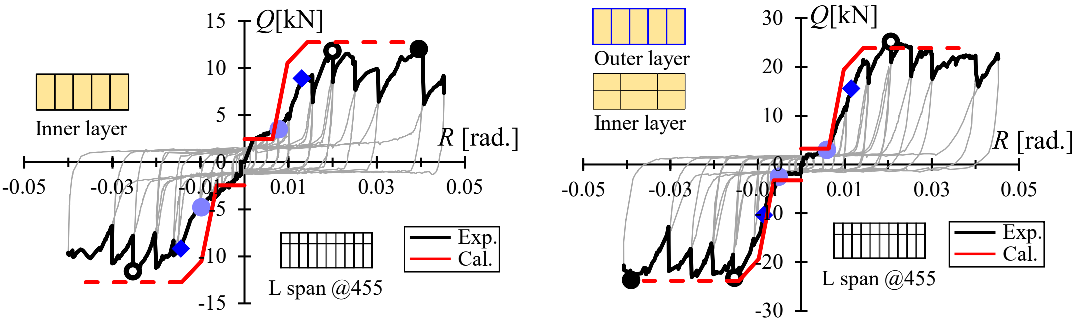

Specimen L12.5*1(V) Specimen L12.5*2@455

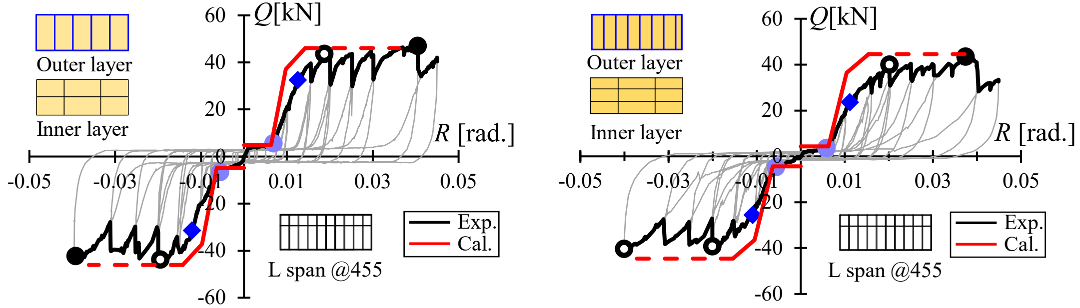

Specimen L12.5*4@455 Specimen L21*2

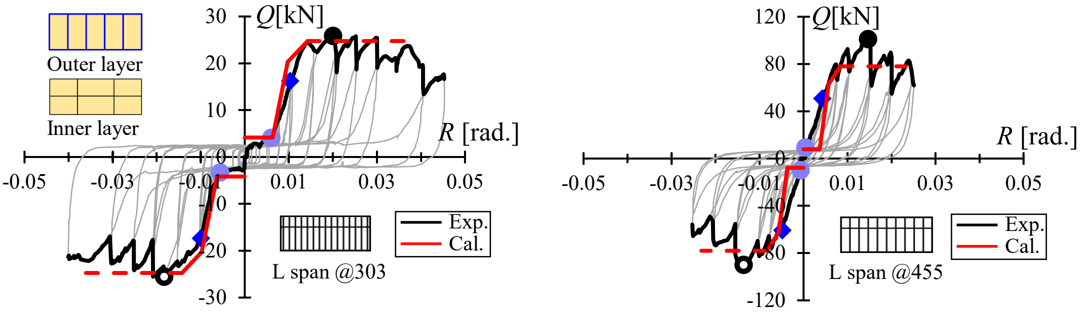

Specimen L12.5*4@303 Specimen No.1 (Isoda et al.[2-3])

Fig. 2-28. Performance levels for specimens.

2.4 The Connection Between the Concrete Slab and Track of the LGS Wall

At the end of this chapter, an experimental study of the connection between a concrete slab and the track of an LGS wall will be introduced. Although the LGS wall is one of the main subjects of this study, some discussion regarding its connection is also documented in this chapter.

2.4.1 Objectives

As one of the non-structural components, gypsum steel-stud partition walls are composed of metal tracks, cold-formed steel studs, and gypsum boards attached with self-drilling screws, and the tracks are usually connected to the deck plate by a power actuated fastener (PAF). In the present section, the shear strength of the PAF between the metal track and concrete slab is investigated to ensure the out-of-plane shear strength of gypsum steel-stud partition walls.

The research subject of this experiment is the joint between the metal track and the concrete slab located at the lower end of the LGS wall. The test specimen consists of a single PAF and a metal track, which is placed between two studs. The track is made of a metal track (SGCC) with a thickness of t_r = 0.8 mm or 2.3 mm, cold bent into a U-shape, and the width of the stud is 65 mm. Two types of tracks with a thickness of t_r = 0.8 mm are prepared, i.e., one with a flat web and the other with an embossed web. An overview of the tracks is shown in Fig. 2-29 and Fig. 2-30. In this paper, the two protruding plates of the track are called flanges, and the plate in contact with the concrete slab is called the web.

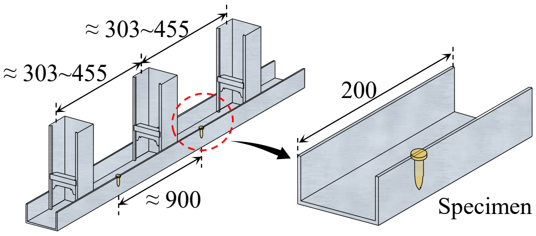

Fig. 2-29 Specimen

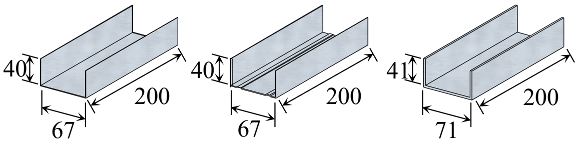

Thickness t_r=0. 8 (Flat)

Thickness t_r=0. 8 (Embossed)

Thickness t_r=2. 3 (Flat)

Fig. 2-30 (a): Parameter Metal track

In this paper, the two protruding plates that make up the track are called flanges, and the plate that contacts the concrete slab is called a web. The pins used in LGS walls are generally PAFs with diameters of 4 mm or less. Fig.2-30(b) shows the relationship between the diameter d_s and the length L_P of the PAF available from Max, Japan Power Fastening, and Hilti. It can be seen that the shape ratio of the PAF, L_P/d_s, is approximately in the range of 6 to 10. In this paper, two types of PAF with diameters of 2.6 mm and 3.0 mm are used, which consist of a flat cylindrical part and a conical tip. In this experiment, pins with length L_P=15-25 mm are selected from Max, Japan Power Fastening, and Hilti, and the PAFs are installed following the method of the corresponding company.

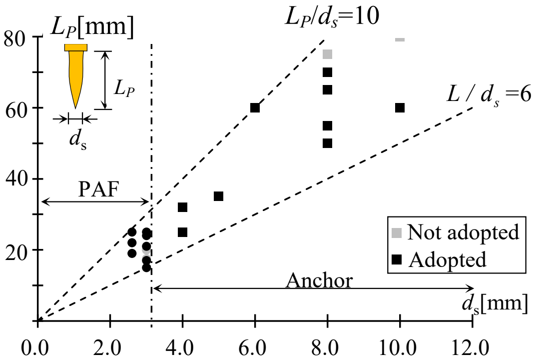

Fig. 2-30 (b): Parameter PAF

The concrete slab is prepared as a rectangular block with a compression strength of Fc=18 N/mm^2, a thickness of 150 mm, and a flat surface of 600 × 600 mm. The pins are placed at a distance of at least 35 mm from each other. The results of the material tests of the tracks are shown in Table 2-3, and the results of the material tests of the concrete are shown in Fig. 2-31(a). The vertical axis is the compressive strength of the cylinder specimen, σ_B, and the horizontal axis is the curing time (days). The compressive strength σ_B of the concrete during the experimental period is approximately 27 to 29 N/mm^2. The shear strength of the headed studs embedded in the concrete as well as the cast-in pins is evaluated by the "Guidelines for the Design of Composite Structures" [2-13] based on the results of push-out tests conducted by J.W. Fisher et al. In this paper, the bearing compression strength σ_c' of concrete at the PAF is evaluated by Eq. (2-19), which applies the above proposed equation.

$$\sigma_c{}' = 0.5 \cdot \sqrt{\sigma_B \cdot E_C} \qquad (2\text{-}19)$$

where E_C is the elastic modulus of concrete, σ_C' is the bearing strength of concrete, which is

Table 2-3 Material test result-metal track

	t_r=0. 8 (Flat)	t_r=0. 8 (Embossed)	t_r=2. 3 (Flat)
σ_y [N/mm^2]	280. 7	283. 2	292. 2
σ_{max} [N/mm^2]	360. 6	382. 9	370. 4

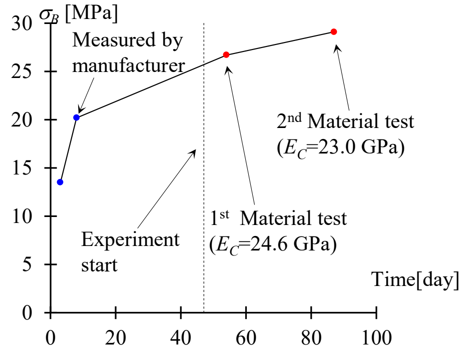

(a) Compression test results

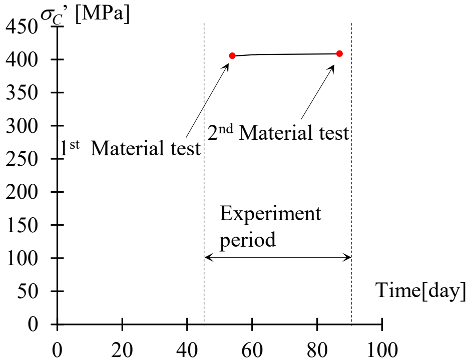

(b) Bearing strength of concrete cylinder

Fig. 2-31 Material test result-concrete slab approximately 405 N/mm^2 during the test.

2.4.2 Test setup

An outline of the test specimen is shown in Fig. 2-32. For the track, which is the test section, two stud jigs are inserted at both ends, and the front and back of the track's flange are sandwiched between loading jigs to form a rigid body, square-shaped loading jig. PC steel rods are connected to this jig, and monotonic tension loading is carried out using a center hole jack.

The experimental setup is shown in Fig. 2-33. The concrete slab, which serves as the base of the specimen, was placed on a self-balancing reaction frame, and the side of the specimen in the loading direction was in contact with the vertical jig. A horizontal jig was attached to the two vertical jigs, and a load cell and a center hole jack were installed on the side of the horizontal jig. Teflon sheets of 1 mm and 0.1 mm in thickness were placed between the track holding jig and the loading jig, and between the track and the concrete slab, respectively, to minimize the effect of friction during the experiment.

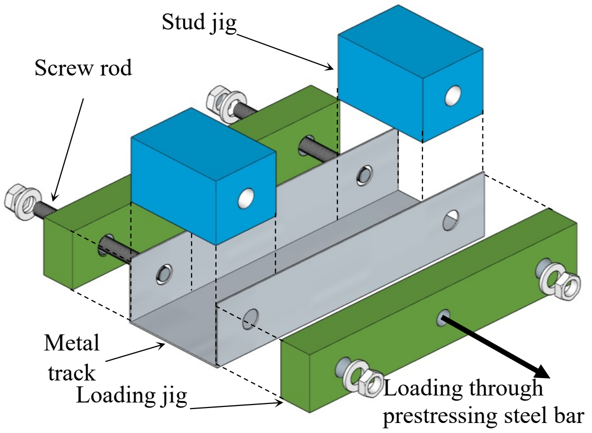

Fig. 2-32 Setup of loading jigs

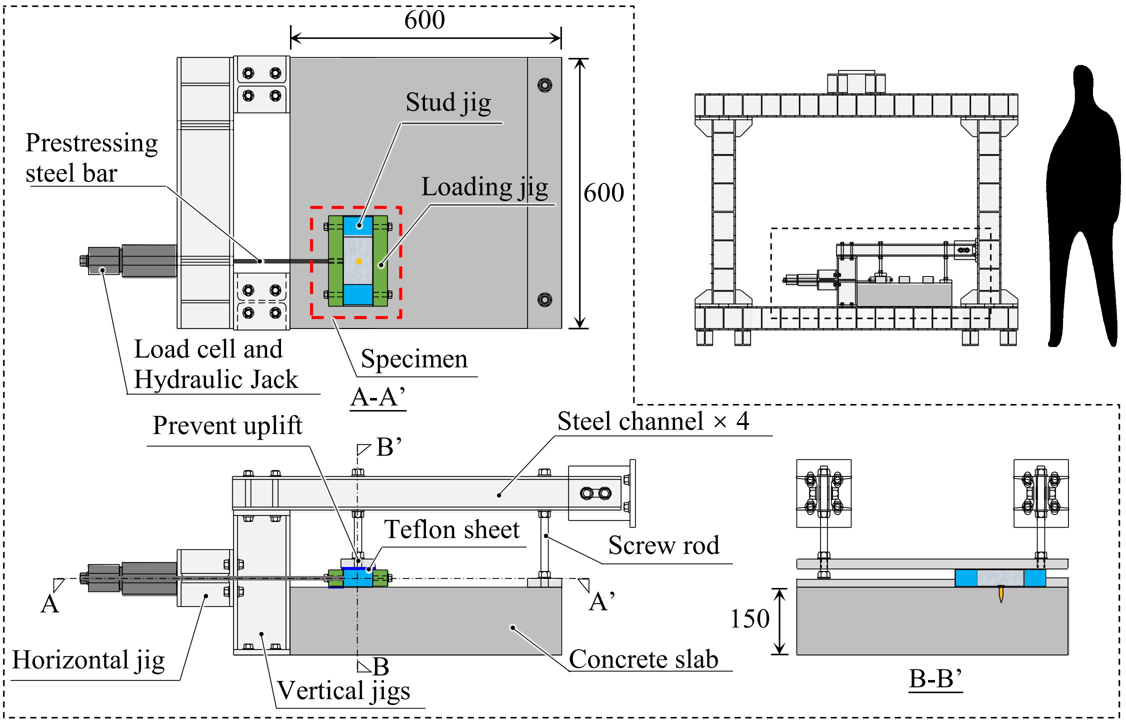

Fig. 2-33 Setup

2.4.3 Test Results

Three failure modes are observed during the test (Fig. 2-34). The first failure mode was the bearing failure of the track shown in Fig. 2-34(a), which shows, from left to right, the top surface of the track's web, the bottom surface, and the concrete slab with the track removed. The second failure mode was the pryout failure of concrete shown in Fig. 2-34(b). The third failure mode was the one in which both of the above failure modes were observed, i.e., bearing failure of the track web in the beginning, followed by the withdrawal of the PAF.

In the case of track thickness t_r=2.3 mm, most of the specimens failed to pryout of the concrete, as shown in Fig. 2-34(c). After the test, pressure failure of the concrete was observed at the front side of the applied force of the PAF, and very shallow cone-shaped cracks were observed at the back side.

In this study, the above failure modes are classified into the first two types and are judged from the shape of the load-deformation relation. An overview of the load-deformation relationship is shown in Fig. 2-35. The vertical axis represents the load, and the horizontal axis represents the horizontal deformation of the track. The yield strength is evaluated as the contact point between the 1/4 initial stiffness and the hysteresis curve. In the case of the track that failed under bearing pressure [Fig. 2-35 (a)], the plastic deformation progresses with strain hardening between the yield strength (●) and the maximum strength (●). On the other hand, in the specimen where the concrete reached pryout failure (Fig. 2-35(b)), there is almost no difference between the yield strength and the maximum bearing capacity, and the specimen shows almost elastic behavior before sudden failure. These judgments are in general agreement with the post experimental observations.

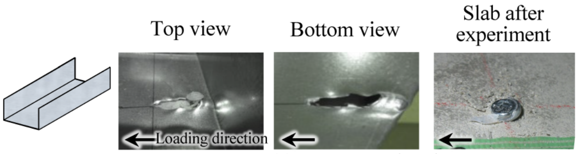

(a) t_r=0. 8mm, bearing

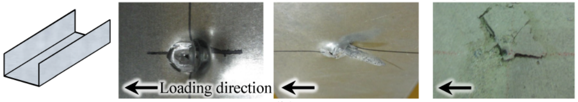

(b) t_r=0. 8mm, pryout

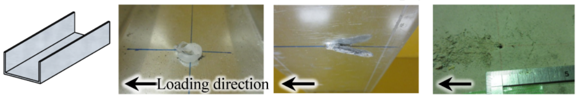

(c) t_r=2. 3mm, pryout

Fig. 2-34 Typical damage pattern after loading

In this experiment, three specimens with the same combination of track and PAF were prepared for each test. The hysteresis curves of the specimens with the same combination are illustrated in Fig. 2-36. In the figure, the result of track failure is shown by the solid black line, and the result of concrete pryout failure is shown by the solid red line. Even for the same combination of specimens, there are variations in yield strength and maximum strength, and in some cases, the failure modes were different. On the other hand, there is no clear difference due to the embossing of the track's web.

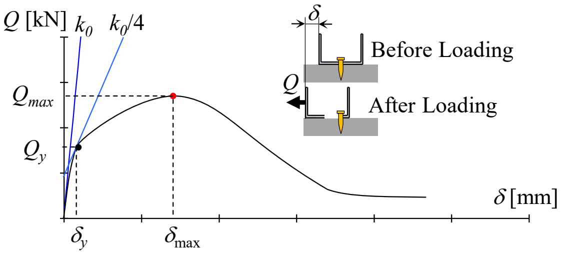

(a) Metal track bearing failure

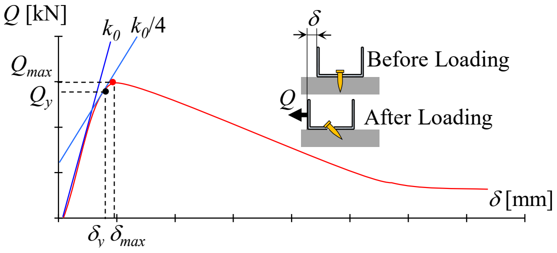

(b) Pryout

Fig. 2-35 Definition of damage pattern

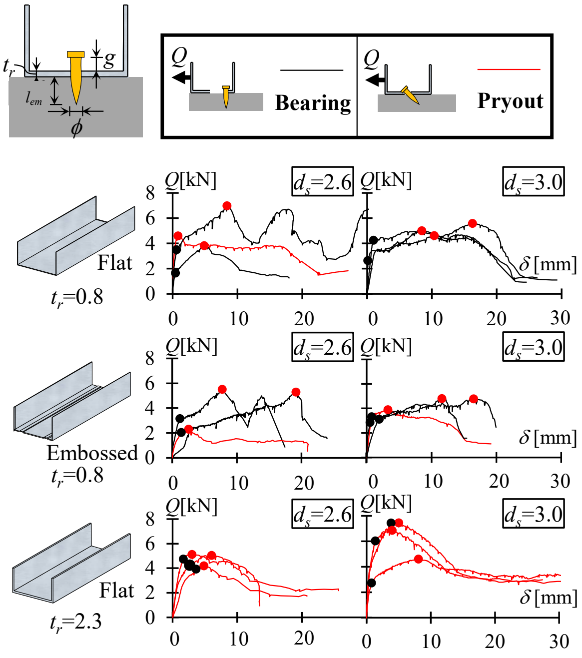

Fig. 2-36 Typical test results

The evaluation of the bearing capacity are then discussed. The bearing capacity ratio (maximum bearing capacity/yielding capacity) and the deformation ratio when the bearing capacity is reached are shown in Fig. 2-37 in relation to the embedment length l_{em} (=L_P-g-t_r). g is the dimension from the bottom of the head of the embedded pin to the top of the track's web (Fig.2-36).

In the case of the specimen with t_r=0.8 mm, the maximum bearing capacity is in the range of 1.0 to 2.5 times the yield strength, and there is no correlation with the embedment length l_{em}. However, in specimens without pryout failure, the yield strength and the maximum bearing capacity are almost the same. In the case of pryout failure, the plastic deformation is 3 to 20 times larger than the deformation at the yield strength before reaching the maximum bearing capacity. Therefore, it is appropriate to use the yield strength as the design bearing capacity in the case of pressure failure and the maximum bearing capacity in the case of pryout failure.

In the case of the specimens with t_r=2.3 mm, most of the specimens achieve pryout failure, and the maximum bearing capacity Q_{max} is in the range of one to two times the yielding capacity Q_y. The maximum bearing capacity Q_{max} is in the range of 1 to 2 times the yield strength Q_y. Similarly, the deformation at maximum bearing capacity d_{max} is in the range of 1 to 5 times the deformation at yield strength d_y. The yield bearing point and the maximum bearing point are closer to each other than in the case of a thin track with a thickness of t_r=0.8 mm.

The relationship between the yield strength Q_y and the diameter ds of the driving pin obtained from the experiment is shown in Fig. 2-37. In AISI [2-14], the bearing strength Q_B of the metal track is given by Eq. (2-20).

$$Q_B = \alpha \cdot t_r \cdot d_s \cdot \sigma_y \qquad (2\text{-}20)$$

Fig. 2-38 shows the results of the calculation using the AISI equation. The calculated results are shown in Fig.2-38. The experimental results are higher than the calculated results, indicating that the calculated results are the lower limit of the experimental results.

The amplification factor α in the experiment is calculated by substituting the yield strength Q_y

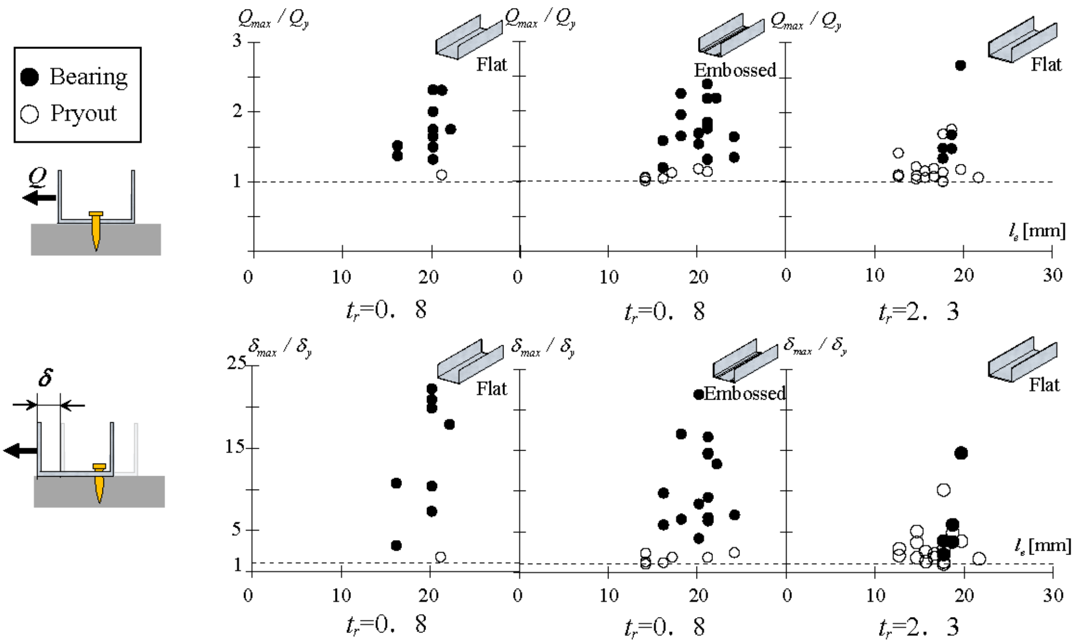

Fig.2-37 Ratio of the maximum force point to yield point

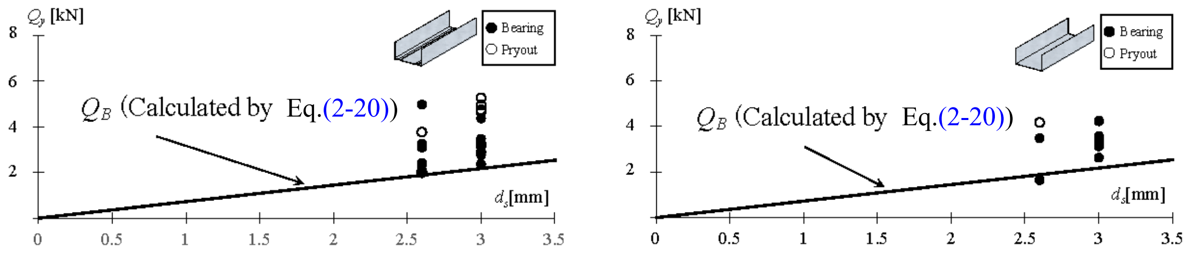

Fig.2-38 Bearing strength of metal track.

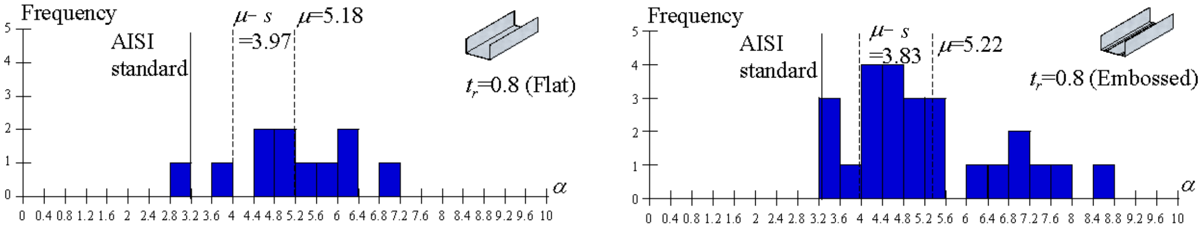

Fig.2-39 Frequency of distribution.

obtained from the experiment for Q_B in Eq. (2-20), and its frequency distribution is shown in Fig. 2-39. The frequency distribution is shown in Fig. 2-39. The mean value of the amplification factor is μ and its standard deviation is s, the value of 3.2 in the AISI equation is lower than μ-s.

Next, the evaluation of the bearing capacity of pryout failure is discussed. Fig. 2-40 shows the mechanical model used in the evaluation. It is assumed that the PAF is subjected to a concentrated load Q from the center of the track web thickness. The cast-in pin is considered to be an embedded column foot embedded in the concrete slab, and the stress distribution at the yield bending capacity is assumed according to the "Design Guidelines for Steel Structure Connections" [2-15]. The PAF is subjected to a reaction force R_U on the forward side of the applied force in the concrete slab and a reaction force R_B in the opposite direction below the PAF. Assuming that the stress range of the reaction force R_U is x and that the stress level on the concrete slab top surface has reached the bearing strength σ_c', the reaction forces R_U and R_B can be obtained from the following equation. The edge stress on the side of the reaction force R_B can be obtained from the geometric relationship.

$$R_U = \frac{1}{2} \cdot d_s \cdot x \cdot \sigma_c' \qquad (2\text{-}21)$$

$$R_B = \frac{1}{2} \cdot d_s \cdot (l_e - x) \cdot \sigma_c' \cdot \frac{l_e - x}{x} \qquad (2\text{-}22)$$

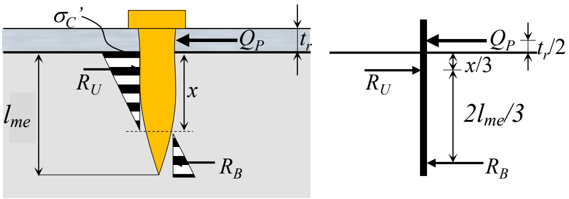

Fig. 2-40 Pryout force distribution

Assuming that the bearing capacity at the time of pryout failure is Q_P, the balance of forces in the horizontal direction and the balance of moments on the top surface of the concrete slab can be expressed by the following equations.

$$Q_P + R_B = R_U \qquad (2\text{-}23)$$

$$Q_P \cdot \frac{1}{2} t_r = R_B \cdot \left(\frac{x}{3} + \frac{2l_{em}}{3}\right) - R_U \cdot \frac{x}{3} \qquad (2\text{-}24)$$

By rearranging equations (3) to (6) for QP, the following equation can be obtained.

$$Q_P = \frac{\sigma_C' \cdot d_s \cdot l_{em}^{\;2}}{2(3t_r + 2l_{em})} \qquad (2\text{-}25)$$

This is the bearing capacity when the stress on the top surface of the concrete slab reaches the bearing strength σc'. In other words, the equation is derived from the observation of the fracture state after the experiment, which shows that the concrete support pressure failure is observed on the forward side of the applied force.

Comparison of experimental and calculated results

Fig. 2-41 shows the maximum bearing capacity Q_{max} of the specimens that failed in the pryout condition in relation to the embedment length l_{em}. In the figure, the calculation result by Eq. (2-25) is shown with a solid line, and the calculation result of yield strength by Eq. (2-20) is shown with a dashed line.

Both experimental results exceed the calculated results assuming pryout failure. In Section 2.4.3, it was shown that the metal track has a residual strength between the yield strength and the maximum strength when the metal track fails under pressure using Eq. (2-20). Therefore, in this type of joint, it is desirable to use the evaluation of the bearing capacity for each failure mode and select the diameter and embedment length of the PAF according to the thickness of the metal track to cause the metal track failed under bearing strength.

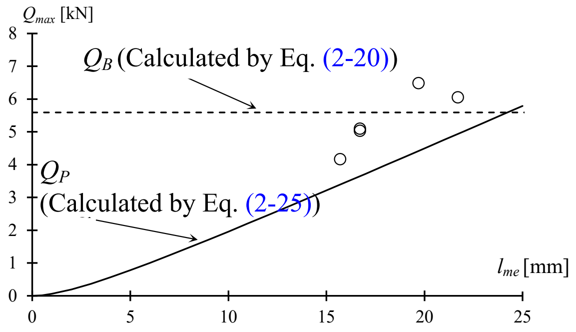

(a) d_s=2. 6mm

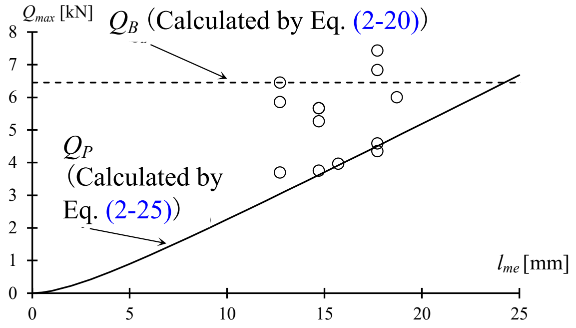

(b) d_s=3. 0mm

Fig. 2-41 Shear strength of pryout specimens

2.5 Summary and Conclusions

An experimental study was carried out on a light-gauge-steel partition drywall, which is a type of interior drywall partition system widely used for frame buildings worldwide. This study focuses on LGS walls built according to Japanese practice, which features a sliding-joint track-stud connection. Fifteen full-scale LGS wall specimens of various span lengths and panel thicknesses were subjected to lateral cyclic loading. The following conclusions can be drawn based on the test results.

(1) After establishing clearance between the gypsum-panel ends and allowing the stud to slide into the metal track, the Japanese practice is considered to significantly delay local compression of the gypsum panel.

(2) All the specimens were predominated by a slip of the gypsum panel because of the sliding track -stud joint. Two failure modes of the LGS wall were observed during the test: One was the relative slip between the upper and lower gypsum panels, which was observed on the one-layer horizontally placed gypsum panel specimens. However, this failure mode may cause out-of-plane failure of the LGS wall; thus, designs using a horizontal configuration with only one layer should be avoided. The other failure mode is due to a local compression of the gypsum panel, which was observed on the two- and four-layer gypsum panel specimens. Although both ends of the panels had local compressive damage, the panel remained intact in the out-of-plane direction.

(3) For the n =1 and n =2 or 4 specimens, the degree of damage correlated with the envelope curves. At the initial stage, when the gypsum panel was not in contact with the loading frame, no significant damage to the specimens was observed. A significant increase in the stiffness occurred when the gypsum panel contacted the loading frame. When the stiffness was increased, only minor damage, such as compressive wrinkles of the gypsum panel, was observed. However, as the stiffness started to decrease, significant damage was gradually observed.

(4) Particular attention was placed on an analysis of the gypsum panel performance, and characteristics of the failure modes of the panel and performance levels were defined to judge the limitation to repairs. Equations were proposed to predict the strength, stiffness, and story drift ratio of each characteristic point of the damage limit states, and the equations of the story drift ratio provided safe-sided results. The damage limit states of the LGS wall can be identified using the story drift ratio associated with a specific degree of damage derived from the results of the in-plane cyclic tests for LGS wall.

Reference

[2-1] Standard Specification of Public Construction Work (Construction Work), Ministry of Land, Infrastructure, Transport and Tourism (Japan), 2019. (In Japanese)

[2-2] JIS A 6517. Japanese Industrial Standards A6517, building steel substrate material, 2020.

[2-3] Isoda M., Oki Y., Tatsumi N., Kishiki S., Ishihara T., Behavior of LGS partition walls against in-plane relative displacements and out-of-plane inertial forces. Proceeding of constructional steel Vol.29, Japanese Society of Steel Construction, Tokyo, 2021. (In Japanese)

[2-4] Lee T., Kato M., Matsumiya T., Suita K. and Nakashima M. Seismic performance evaluation of non-structural components: Drywall partitions. Earthquake Engineering and Structural Dynamics, 36(3): 367-382. https://doi.org/10.1002/eqe.638.

[2-5] Tasligedik A., Pampanin S., and Palermo A. Low damage seismic solutions for non-structural drywall partitions. Bulletin of Earthquake Engineering, 13(4):1029-1050. https://doi.org/10.1007/s10518-014-9654-5

[2-6] Pali T., Macillo V., Terracciano M., Bucciero B., Fiorino L., and Landolfo R. In-plane quasi-static cyclic tests of non-structural lightweight steel drywall partitions for seismic performance evaluation. Earthquake Engineering and structural dynamics, 47(6): 1566-1588.

[2-7] Tamura K., Kaneko M., Kambara H., Shiohara H., Terada T. Static Loading Tests on Partition walls with Light Gage Steel. Summaries of Technical Papers of Architectural Institute of Japan Annual Conference, Sep.2006, pp.985-986. (in Japanese)

[2-8] Kumazawa F., Wakiyama Y., Kato H., Mukai T., Tajiri S. and Adachi K., Full-scale loading test on a RC building focus on reparability and serviceability Part 9 Characteristics of partition walls and interior doors. Summaries of Technical Papers of Architectural Institute of Japan Annual Conference, Sep.2012, pp.1275-1278. (in Japanese)

[2-9] Mitani H. Hayashi T., Kawachi T., Ohuchi W. and Hayashi Y., Seismic tests for partition walls of a multiple dwelling house Part 1 outline of tests. Summaries of Technical Papers of Architectural Institute of Japan Annual Conference Sep. 2011, pp.751-754. (in Japanese)

[2-10] Suzuki et al., experimental study on fire resistance of damaged partition wall, part 1 experimental outline. Summaries of Technical Papers of Architectural Institute of Japan Annual Conference Sep. 2010, pp.145-146. (in Japanese)

[2-11] Sato Y., Ogawa M., Hatori T., Motoyui S., Development of Reduction Method for Seismic Damage to LGS Partition Wall, Part6. Study on the material property of gypsum board. Academic proceedings of Architectural Institute of Japan (AIJ) annual national meeting, pp.1419-1420, Hokuriku, Japan; 2019. (in Japanese)

[2-12] JIS A 5538. Japanese Industrial Standards A5538, Adhesives for walls and ceilings, 2003.

[2-13] Architectural Institute of Japan, Design Recommendations for Composite Constructions, pp. 91-101. 2010 (in Japanese).

[2-14] AISI (American Iron and Steel Institute).（2012). North American specification for the design of cold-formed steel structural members．AISI S100-12,Washington,DC

[2-15] Architectural Institute of Japan, Recommendation for Design of Connections in Steel Structures, pp. 336-350, 2012 (in Japanese).

3. Experimental Study on Masonry Infilled Timber Frames

3.1 Introduction

The beginning of this chapter will introduce an experimental study of masonry infilled timber frame, after which it will mainly discusses the contribution of masonry infill. Although masonry infill is one of the main subject of this study, some discussions of its timber frame will also be documented in this chapter.

The Chuandou timber frame system has a history of approximately 500 years and remains one of the currently widely used timber structural systems in southwestern China. It was historically infilled with timber panels or wattle and daub panels while clay brick masonry has been overwhelmingly preferred for the infills over past few decades for its low cost and easy construction Fig. 3-1. Compared with other traditional timber systems in China, it is distinguished by the following features: (1) the timber beams and columns are joined by penetration tenons, where the full section of a beam goes through the mortise on the column; (2) it uses no timber braces but is infilled with masonry or wood panels as the partitions; (3) the columns stand freely on independent base stones and there are neither sills nor mechanical anchors at the column bases. Through in-site observations immediately after the 2013 M7.0 Lushan earthquake in China, Qu et al. [3-1] found that the Chuandou frames exhibited better seismic performance than un-reinforced masonry structures in terms of collapse prevention, although they sustained damage of various types, including the collapse of the masonry infills [Fig. 3-2(a)], excessive slip of the free-standing columns at the base [Fig. 3-2(b)]; fracture of beam tenons [Fig. 3-2 (c)] and pull-out of beam tenons [Fig. 3-2(d)].

The wide spread of Chuandou timber houses in southwestern China, especially in the mountainous areas, may have benefitted from its low cost, easy access to the materials, and quick construction with only man power. The independent column bases without sills make it especially fit for sloped, narrow and irregular sites, which are very common in mountainous areas. Notwithstanding the fact that the southwestern China is highly prone to earthquakes, very limited studies have been conducted on the seismic performance of Chuandou timber frames. Chang et al. [3-2] conducted a monotonic loading test on cantilever timber beams with different types of penetration tenons and proposed a model to predict the rotational stiffness of the penetration tenon connections in Chuandou frames. Chen [3-3] investigated the methods to strengthen the timber penetration tenons by either carbon -fiber-reinforced polymer sheets or steel plates. Monotonic loading tests on cantilever beams showed that both methods would significantly increase the joint stiffness.

Huang et al. [3-4] conducted a series of cyclic loading tests to investigate the seismic behavior of full-scale two-bay Chuandou timber frames with timber, wattle or daub infills. The specimen with timber infills exhibited higher lateral stiffness and strength than that of the others. All these studies have focused on the mechanical properties and retrofit of the timber frame itself, whereas little is known about the masonry-infilled timber frame, in which the masonry infill is supposed to provide most of the

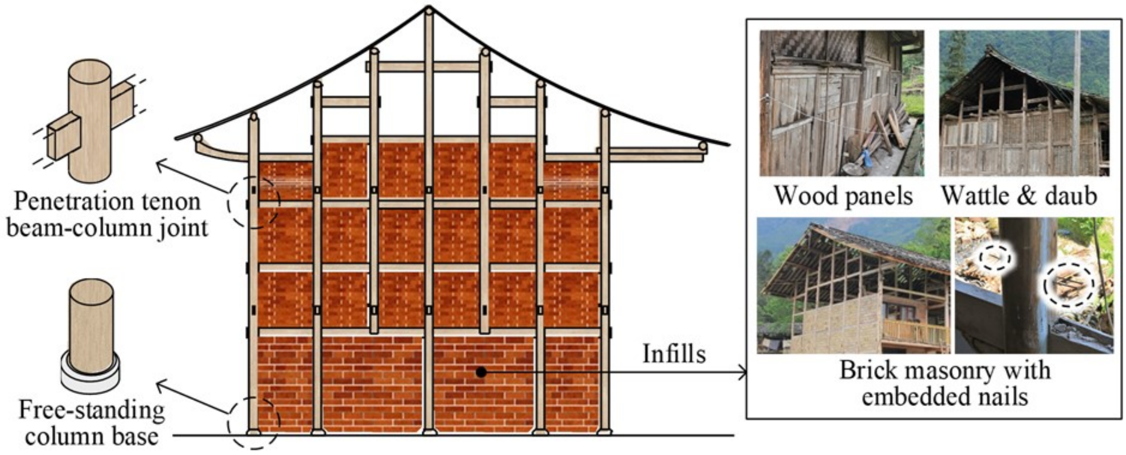

Fig. 3-1. Configuration of an infilled Chuandou timber frame.

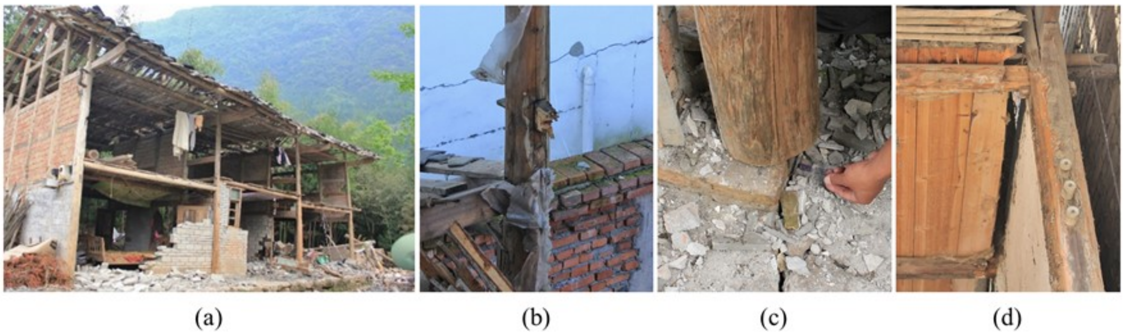

Fig. 3-2. Damage to masonry-infilled Chuandou timber frame after 2013 Lushan earthquake in China[1-18]: (a) Collapse of the masonry infills; (b) sliding at column base; (c) fracture of beam tenon and (d) pull-out of beam tenon.

seismic resistance.

The present study intends to investigate the seismic behavior of Chuandou timber frames with masonry infills, which have become the most popular type of infills of timber frames in recent decades in South China. Several full-scale specimens of single story-one bay Chuandou frames were subjected to in-plane cyclic loading. Combined with the results of many previous experiments, the in-plane drift demands of masonry infill walls were evaluated and verified. The details of the specimens, testing method and primary findings are reported in the following sections.

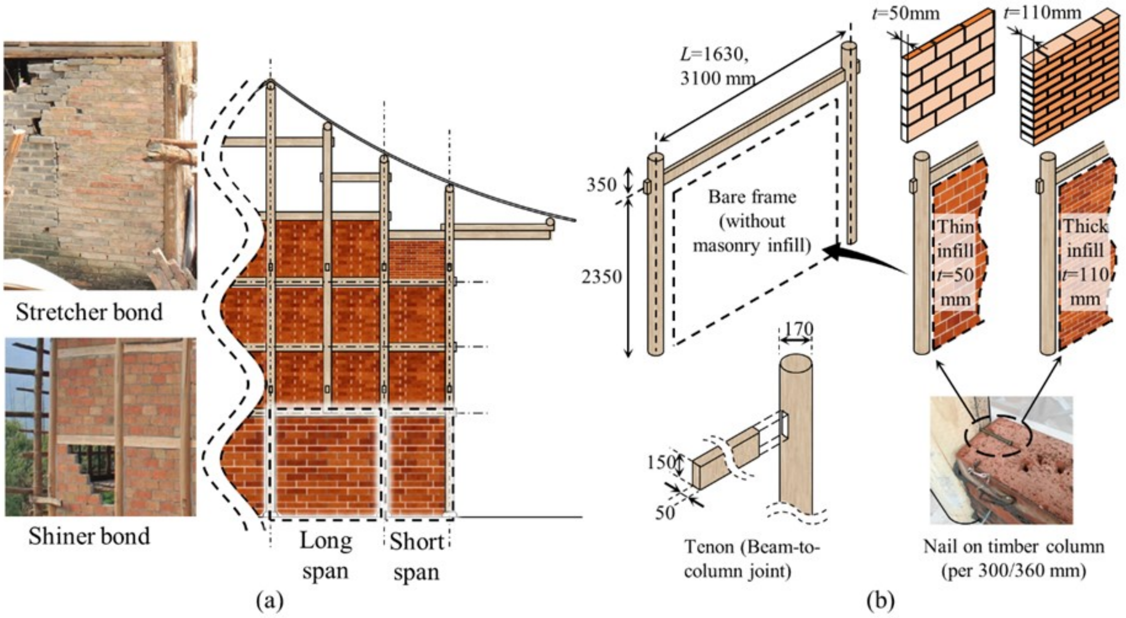

Fig. 3-3. (a) prototype Chuandou frame and (b) specimen dimensions (unit: mm).

3.2 Test plan

3.2.1 Specimens

Six specimens were designed and built in the lab by local workers following the construction practice of Chuandou frames in Lushan, China. The specimens, including their dimensions, cross-sections and detailing, were designed so that they reproduce full-scale subassemblies of a prototype Chuandou timber frame in the local area [Fig. 3-3(a)]. All specimens had the identical story height of H=2350 mm, which is the distance from the column base to the axis of the beam, and the masonry infills were made of a single-wythe of 230×110×50 mm fired clay bricks with a running bond. The aspect ratio (H/L) and wall panel thickness (t) were selected as the parameters of the specimens. Two typical aspect ratios of the masonry panels in Chuandou timber frames were used to represent the panel in either a long span or a short span. For each aspect ratio, three specimens were prepared, including a bare frame specimen and two masonry-infilled specimens in which the masonry panel was laid either in a stretcher bond (thickness t=110mm) or a shiner bond (thickness t=50mm) according to the local practice of construction. Each timber frame consisted of two columns and a beam. The columns had a circular section of 170 mm in diameter, and the beam had a rectangular section of 50 mm wide and 150 mm deep [Fig. 3-3(b)]. The beam went through the mortises on the columns, which were slightly bigger than the cross-section of the beam so that the beam can fit into the mortise.

Following the local construction practice, the masonry infill was connected to the timber columns by plain nails at approximately 300-mm and 360-mm spacing for the thick and thin wall specimens, respectively. The gap between the infill and the timber columns was filled by mortar. The parameters of the specimens are summarized in Table 3-1.

Table 3-1. Specimen parameters

ID	L (mm)	H/L	t (mm)	Shear key
L0	3100	0.76	-	No
L50	3100	0.76	50	Yes
L110	3100	0.76	110	Yes
S0	1630	1.44	-	No
S50	1630	1.44	50	Yes
S110	1630	1.44	110	Yes

3.2.2 Material properties

According to the Chinese Standard for the Testing Method of Performance on Building Mortar[3-4], the compressive strength of the mortar (a 1 : 3.2 : 0.27 mix of cement, sand and accelerator) in the masonry infill, σ_m, was tested on 70.7 mm cubes [Fig. 3-4(a)]. The bond-slip strength of the masonry τ_0 was obtained by direct shear tests on blocks of three bricks bonded by two mortar beds without applying any transverse restraint [Fig. 3-4(b)], and the masonry compressive strength σ_M was tested on blocks of four bricks with three mortar beds [Fig. 3-4(c)]. Both the compression and shear strengths were tested on masonry coupons of a stretcher bond, and were calculated as the measured force divided by the corresponding areas. The mortar bed was approximately 8-10 mm thick in all tests. Three coupons were tested, and the average result was taken as the material property. It was assumed that the masonry strength is the same for a shiner system. For each material property, three masonry coupons were tested on the same day as the loading of each specimens. The average material properties for each masonry-infilled specimen are summarized in Table 3-2. The average strengths and their standard deviations over all masonry-infilled specimens are also listed in the table.

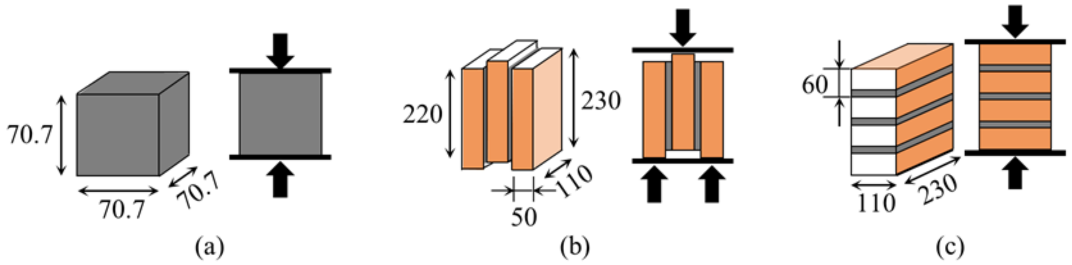

Fig. 3-4. Dimensions of samples in testing (a) mortar compressive strength σ_m, (b) masonry bond-slip strength v_{te} and (c) masonry compressive strength σ_M (Unit: mm).

The material properties of the timber were tested according to the Chinese codes for the testing methods of timbers in bending [3-5] and in compression [3-6] with some revisions on the dimensions of the test coupons. In particular, small timber coupons of 20-by-20 mm cross sections are adopted by the code methods, but coupons of 120-by-120 mm cross-sections that represent the inscribed square of the full-scale column cross section in the test were used to minimize the size effect in the material properties. The average bending strength was 30.08 MPa and the elastic modulus E_B was 3.87 GPa at an average moisture content of 14.6% by three-point bending tests of six 120-by-120-by-2400-mm timber beam coupons. The average compressive strength and elastic modulus E_{com} parallel to the grain of 120-by-120-by-240-mm timber cuboids were 25.92 MPa and 5.65 GPa, respectively, at an average moisture content of 9.4%. During the test of the timber frame specimens, the moisture content of the timber varied from 7.7% to 10.2% with an average of 8.3%.

Table 3-2. Material properties of mortar and masonry

Specimen	Masonry		
	σ_m (MPa)	v_{te} (MPa)	σ_M (MPa)
L50	7.30	0.23	4.54
L110	8.21	×	9.93
S50	5.58	0.18	3.66
S110	6.19	0.19	5.44
Mean	6.82	0.20	5.89
Standard deviation	1.10	0.08	2.71

×: test failed

3.2.3 Test setup

For all specimens, the timber columns stood freely on top of a reinforced concrete foundation block with roughened surface at the location of the column bases. A small slip was expected at the column bases of the bare frame specimens, while the column may be pushed outside by the toes of the wall panels and exhibit excessive lateral slip, which would be restrained by a wall panel in the adjacent span if it were in a real Chuandou frame. In the test, a pair of metal shear keys was installed to impose an upper limit of approximately 20 mm on the lateral slip at the column bases for the masonry-infilled specimens (Fig. 3-5).

A lateral load was applied to the timber columns by a 300-kN hydraulic jack along the axis of the timber beam. The jack was connected to the columns through specially designed jigs to avoid touching the penetration tenons of the beam-to-column joints. The two jigs on both columns were connected by a pair of steel rods on both sides of the beam to transfer the force of the jack to the jig at the far end in negative loading. The timber columns were connected to a steel beam at the top through a pair of mechanical hinges. Two pantographs were installed on both ends of the steel beam for the out-of-plane stability.

The total weights of the steel beam, specially designed jigs, steel rods, pantographs and mechanical hinges were approximately 8.0 kN. To simulate the dead load of the superstructure, an additional gravity load of 25.4 kN was applied to the steel beam by steel blocks, resulting in a total gravity load of 33.4 kN in addition to the self-weight of the masonry-infill timber specimens. Therefore, each timber column in the wide-span specimens was subjected to 16.7 kN additional axial force, while in the narrow-span specimens, one column was subjected to 14.3 kN and the other was subjected to 19.1

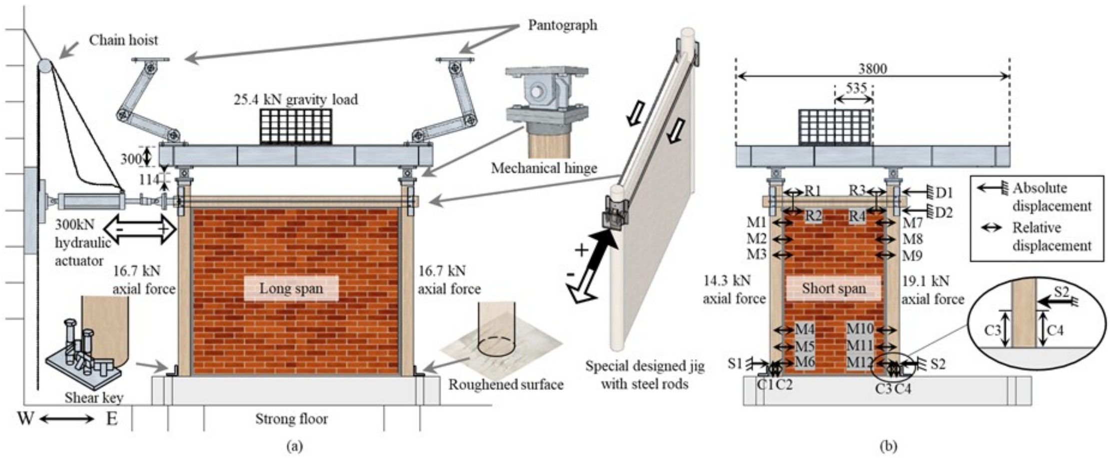

Fig. 3-5. Test setup: (a) long span, (b) short span (length unit: mm).

kN additional axial force because of the eccentricity of the top steel beam [Fig. 3-5(b)]. The difference in the column axial forces of the short-span specimens is deemed to have little effect on the behavior of the beam-to-column joints, which is governed by the properties of the beam, whereas its effects on the overturning moment of the free-standing columns of bare frame specimens and the rocking strength of the masonry-infilled specimens are considered in the calculations in the following sections. In determining the amount of addition gravity load, a combined gravity load [3-7] of (1.0DL + 0.5LL) = 1.95 kN/m2 was assumed, in which DL = 1.8 kN/m2 is the dead load and LL = 0.3 kN/m2 is the live load according to existing statistics for Chuandou houses in the literature [3-8]. The range of column axial forces of 14.3 to 19.1 kN corresponds to a 7 to 10 m2 tributary area of a single column, which is realistic for commonly-seen Chuandou houses.

The locations of the displacement transducers are also shown in [Fig. 3-5(b)]. The two transducers D1 and D2 were mounted near one of the beam-to-column joints to measure the lateral drift Δ of the frame, which is calculated by Eq. (3-1). The rotation of the two beam-to-column joints were obtained by two pairs of transducers R1-R4. Twelve transducers, M1-M12 were installed horizontally at the timber columns-to-masonry interfaces to measure the gap opening. The sliding of the column bases was measured by transducers S1 and S2 near the column bases. The rotation of each column was measured by transducers C1-C4.

$$\Delta=\frac{\Delta_{D1}+\Delta_{D2}}{2} \qquad (3\text{-}1)$$

where Δ_{D1} and Δ_{D2} are the lateral displacements recorded by displacement transducers D1 and D2 as shown in [Fig. 3-5(b)].

Cyclic loading was performed with increasing amplitudes of story drift ratios R=Δ/H from 0.125% to 10% (Fig. 3-6). The drift amplitudes were in accordance with the ISO/TC 165 WD 16670 [3-9], and two cycles of loading were performance for each amplitude. The maximum R was up to 8% in the negative loading direction because of the limitation of the stroke of the jack. For the bare-frame specimens S0 and L0, the very small drift amplitudes were skipped and the loading started from an amplitude of 0.5% story drift ratio.

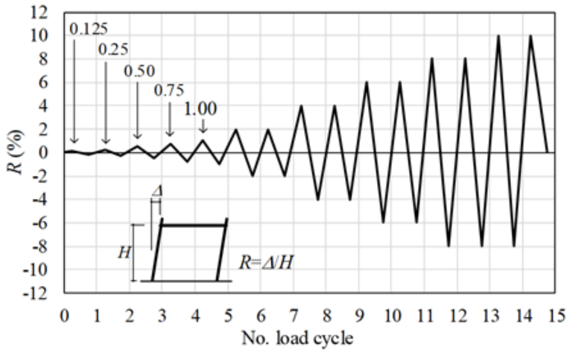

Fig. 3-6. Loading protocol.

3.3 Hysteretic behavior and failure modes

3.3.1 Bare frame specimens

The hysteretic curves of the lateral force *Q* and story drift ratio *R* of the bare-frame specimens S0 and L0 are shown in Fig. 3-7. The *P-Δ* effect on the lateral force is compensated. The results in the negative loading direction was affected by the mis-operation of the chain hoist that hung the hydraulic jack. The chain hoist, which was installed diagonally between the jack and the reaction wall (Fig. 3-5), was not sufficiently loosened during the test and imposed an unintended force on the jack in the negative direction, whose horizontal component added to the jack force recorded by the load cell in series with the piston of the jack. Therefore, the lateral force results in the negative direction for the bare frame specimens were deemed unreliable and will not be included in the following discussion. The displacement results were not affected by this issue because the loading was controlled by separately monitored displacement. The hysteresis of both timber frames exhibited significant pinching, which is a commonly-observed behavior for timber frames and was deemed to be attributed to the initial gaps in the mortise-tenon joints and the residual compressive deformation when the beam tenons were squeezed parallel to the grain [3-10][3-11][3-12]. A significant stiffness reduction was observed on the envelope curves at approximately 1% and 3% story drift ratios for specimens S0 and L0, respectively, beyond which both specimens continued to sustain the lateral strength without losing the vertical stability up to 10% story drift ratio. In particular, the lateral force *Q* in specimen S0 continued to increase beyond the point of apparent stiffness reduction and reached a maximum lateral force of 3.7 kN at 10% story drift ratio, at which the jack run out of its stroke and the testing was terminated. On the other hand, the lateral strength of specimen L0 was 2.4 kN, which took place at a story drift ratio of 4%.

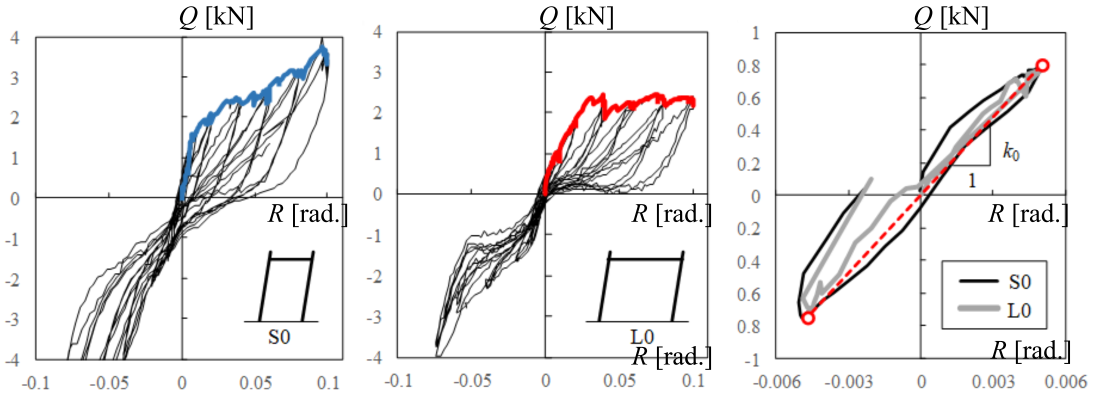

(a) (b) (c)

Fig. 3-7. Hysteretic and envelope curves of bare frame specimens: (a) S0, (b) L0 and (c) first cycle of both.

The hysteretic curves in the first loading cycle of the bare-frame specimens are compared in [Fig. 3-7(c)] to show that the two bare-frame specimens exhibited very similar initial stiffness regardless of their different spans. The initial lateral stiffness derived by the slope of the straight line that connects the peak points was 159.6 kN/rad. It rises from the frame action of the bare frame that relies on the rotational resistance of the beam-to-column joints and column base joints. In contrast to the extensively investigated beam-to-column joints in a timber frame, the role of free-standing column bases in the initial stiffness of a timber frame remains unclear. Taking advantage of the measured displacements at the column bases in specimens S0 and L0, the equivalent stiffness of the column bases in the first cycle of loading is calculated to show that neither a pin nor a fixed base assumption can be considered realistic.

The uplift and rotation of the column bases can be calculated from the displacements at the column bases be Eqs. (3-2) and (3-3), respectively.

$$\delta_N = \frac{\Delta_{C1} + \Delta_{C2}}{2} \tag{3-2}$$

$$\delta_N = \frac{\Delta_{C1} + \Delta_{C2}}{2} \tag{3-3}$$

where Δ_{C1} and Δ_{C2} are the lateral displacements recorded by transducers C1 and C2 as shown in [Fig. 3-5(b)]; *B* is the distance between the two transducers C1 and C2 (Fig. 3-8).

The height of the compression zone of the column section, which is taken as the part that falls below the grade level in Fig. 3-8, can then be calculated by Eq. 3-4.

$$x_0 = r - \frac{\delta_{\mathrm{N}}}{sin\,\theta_{\mathrm{CB}}} \tag{3-4}$$

where *r* is the radius of the circular column section.

By assuming a triangular distribution of compressive stress within the compression zone, we determined the action point of the resultant reaction force (Fig. 3-8). It counteracted the axial force N of the column and produced a moment of $M_{\mathrm{CB}}=N \cdot j$ at the column base, where j is the distance between axial force N and the reaction force. Therefore, the rotation stiffness of the column base joint can be calculated by Eq. (3-5). The calculation results are summarized in Table 3-3.

$$k_{CB} = \frac{M_{CB}}{\theta_{CB}} \tag{3-5}$$

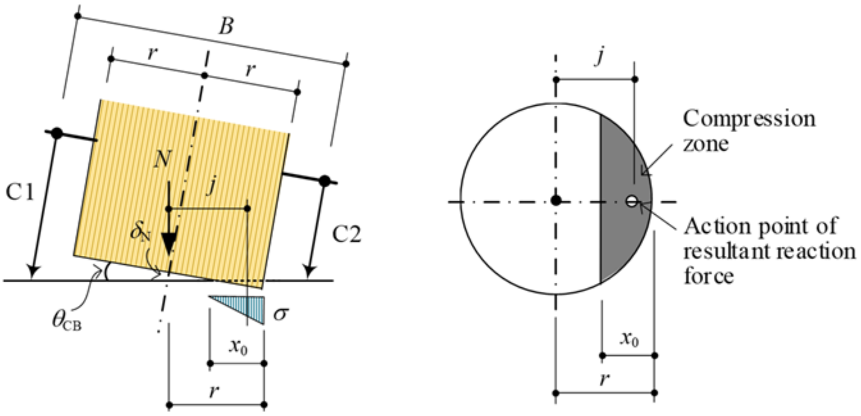

Fig. 3-8. Calculation of moment and rotation at free-standing column base.

Table 3-3. Evaluation of column base stiffness by test data

	Long-span bare frame L0				Short-span bare frame S0			
	R = +0.5%		R = -0.5%		R = +0.5%		R = -0.5%	
	West	East	West	East	West	East	West	East
N (kN)	17.1	17.1	17.1	17.1	14.7	19.5	14.7	19.5
δ_{N} (mm)	0.10	0.10	0.03	0.02	0.20	N/A	0.15	N/A
θ_{CB} (rad)	0.44%	0.38%	0.39%	0.35%	0.54%	N/A	0.54%	N/A
x_0 (mm)	62.4	59.9	77.0	79.7	47.3	N/A	57.8	N/A
j (mm)	58.1	59.1	51.8	50.6	64.6	N/A	60.0	N/A
k_{CB} (kNm/rad)	227.2	263.9	228.2	248.7	175.9	N/A	162.5	N/A

N/A: data not available because of transducer malfunction.

With the knowledge of the column base stiffness k_{CB} derived from the test data, the initial stiffness of the bare-frame specimens is estimated by a simple linear elastic model as shown in Fig. 3-9. It consists of three elastic beams that represents the timber beam and columns and four rotation springs, two of which are for the direct penetration beam-to-column joints, and the other two are for the free-standing column bases. Their respective rotational stiffnesses are k_{J} and k_{BC}. E_{B} is the bending elastic modulus of the timber components; I_{C} and I_{B} are the moments of inertia of the timber column and beam, respectively. For the direct penetration beam-to-column joints, the model proposed by Sakata et al. [3-12] was adopted to estimate the rotational stiffness. The estimated rotational stiffness of the beam-to-column joints is 86.7 kNm/rad, which is much lower than that of the free-standing column base joints.

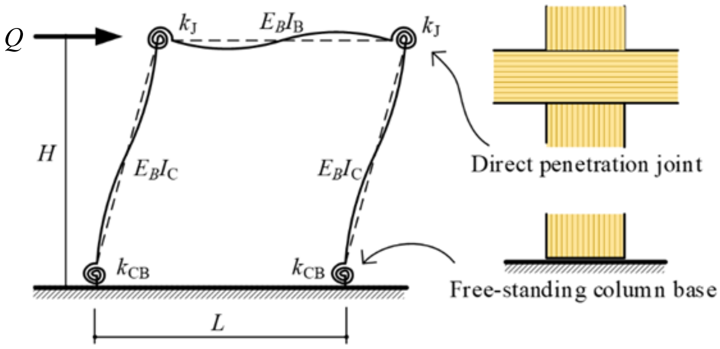

Fig. 3-9. Linear elastic model for calculating initial stiffness of bare frame specimens.

Fig. 3-10 compares the thus-calculated k_1 with the envelope curves and the experimental k_1 of the bare-frame specimens to show that the calculation slightly underestimated the initial stiffness of the specimens. The initial stiffnesses assuming pinned (k_{CB} = 0) or fixed ($k_{CB}\to\infty$) column bases in the model in Fig. 3-9 are also depicted in Fig. 3-10. Either assumption would result in a significance discrepancy in estimating the initial stiffness.

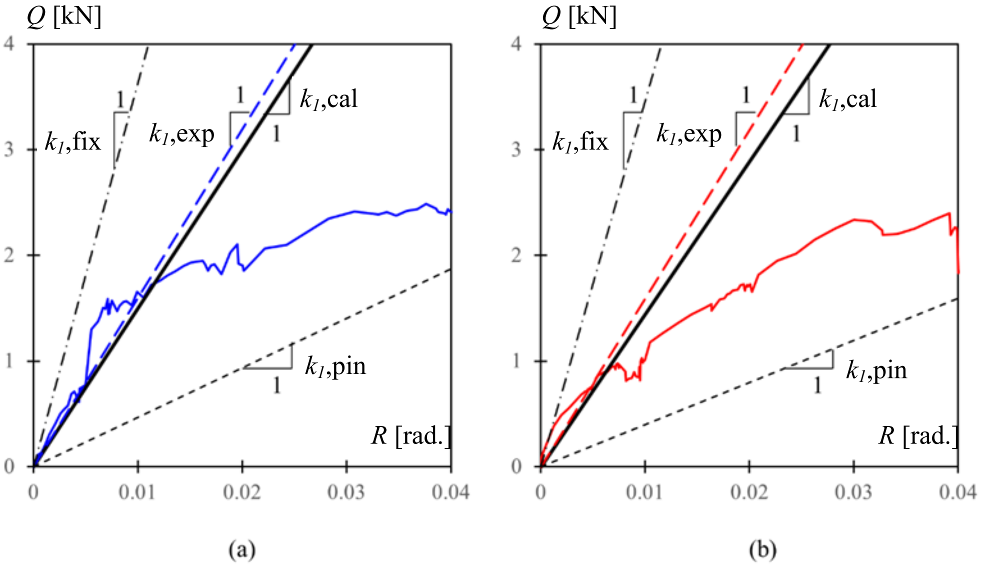

Fig. 3-10. Envelope curves with initial stiffness: (a) S0 and (b) L0.

3.3.2 Thick-infill specimens

The introduction of infills to the timber frame substantially changes the lateral behavior of the structure. The deformation of the short-span specimen with 110-mm-thick infill is predominated by the

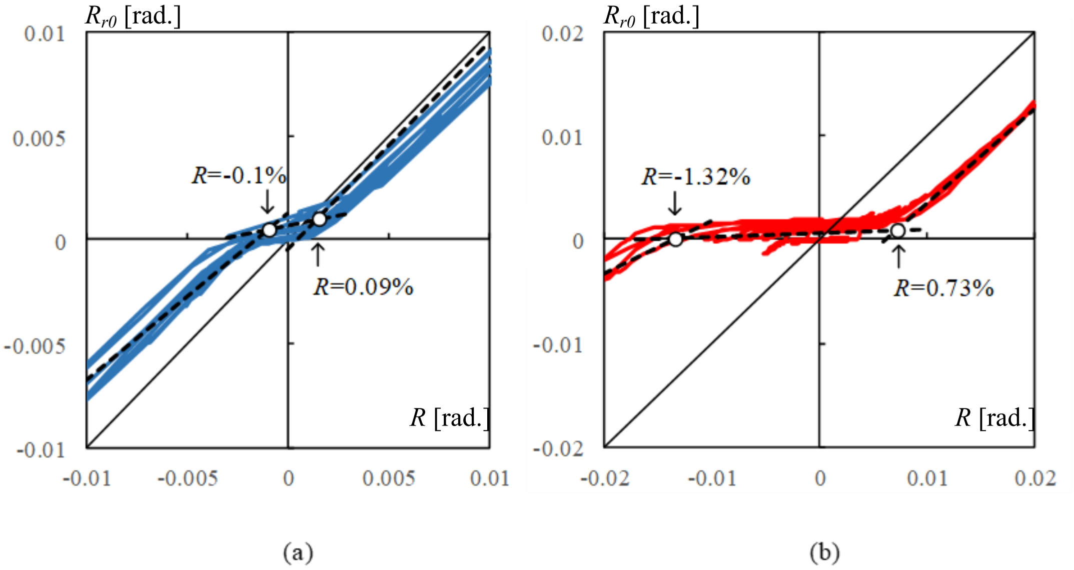

Fig. 3-11. Relationship between rigid-body rotation-to-lateral drift ratio of thick-wall specimens: (a) S110 and (b) L110.

rigid-body rocking around the column base by the fact that the angle of the rigid-body rotation R_{ro} , which is calculated by Eq.3-6, was very close to the overall story drift ratio R [Fig. 3-11(a)]. Piecewise linear idealization of the rigid-body rotation and lateral drift ratio curve indicates that the specimen S110 started to rock at very small lateral drift of 0.1% and -0.09% in the positive and negative direction, respectively. The long-specimen L110 also sustained significant rocking motion in the positive loading direction, but the initiation of rocking was postponed to a lateral drift ratio of 0.73% [Fig. 3-11(b)].

$$R_{ro} = \frac{\Delta_{CW} - \Delta_{CE}}{L} \qquad (3\text{-}6)$$

where Δ_{CE} and Δ_{CW} are the uplift at the east and west column bases, respectively. Δ_{CE} is taken as the average of the displacements by transducers C1 and C2, whereas Δ_{CE} is that by transducers C3 and C4 [Fig. 3-5(b)]. L is the span length of the specimen.

Correspondingly, the hysteretic curve of specimen S110 was approximately bilinear with little residual lateral drift and hysteretic energy dissipation [Fig. 3-12(a)]. No significant shear cracking was observed on the masonry infill throughout the test [Fig. 3-13(a)]. On the other hand, although it also exhibited significant rocking, the hysteretic curve of specimen L110 was fatter than that of specimen S110, indicating additional energy dissipation during the rocking motion [Fig. 3-12(b)]. The primary crack around which the rocking took place extended into the masonry panel as can be seen in [Fig. 3-13 (b)].

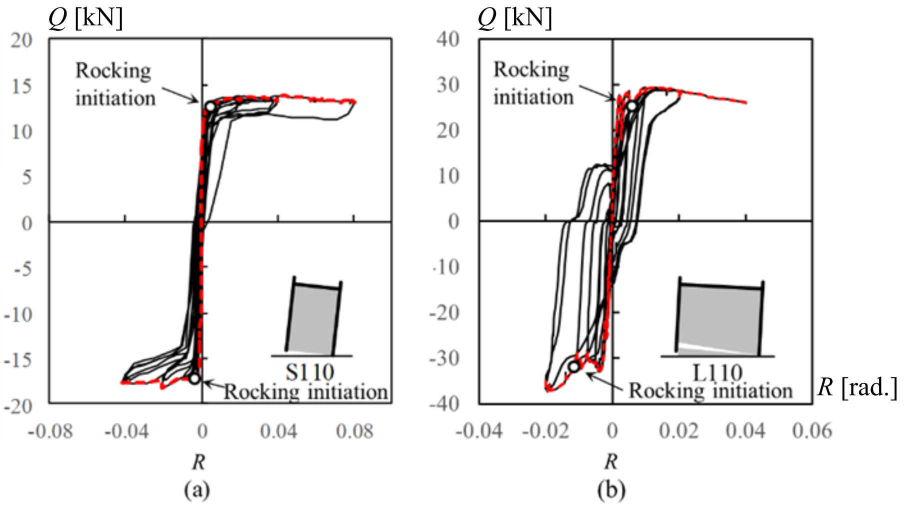

Figure 3-12. Hysteretic curves of thick-infill specimens: (a) S110, (b) L110.

The interaction between the masonry infill and the timber frame was captured by the relative displacements at their interfaces in specimen L110, for which the shear keys at the column bases were not installed in the first cycle loading so that the column bases slid excessively, and the interfacial connections such as the bond of the mortar and embedded nails between the columns and the masonry panel were broken. To observe the deformation of the masonry panel, the shear keys were used for the rest loading of L110 and other infilled specimens. Thus, the test object of this study is internal panel of Chuandou timber frame. The deformed shapes of the timber frames and masonry infill of specimen L110 at *R*=±2.0% are depicted in Fig. 3-14 by bold solid lines and shaded areas, respectively, where the horizontal axis δ is the relative horizontal displacement and the vertical axis is the height of the locations of the displacement transducers.

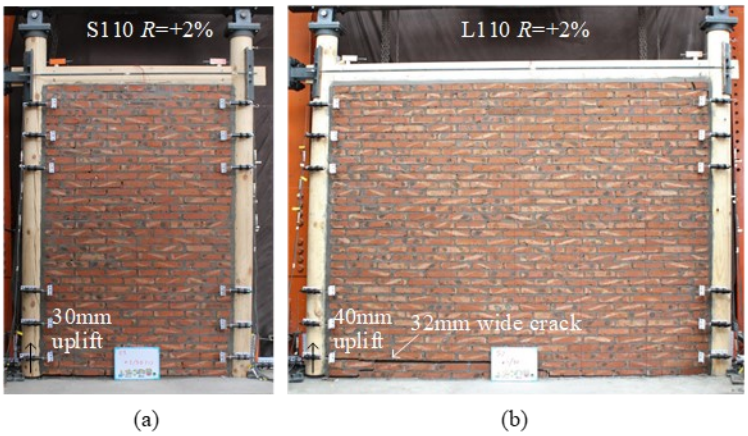

(a) (b)

Fig. 3-13. Rigid-body rotation of thick-infill specimens: (a) S110 and (b) L110.

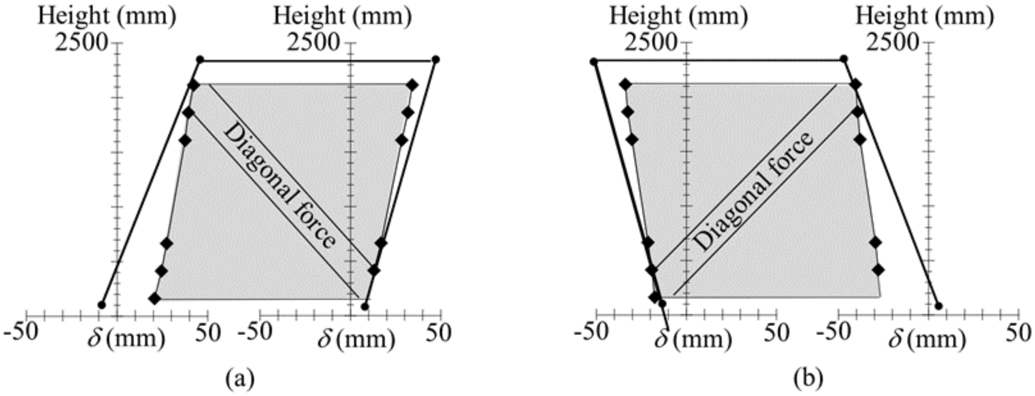

(a) (b)

Fig. 3-14. Deformed shapes of timber frame and masonry infill in specimen L110: (a) *R*=+2%, (b) *R*=-2%.

The deformed shapes of the timber frames are obtained by the lateral displacements at the floor level of each column (transducers D1 and D2 in [Fig. 3-5(b)] and slips measured by transducers S1 and S2 at the column bases. As aforementioned, twelve transducers, denoted as M1-M12 in [Fig. 3-5(b)], were mounted horizontally across the masonry-timber interfaces to monitor the relative displacement between the masonry panel and the timber columns. By further considering thus-obtained relative displacements based on the deformed shapes of the timber frames, it is found that the masonry infill separated from the timber columns at lower left and upper right corners during positive loading and was in contact with the columns at the other two corners [Fig. 3-14(a)], indicating that the masonry infill resisted the lateral load by a diagonal compressive strut which lay approximately between the two corners that were in contact with the columns. The opposite was observed during the negative loading [Fig. 3-14(b)].

3.3.3 Thin-infill specimens

In specimen S50, the 50-mm-thick masonry infill sustained severe shear cracking while the rigid-body rocking was significant. The combined rocking-shear damage pattern corresponds to a fatter hysteretic curve than that of specimen S110 [Fig. 3-15(a)] and a larger deviation of the rocking angle R_{ro} from the story drift *R* [Fig. 3-15(c)]. The first visible diagonal crack on the infill was observed at approximately *R*=0.8%. The maximum diagonal crack width reached 9mm at *R*=1% and the uplift at the column base was 13mm at the same time. The shear cracks and uplift of the column base continued to grow simultaneously with the increase in story drift. The shear cracking became very severe at *R*=4% and the thin masonry panel exhibited visible bulge in the out-of-plane direction. that part of the masonry infill. Part of the infill panel fell to the ground when it was unloaded (Fig. 3-16). The lateral strength of the specimen suddenly dropped after the partial collapse of the infill and became only slightly greater

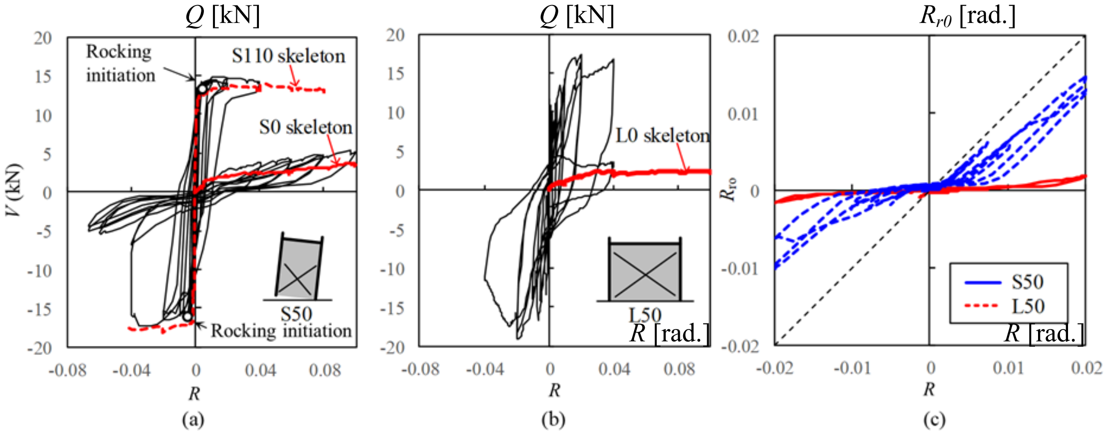

Fig. 3-15. Hysteretic curves of thin-infill specimens: (a) S50, (b) L50 and (c) their rigid-body rotation.

than that of a bare timber frame [Fig. 3-15(a)].

In contrast to S50, specimen L50 exhibited a typical shear failure of the masonry infill [Fig. 3-15 (b)] and the rigid-body rotation of the specimen was negligibly small [Fig. 3-15(c)]. Diagonal cracks were observed on the masonry infill at R=+0.25%. The diagonal crack width reached 28mm at R=2% and the masonry infill partially collapsed at R=-3% (Fig. 3-17), after which the lateral strength of the specimen suddenly dropped to slightly greater than a bare timber frame. Like what was observed in specimen S50, the masonry panel deformed in the out-of-plane because of the in-plane shear before it finally collapsed.

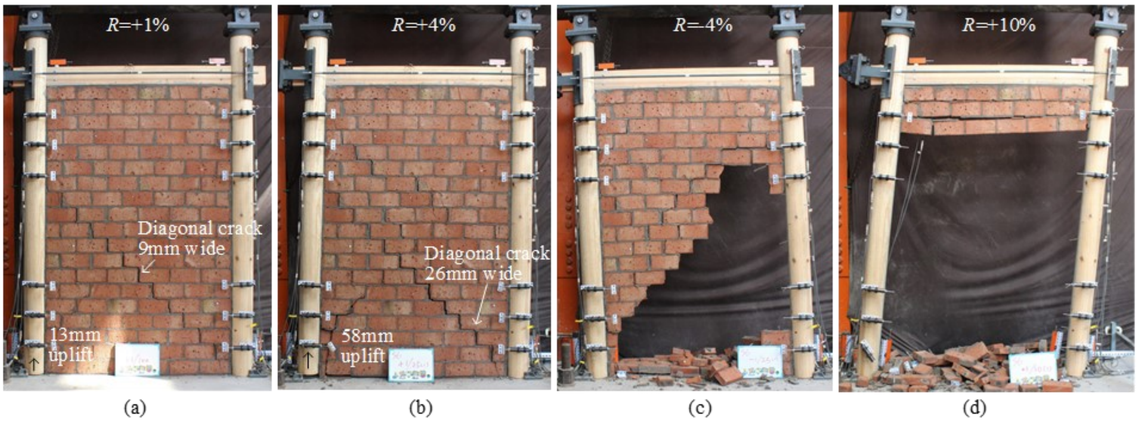

Fig. 3-16. Damage evolution of specimen S50 with a combined rocking-shear failure mode.

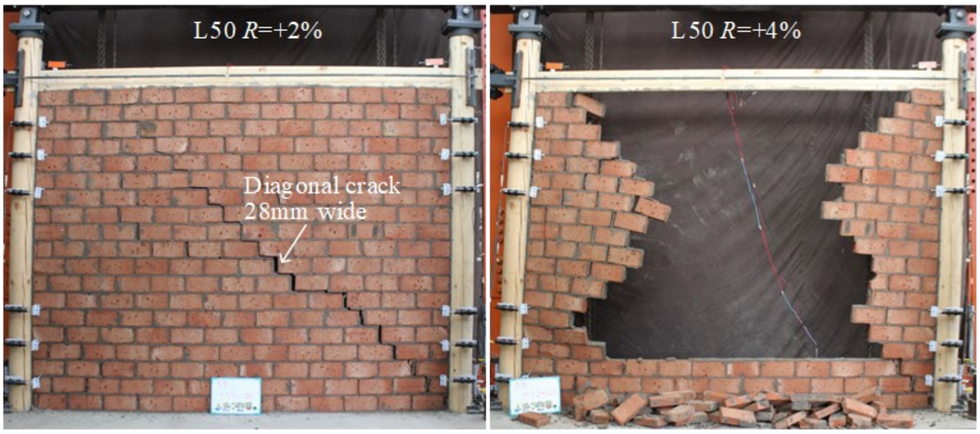

Figure 3-17. Shear cracking and collapse of masonry infill in specimen L50.

Fig. 3-18 compares the slips at the column bases in the three short-span specimens. Column base slips were measured by the displacement transducers S1 and S2 as shown in [Fig. 3-5(b)], respectively. No obvious slip was observed in the bare frame or the thick-infill specimen in which the masonry infill did not exhibit shear cracking, but the thin-infill specimen S50 sustained considerable slip at the column bases and the slips at the two column bases were in opposite directions, indicating that the timber frame opened at its base [Fig. 3-18(c)]. This can be attributed to the expansion of the cracked masonry infill. Significant outward slips at the column bases were also observed in L50, where the masonry infill also sustained diagonal shear cracking.

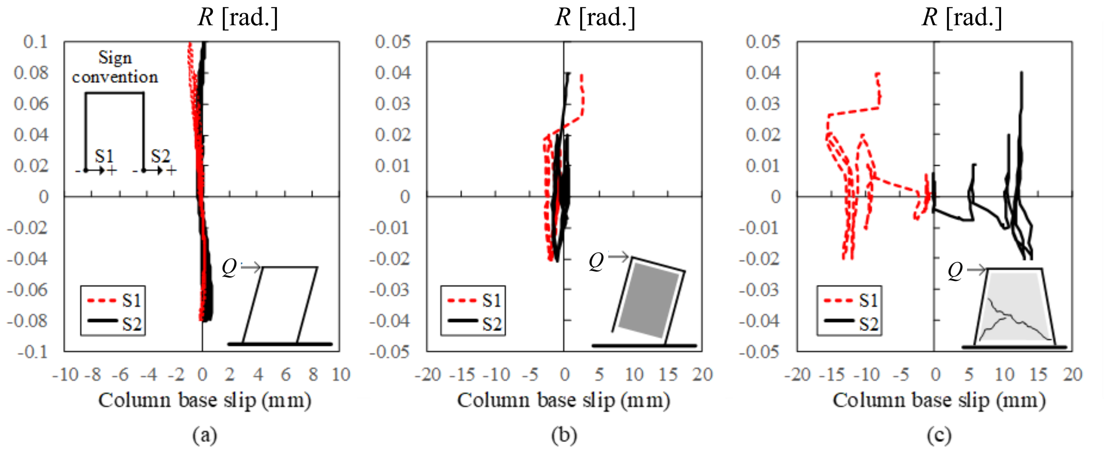

Fig. 3-18. Column base slip of short-span infilled specimens: (a) S0, (b) S110 and (c) S50.

The lateral strengths and stiffnesses of the masonry-infilled specimens are summarized in Table 3-4. The initial stiffness is taken as the slope of the straight line that connects the peak points of the hysteretic curve at story drift ratio R=0.125%. The stiffness of the masonry-infilled specimens were more than 63 to 104 times that of the bare frame specimens even if the masonry infill was a shiner system. The lateral strength of infilled specimens was 3.7 to 10 times that of the bare frame specimens depending on the thickness and damage pattern of infill.

Table 3-4. Stiffness and strength of masonry-infilled specimens

	L50	L110	S50	S110
Initial stiffness, k_1 (kN/rad)	12983.3	16609.6	10169.6	10180.4
Lateral strength, Q_u (kN)	17.3	29.4	14.8	13.8

3.4 Discussions

3.4.1 Estimate of lateral strength

In estimating the shear strength Q_s of unreinforced masonry walls, the equations in FEMA-273[3-13](Eq. 3-7) and the Chinese design code for masonry structures (GB50003-2011) [3-14] (Eq. 3-8) take the same form of multiplying an equivalent mortar strength v_{me} with the net area of the mortar section A_n, but they are different in calculating v_{me}.

$$Q_{s,FEMA} = \tau \times An = 0.5 \times (\tau_0 + \sigma_N) \times A_n \qquad (3\text{-}7)$$

$$Q_{s,GB} = \tau \times A_n = (t_0 + \alpha' \times \mu' \times \sigma_N) \times A_n \qquad (3\text{-}8a)$$

$$\mu' = 0.23 - 0.065 \times \frac{\sigma_N}{\sigma_M} \qquad (3\text{-}8b)$$

where τ_0 and σ_M are the bond-slip and compressive strength of the masonry prism, respectively; $\sigma_N = N/A_n$ is the normal stress in the masonry panel, N is the expected gravity compressive force, equal to the self-weight of the masonry panel in this test; α' and μ' are the coefficients that depend on the loading condition of the structure. When the loading of the structure is predominated by the dead load, $\alpha'=0.64$ and μ' can be obtained by Eq. 3-8(b).

Meanwhile, the lateral force corresponding to the initiation of rigid-body rocking (referred to as the rocking strength hereinafter) can be derived by the moment equilibrium assuming that the specimen rotates around the center of one of the column bases (Eq. 3-9).

$$Q_{ro} = G \cdot L / H \qquad (3\text{-}9)$$

where G is the gravity force on the specimen including its self-weight and the additional gravity load on the top of the specimens and the masonry infill; D is the horizontal distance between the centroid of gravity force to the axis of the column, around whose base the specimen rotates. For long-span specimens, $D = L/2 = 1550$ mm in both positive and negative loading direction, whereas $D = 698$ mm in the positive direction and 932 mm in the negative direction because of the asymmetric arrangement of the steel loading beam in the setup (Fig. 3-5).

The calculated shear strength by Eqs. 3-7, 3-8 and 3-9 for the infilled specimens are shown in Fig. 3-19 along with the hysteretic and envelope curves of the respective specimen. For thick-infill specimens L110 and S110, whose failure was predominated by the rigid-body rotation, the lateral strengths in the test are very close to the estimated rocking strength Q_{ro}. For thin-wall specimens whose masonry infill sustained significant shear cracking, the equation in FEMA 273 (Eq. 3-7) appears to yield a reasonable estimate of the shear strength of the long-span specimen L50, whereas the equation in the Chinese code (Eq. 3-8) well estimates the shear strength of the short-span masonry infill. Since both Eqs. 3-7 and 3-8 are empirical and neither consider the aspect ratio of the masonry wall in the calculation, they appear only applicable to a certain range of aspect ratio. The estimated shear strength $Q_{s,GB}$ and rocking strength Q_{ro} for specimen S50 are quite similar to each other, which is consistent with the observed combined rocking-shear failure mode in S50.

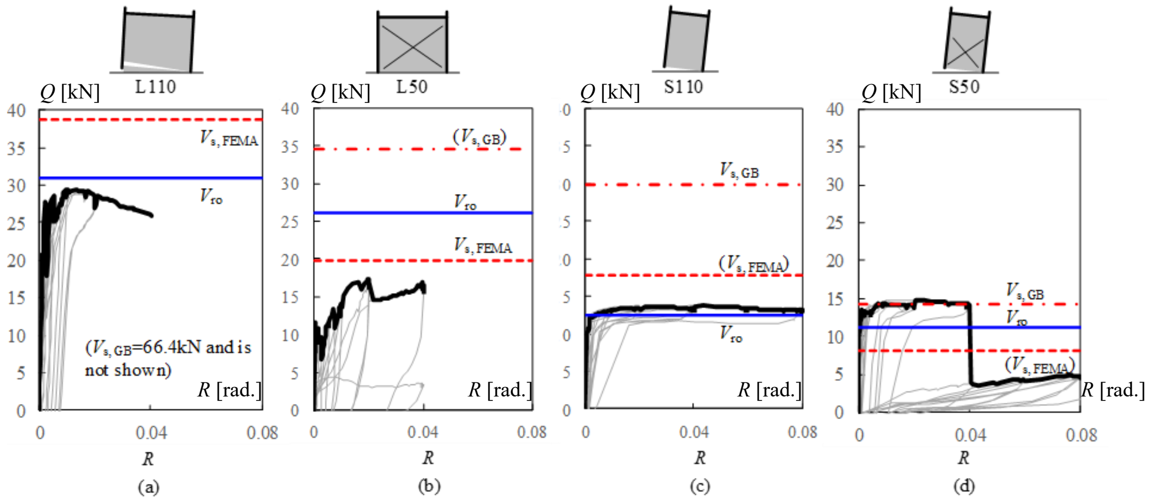

Fig. 3-19. Lateral strength of specimens.

The shear failure of the masonry infill in the test was almost bed-joint sliding failure. When this type of failure occurs, it is commonly observed that the mortar-brick interfaces debond and that sliding shear occurs along the bed joints. Fig. 3-20 shows an example of typical bed-joint sliding failure, which often develops a crack along a horizontal plane or a diagonal stepped crack. The shear stress in mortar joints increases with increasing vertical stress, as experimentally verified by various researchers [3-15] [3-16]. Therefore, the shear strength can be represented using Eq. (3-10).

$$\tau_{MI} = a_t \cdot \tau_0 + \mu_m \cdot \sigma_N \qquad (3\text{-}10)$$

where τ_0 is the initial shear bond strength, and can be obtained following the corresponding material test, which is described in (Section 3.2.2).

μ_m is the coefficient of internal friction of the brick-mortar interface, and

σ_N is the compressive strength of the masonry in the direction perpendicular to the bed joints.

Notably, Eq. (3-10) represents the shear strength of the mortar-brick interfaces. Therefore, it is strictly applicable to cases of shear failure of mortar joints. Numerous researchers have studied the range of values of each parameter in this equation. T. Paulay and M.J. N Priestley [3-17] indicated that values of t_0 range from 0.1 MPa to 1.5 MPa; these researchers also indicated that the value of μ_m varies from 0.3 to 1.2. F. J. Crisafulli [3-18] indicated that the normal stress of the masonry panel σ_N limit for masonry panels ranges between 2 and 4.5 MPa. Beyond this limit, different mechanisms of failure control the strength of the masonry panels, and Eq. (3-10) would overstate the true strength.

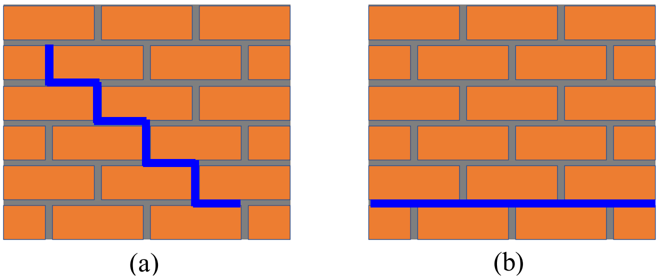

Fig. 3-20 Failure modes of masonry panels subjected to shear force: (a) diagonal stepped crack and, (b) horizontal crack.

In estimating the shear strength Q_{MI} of unreinforced masonry walls, the equations in FEMA-273 [3-13] and the Chinese design code for masonry structures (GB50003-2011) [3-14] (Table 3-5), take the same form of multiplying an equivalent mortar strength τ_0 with the net area of the mortar section A_n (Fig. 3-21), but they are different in calculating τ_{MI}. Both the FEMA and GB considered the strength of masonry panel decreases when the compression of the axis reaches a critical value.

Table 3-5 Recommended values of α_t and μ in codes

Codes	α_t	μ
FEMA 273 [3-13]	0.5	0.5
GB 50003-2011 [3-14]	1	$0.64\times\mu'$

$$\mu' = 0.23 - 0.065\times\frac{\sigma_N}{\sigma_M} \tag{3-8b}$$

where A_n is the net area of the mortar section of the masonry panel.

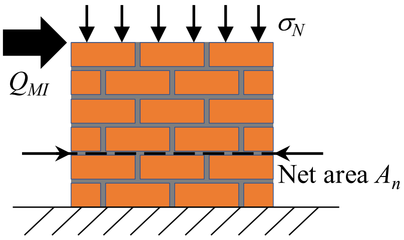

Fig. 3-21. Net area of the masonry panel

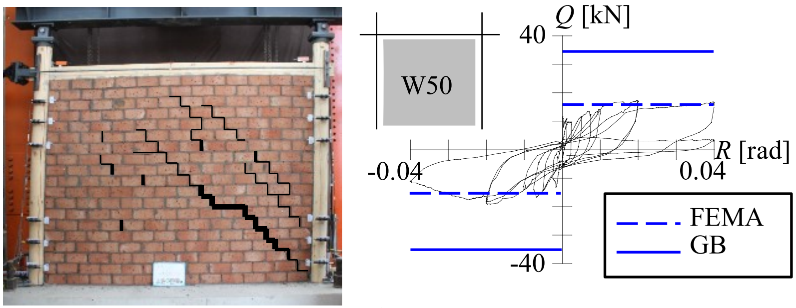

(a) W50

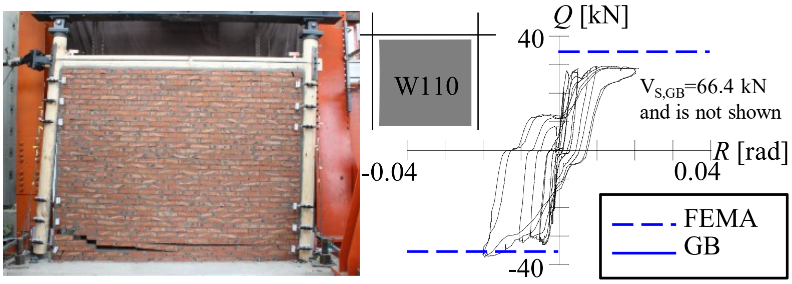

(b) W110

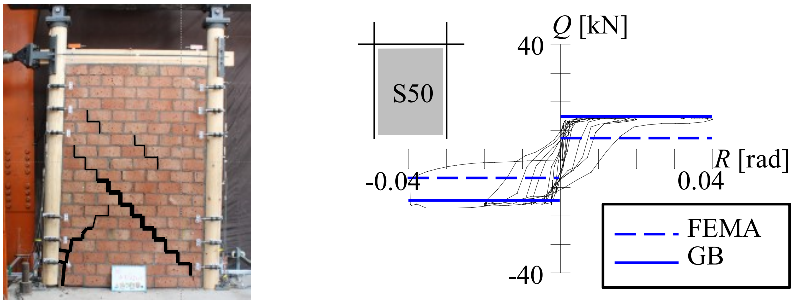

(c) S50

Fig. 3-22. Lateral strength of the specimens.

The shear strength calculated by Eqs. (3-7)-(3-8) for the infilled specimens are shown in Fig. 3-22 along with the hysteretic and envelope curves of the respective specimen. For specimens whose masonry infill sustained significant shear cracking, the equation in FEMA 273, i.e., Eq. (3-7), yields a reasonable estimate for the shear strength of long-span specimens W50 and W110. While the equation in Chinese code, Eq. (3-8), satisfactorily estimates the shear strength of the short-span masonry infill S50. Since both Eqs. (3-7) and (3-8) are empirical and do not consider the aspect ratio of the masonry wall in the calculation, they are only applicable to a certain range of aspect ratios.

Compared to FEMA and GB equations, a more reasonable equation is represented by Paulay and Priestley [3-17]. These investigators suggest that since Eq. (3-10) applies to unreinforced masonry (URM) structures, the higher floor slab acts directly on the brick wall in URM buildings; thus, gravity load σ_N contributes significantly to the shear strength of the URM wall. On the other hand, infill walls are constructed only after the completion of the frame structure, and masonry infills are not designed for gravity loads. Thus, when using Eq. (3-10) to evaluate the shear strength of the infill wall, Eq. (3-10) may overestimate the shear strength of the infill wall. In addition, an equivalent diagonal strut model is assumed (Fig. 3-23), and its compression force Q_d is considered to initiate horizontal shear sliding depending on the shear friction stress τ_0.

The maximum shear force of masonry infill Q_{MI} is thus

$$Q_{MI} = \tau_0 \cdot A_n + \mu_m \cdot Q_d \cdot sin\,\theta$$

where Q_d is the shear force of masonry infill transmitting along diagonal direction.

θ=H/L and is shown in Fig. 3-24.

However, from Fig. 3-24,

$$Q_d = \frac{Q_{MI}}{cos\,\theta}$$

Thus Eq. (3-10) can be rewritten as

$$Q_{MI} = \frac{\tau_0 \cdot A_n}{1-\mu_m \cdot tan\,\theta} \qquad (3\text{-}11)$$

where where τ_0 is the bond strength of masonry infill, which is obtained from the triplet material test described in **Chapter 3.2.2**.

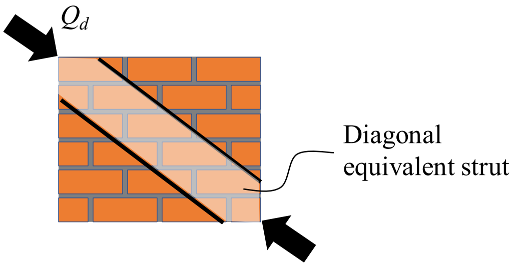

Fig. 3-23. Force transmitting through the masonry infill.

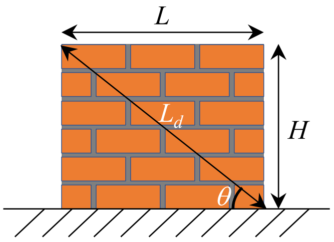

Fig. 3-24. Masonry panel definition.

Notably, Paulay and Priestley recommended a value of μ_m=0.3 in Eq. (3-11) for design purposes, although the experimental results indicate that the coefficient of friction usually varies from 0.7 to 0.85 [3-17].

In this study, to balance the force of masonry infill in the vertical direction, there is a dead load A, a counterforce B of the column, and a vertical force C between the infill and the column (Fig. 3-26), while C is considered in the following two cases. First, although there is clearance between the beam and infill, the clearance is filled with mortar (Fig. 3-25). When a horizontal force is applied to the specimen, the reaction force in the vertical direction is transmitted to the beam through the mortar and then to the column through the beam and is balanced with the gravity load on the column or the tensile force of the column [Fig. 3-26(a)]. Second, the reaction force in the vertical direction is transmitted to the column since it is assumed that there is shear force between the column and the masonry panel [Fig. 3-26(b)] because of the contact between the column and masonry infill (Fig. 3-14). However, there is no experimental evidence to support whether it is Fig. 3-26(a), Fig. 3-26(b), or Fig. 3-26 (a)+(b), and this is only an assumption of the author.

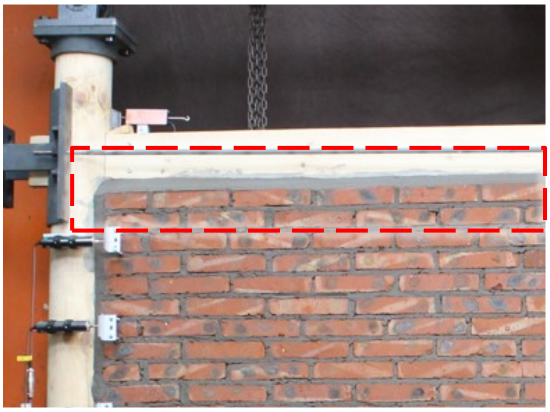

Fig. 3-25. Clearance between the beam and infill panel filled with mortar.

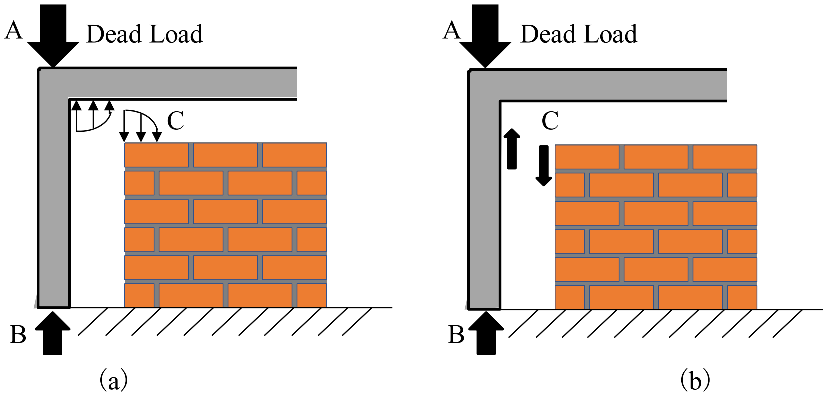

Fig. 3-26. The vertical force $Q_d \times \sin\theta$: (a) through the top mortar joint and (b) through the column.

For τ_0, the test result of the triplet material test is higher than those obtained from wall tests, and this phenomenon is confirmed by experimental work in Riddington et al. [3-19]. These authors conducted a series of tests, including a triplet material test and a five-brick high masonry wall material test, and the test couples were made with mortar with a water-cement ratio of 0.9. The specimens and corresponding results are shown in Fig. 3-27. The vertical axis represents the shear strength τ_0, and the horizontal axis represents the compression stress σ_N perpendicular to the bed-joint direction of the masonry test couples. The figure shows that the wall results are lower than the triplet results. Riddington et al. considered that larger masonry structures, such as walls, have a number of vertical and horizontal mortar joints along which failure may take place. Shear cracks will develop along the mortar joint where shear conditions are worst because masonry is considered a brittle material (Fig. 3-28). In addition, the test results of Riddington et al. [3-19] are listed as follows.

Triplet result*:

$$\tau=\sigma_N+0.53$$

（*：Assumed from Fig. 3-27）

Five-brick wall result:

$$\tau=0.52\sigma_N+0.4$$

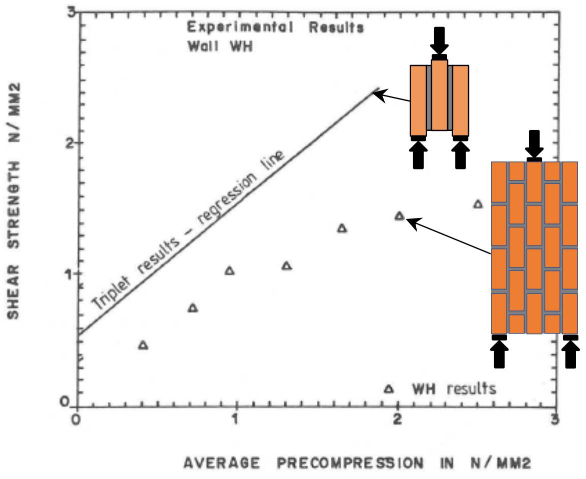

Fig. 3-27. Comparison of the wall and triplet test results. (The figure is modified according to the test results of [3-19])

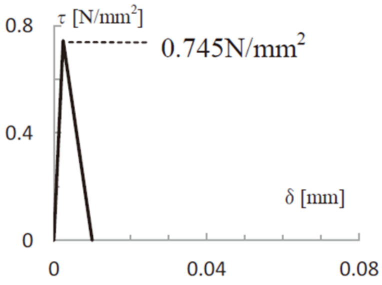

Fig. 3-28. Shear properties of brick-mortar.（Kobayashi et al.'s result[3-20]）

To evaluate the shear strength of masonry infill, a reduction factor b_{MI} of bond strength t_0 is developed by regression analysis. A series of experimental studies of masonry infill walls are selected, and their frame is timber, concrete or steel. The specimens are dominated by mortar shear failure because Eq. (3-11) is strictly valid for debonding at the mortar-brick interface. This study focuses on specimens that use solid clay bricks or solid concrete blocks without openings, and no reinforcement (e.g., longitudinal steel) is adopted in the specimens; thus, the masonry infills for this study are limited to URM (unreinforced masonry) (Fig. 3-29).

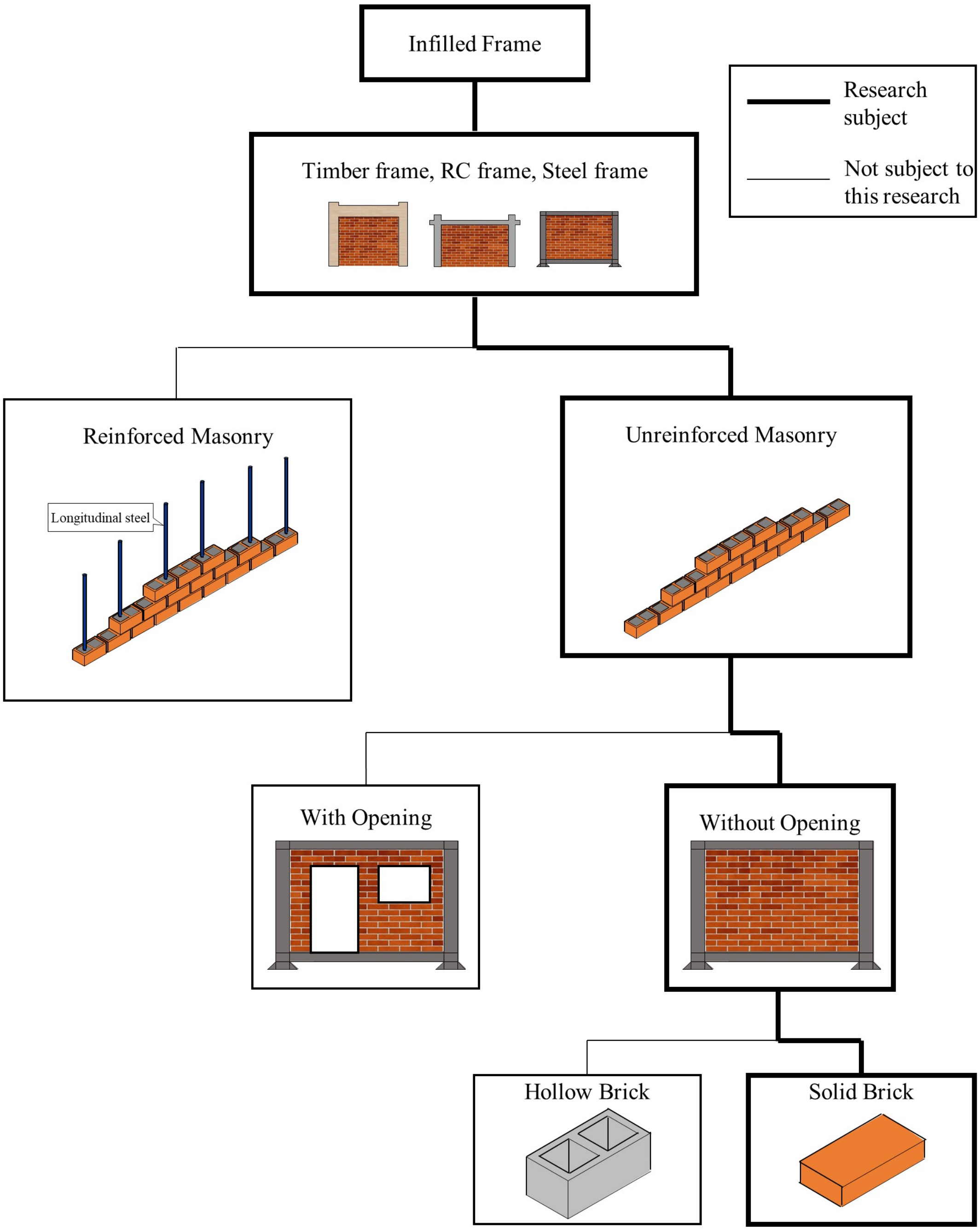

Fig. 3-29 Applied range of this study

According to Paulay and Priestley [3-18], masonry infilled frames can fail in several different ways, including the following:

(a) Rocking: Tension failure of the tension column because of the overturning moments of the masonry infill. [Fig. 3-30(a)]

(b) Debonding of the mortar-brick joint: Sliding shear failures of the masonry along horizontal mortar courses generally occur at or close to the mid-height of the panel. [Fig. 3-30(b)]

(c) Diagonal tensile cracking of the panel: It is not generally regarded as a failure condition; however, higher lateral forces may be supported by the following failure modes. [Fig. 3-30(c)]

(d) Compression failure of the diagonal strut. [Fig. 3-30(d)]

(e) Flexural or shear failure of the columns. [Fig. 3-30(e)]

Notably, failure may be caused by a combination of some of the failure modes described above. For example, the failure of a column may lead to debonding failure of a mortar-brick joint. When designing an infilled frame, it is advisable to assess the strength associated with each of the possible failure modes and use the lowest value as a guide.

The author considers that each failure mode should be investigated separately. Since the building materials for masonry infill are bricks and mortar and their respective material properties are subject to many conditions, it is challenging to define a clear range of equations for each failure mode. In addition, the experiments conducted by the authors mostly represented rocking of the frame and shear failure of masonry infill, and the main objective of this study is masonry infill. The failure mode of shear failure of mortar is discussed in this study. However, in practical applications, other damage modes, such as column failure, should also be evaluated together, and the lowest value should be taken as its design criterion.

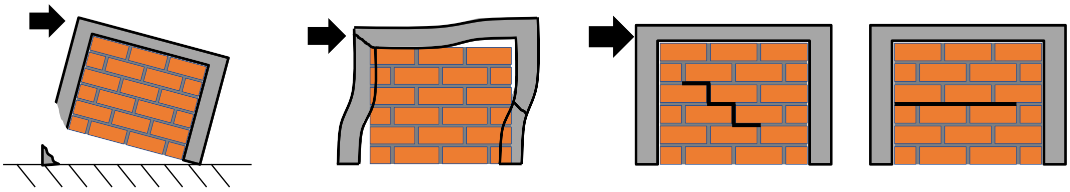

(a) Tensile failure of column (Rocking)

(b) Flexural or shear failure of the columns

(c) Sliding shear failure (Debonding of mortar joint)

(d) Compression failure of the diagonal strut

(e) Diagonal tension crack

Fig. 3-30 Failure mode of the masonry infilled frame.

Through observations of failure from many previous studies, a series of specimens that are considered bed-joint shear failure are represented in Table 3-6 with their details. The specimen configuration at the same scale is shown in Fig. 3-31. In the absence of the value, the following equations are used: the bond strength t_0 and compressive Young's modulus of the brick wall (with mortar) E_M are calculated using Eqs. (3-12) [3-21] and (3-13) [3-22], respectively. Since there are many influencing factors that affect Eq. (3-10) (temperature, humidity, moisture content of bricks, etc. [3-18]), it should be noted that empirical procedures are valid only for materials and conditions similar to those considered when they were obtained. More specifically, the application of this study is listed as follows.

- Eq. (3-11) is strictly valid for debonding of mortar-brick interface.
- The material of the frame is not limited but can include timber, concrete and steel). However, the form of the frame is limited to the structural form that can ensure that the load is transferred along the diagonal direction; thus, diagonal braces are not applied in this study.
- The aspect ratio of the infill wall ranges from 0.67 to 1.56, the wall length limit range is 3100 mm, the wall height limit range is 2350 mm, and brickwork should be limited to a single wythe of the running bond.
- For the material, the mortar shear stress should be within the range of 0.01 to 0.7, and the masonry prism compressive stress should be less than 36.8.
- For specimens with masonry infill or not (i.e., bare frame), the failure modes of their frames are similar.

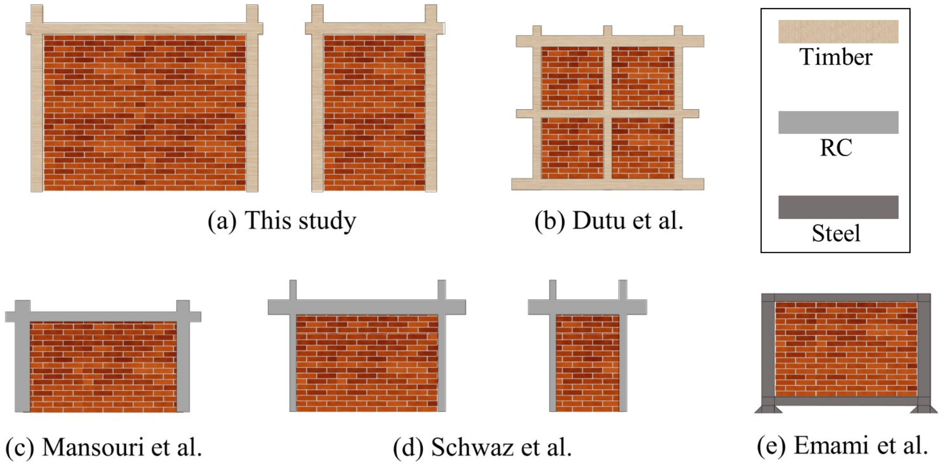

Fig. 3-31. Configuration of each specimen in Table 3-6.

Nolan et al. [3-21] conducted a series of material tests with concrete blocks as specimens and combined their results with some previous tests with concrete blocks and clay blocks. In the mortar, the compressive strength σ_m ranges from 1-15 MPa. The resulting bond strength is from 0.05 MPa to 0.70 MPa. The corresponding empirical equation is listed below.

$$\tau_0 = 0.0471 \times \sigma_m \qquad (3\text{-}12)$$

where σ_m is the compressive stress of the mortar.

Kaushik et al. [3-22] conducted a series of material tests with solid clay bricks and used mortar of cement:lime:sand in ratios of 1:0:6, 1:0.5:4.5 and 1:0:3. Eighty-four masonry prism coupons were used, and one-third of the s_M elasticity moduli ranged from 250s_M to 1100s_M. This resulted in a mean value of 550 and represented Eq. (3-13) as an empirical approach for Young's modulus of the masonry prism E_M. The corresponding empirical equation is listed below. The tests were performed over a range of masonry compressive strengths from 2.2 MPa to 10.5 MPa, so this empirical equation can be applied to the specimens in Tables 3-6 .

$$E_M = 550 \times \sigma_M \qquad (3\text{-}13)$$

where σ_m:Compressive stress of mortar

σ_M:Compressive stress of masonry prism (with mortar)

E_M: Young's modulus of masonry prism (with mortar)

Table 3-6. Comparison of existing masonry infill studies.

Specimen		ID	material	Cross-section (column)	Cross-section (beam)	L	H	t	aspect ratio	An	σ_m	σ_M	τ_0	E_M
				mm	mm	mm	mm	mm	H/L	$L*t$	Mpa	Mpa	Mpa	N/mm^2
This study	Fig.3-31 (a)	L50	timber	Circular section of 170	Rectangular section of 50 wide and 150 deep	3100	2350	50	0.76	155000	6.80	5.90	0.20	3245*
		L110	timber			3100	2350	110	0.76	341000	6.80	5.90	0.20	
		S50	timber			1630	2350	50	1.44	81500	6.80	5.90	0.20	
Dutu et al. [3-15]	Fig.3-31 (b)	S2	Timber	Square section of 120	Square section of 120 or 160	1800	1800	100	1.00	180000	8.35	36.80	0.70	1900
Mansouri et al. [3-23]	Fig.3-31 (c)	S	Concrete	Square section of 200	Rectangular section of 200 wide and 150 deep	2100	1300	106	0.62	222600	8.33	2.30	0.31	437
Schwaz et al. [3-24]	Fig.3-31 (d)	1000	concrete	Rectangular section of 100 wide and 200 deep	Rectangular section of 100 wide and 200 deep	900	1400	100	1.56	90000	8.30	2.70	0.39*	1485*
		0000				2045	1400	100	0.68	204500				
Emami et al. [3-25]	Fig.3-31 (e)	M-RC-1B	steel	IPBL180	IPBL120	2079	1386	150	0.67	311850	8.3	9.5	0.39*	1800

*: Calculated by Eq. (3-12) or (3-13).

An approximate approach is used to obtain the contribution of the infill panel (Fig. 3-32). Using specimen W110 as an example, the envelope curve of its infilled specimen and the corresponding bare frame specimen are illustrated in Fig. 3-33. The contribution of the infill wall is obtained by subtracting the envelope curve of the bare frame specimen from that of the infilled specimen using linear interpolation. In addition, to obtain a safer infill extraction value, the forces after the maximum force of the bare frame are all set to their maximum value.

Many scholars have considered that the contribution of masonry infill is the difference between the lateral forces of masonry infilled frame specimens and the corresponding bare frame specimens at the same story drift ratio [3-26][3-27][3-28][3-29][3-30]. According to this approach, the failure in the flexure of a column and the yield failure of an infill wall are reached at similar drift ratios [3-28][3-29], or the infill panel reaches a limit that is lower than the drift limitation of the bare frame (i.e., the frame behavior is not affected significantly by the test conducted on the infilled frame specimen) [3-30]. It should be noted that this approach is only an approximation because the state of strain of the frame is different between the bare frame specimen and the infilled frame specimen. For clarity, extracted masonry infill will be referred to as extracted infill in the following, while frame specimens with masonry infill walls will be referred to as infilled frames.

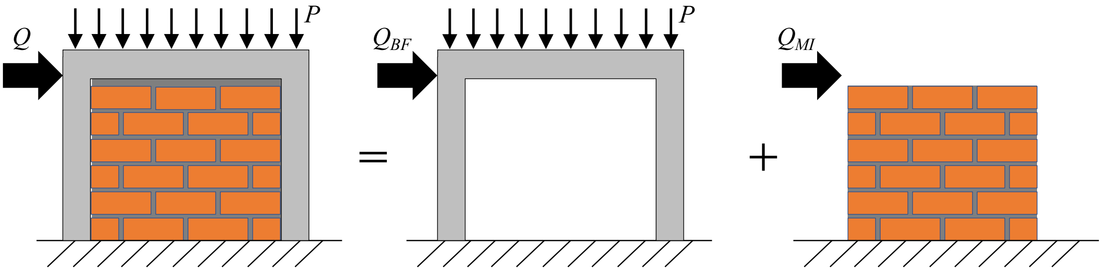

Fig. 3-32. Subtraction of the bare frame from the infilled frame.

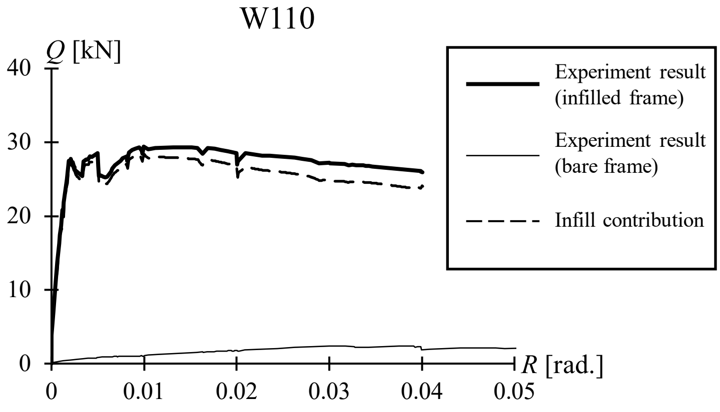

Fig. 3-33. Subtraction of the bare frame from the infilled frame.

Typically, masonry infill walls are not subject to seismic structural design since they are non-structural components. This experiment was conducted by obtaining the contribution of masonry infill walls at mortar bond failure, which is considered to give a reference value for the range of horizontal resistance and safe drift ratio values for masonry infill.

Fig. 3-34 illustrates the definition of the envelope curve of the masonry infill panel, [Fig. 3-34(a)] represents the extracted infill, and [Fig. 3-34(b)] represents the infilled frame. The characteristic points of the envelope curve, namely, the yield strength Q_y and ultimate strength Q_u, are defined to generate the performance level of extracted masonry infill. For the first part of the envelope curve, the yield strength Q_y is considered to be the point where the stiffness decreased to 30% of the initial stiffness k_1. The stiffness continuously deteriorates after the yield strength until the maximum strength Q_{max} is reached, and the line between Q_y and Q_u is determined as the secondary contact stiffness k_2. The same approach is used to obtain the yield strength and maximum strength of the masonry infilled frame specimens. With the example of specimen W110, the characteristic points of the extracted infill are represented by hollow diamonds, while the characteristic points of the infilled frame specimen are represented by solid diamonds.

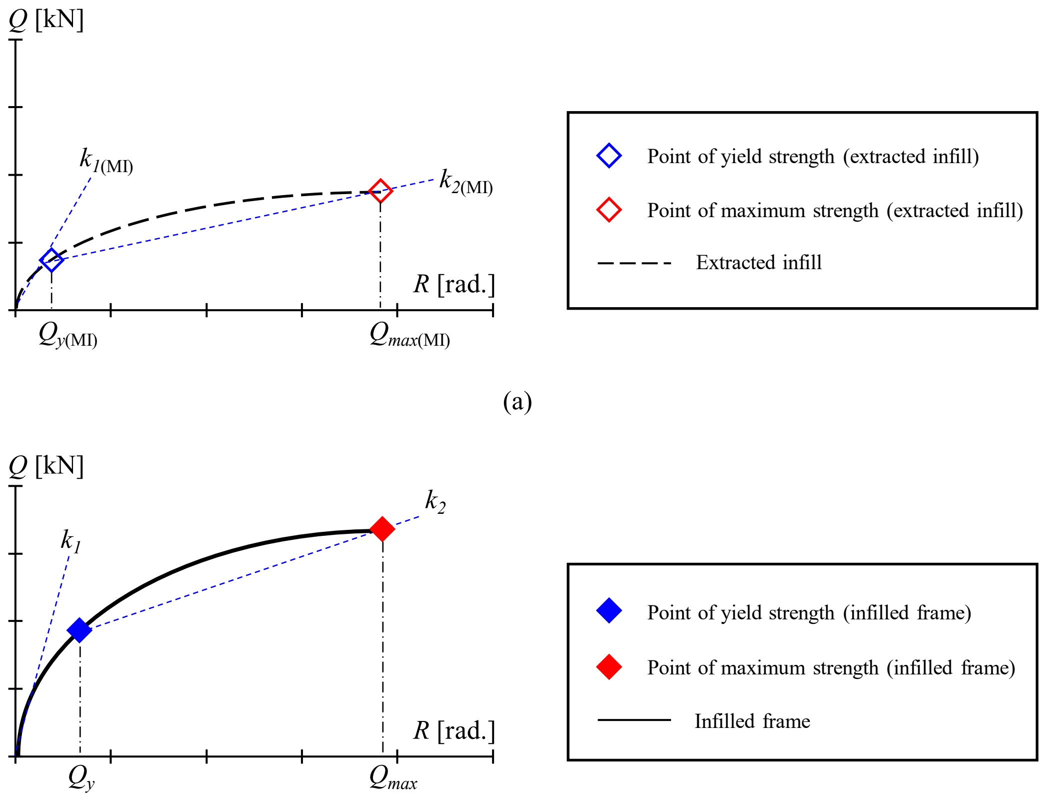

(a)

(b)

Fig. 3-34. Definition of envelope curve: (a) extracted infill and, (b) infilled frame.

The results for each specimen in Table 3-6 are represented in Fig. 3-35 by the envelope curves defined above. For most specimens, the characteristic point of the extracted infill is located at the same drift ratio as the characteristic point of the infilled frame; however, for a few specimens, the characteristic point of the extracted infill is located to the left of the infilled frame's point. This is regarded as a safe method of evaluating the envelope curve of the infill itself.

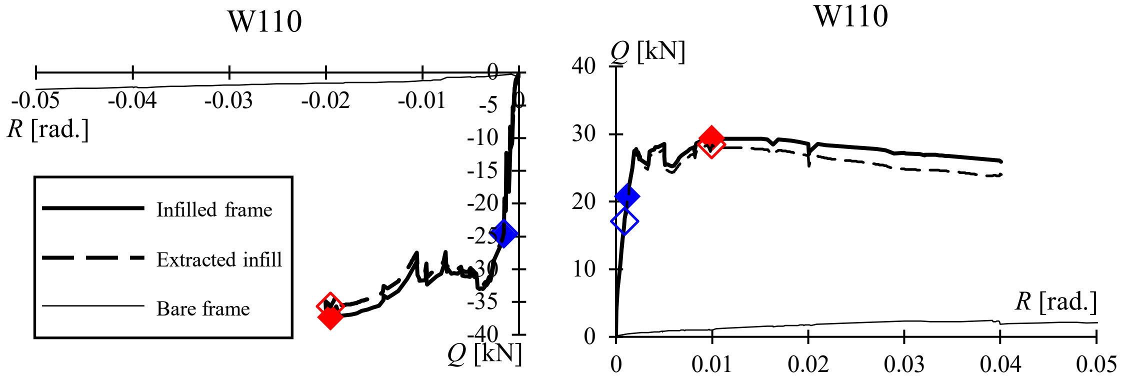

Test result of specimen W110 of this study

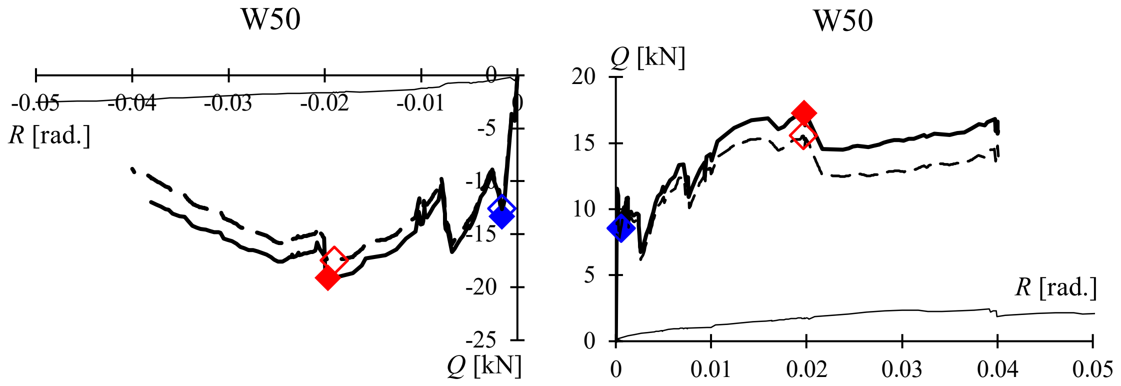

Test result of specimen W50 of this study

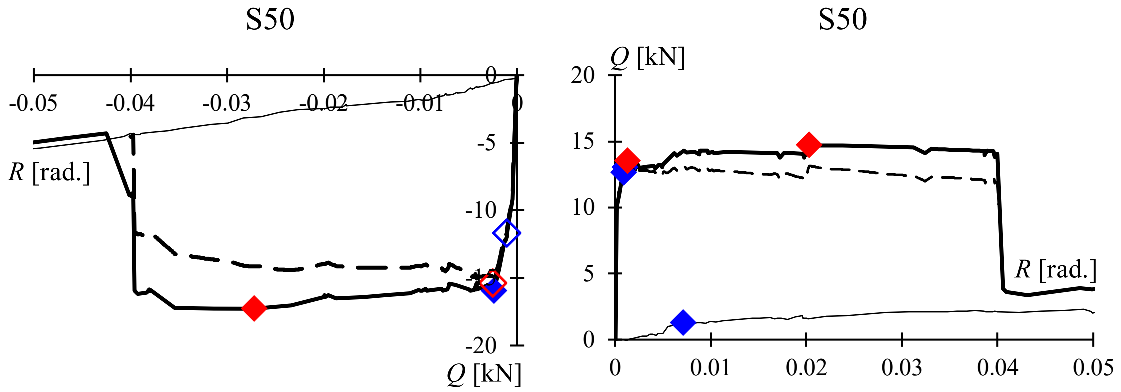

Test result of specimen S50 of this study

Figure continue on the next page

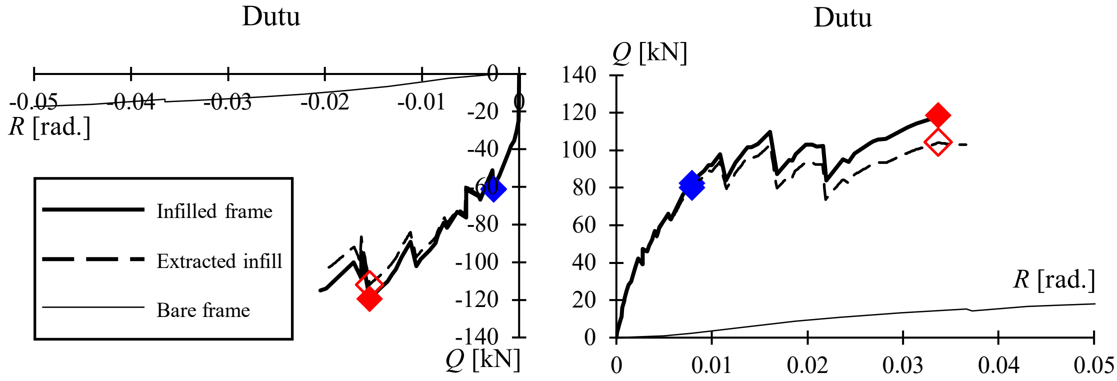

Dutu et al. ’s results [3-15]

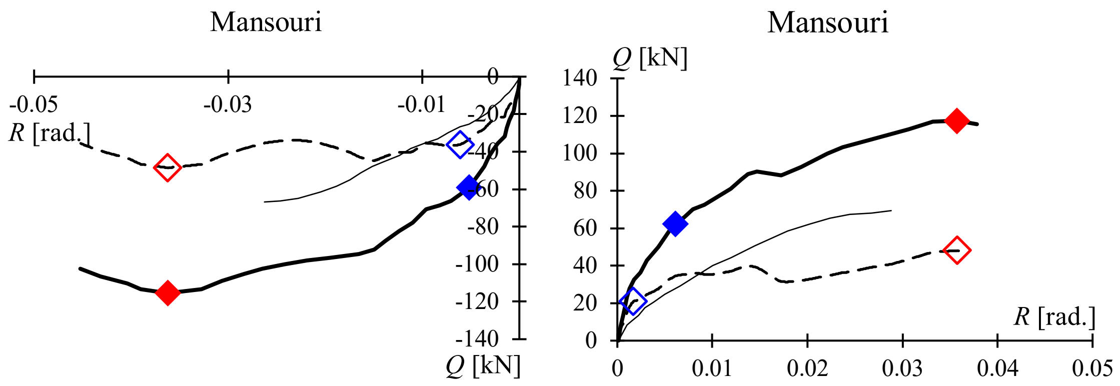

Mansouri et al. ’s results [3-23]

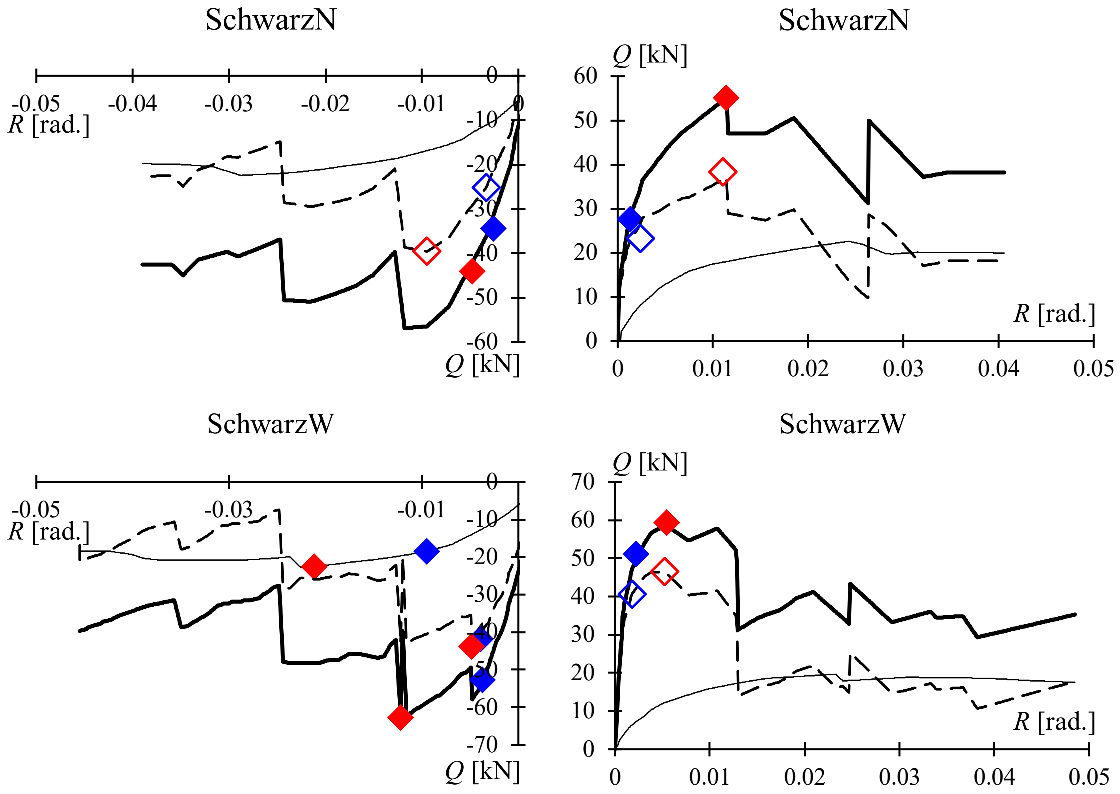

Schwarz et al.’s results [3-24]

Figure continue on the next page

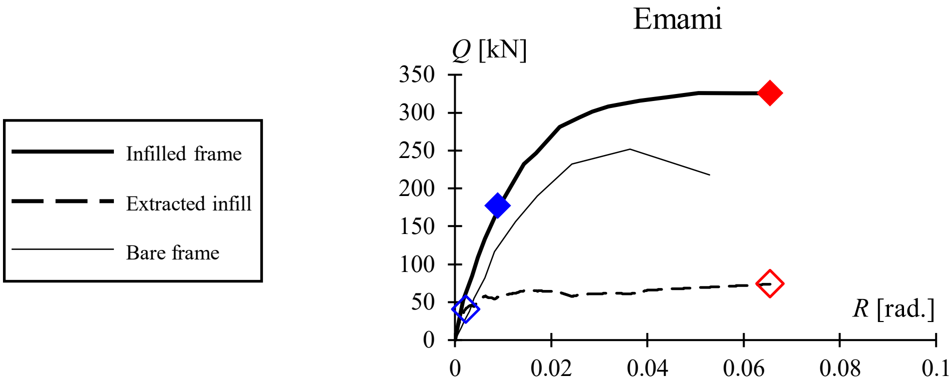

Emami et al.'s results [3-25]

Fig. 3-35 Envelope curve of the specimen in Table 3-6.

A definition of specific performance levels suitable for the in-plane response of extracted infill is proposed within the scope of this study. The limit state definition relies on the performance of the infill panel obtained from the results of this experimental study. A description of each characteristic point and its corresponding stiffness is provided below. The specific values of the terms of each equation are taken with reference to Table 3-6.

First, the calculation results of Eq. (3-11) are compared with the experimental results (Fig. 3-36). The vertical axis represents the experimental results, and the horizontal axis represents the calculated results. It can be found from the figure that the calculation results are higher than the experimental results.

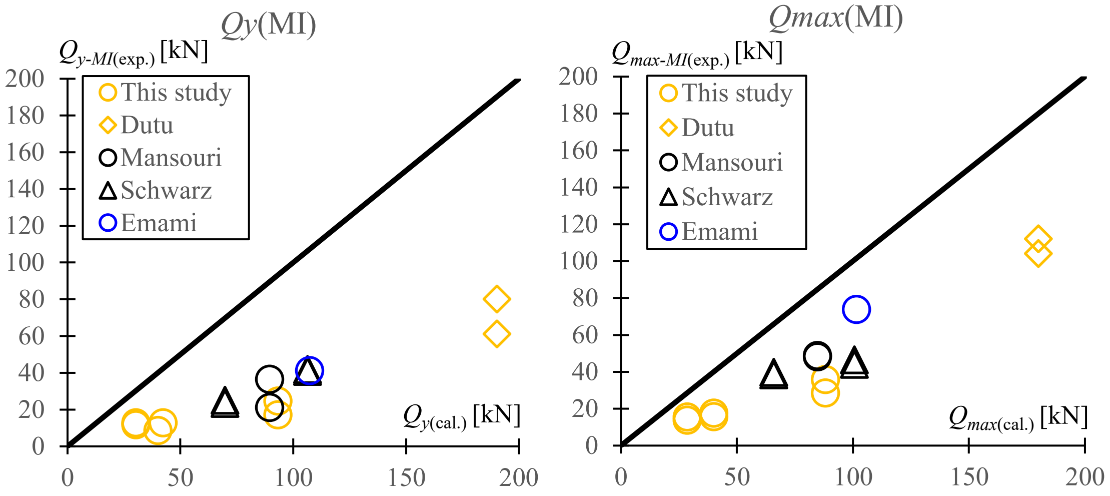

Fig. 3-36. Experimental results versus calculated results of Eq. (3-11).

Then, an empirical factor b_{MI} to reduce the bond strength t_0 is developed according to the approximation of Fig. 3-36. For the yield strength Q_y, $\beta_{MI\text{-}y}$ is 0.35, while for the maximum strength, $\beta_{MI\text{-}max}$ is 0.54. The comparison of the calculated results with applied empirical factors and the experimental results is shown in Fig. 3-37.

Notably, Eq. (3-11) is valid only for estimating the maximum strength of a specimen. However, by comparing the two empirical coefficients, the bond strength at the yield point in this study was approximated to be 65% of the maximum strength (i.e.: for yield strength, $\tau_{0\text{-}yield}=(\beta_{MI\text{-}y}/\beta_{MI\text{-}max})\times\tau_0=0.65\times\tau_0$). Thus, the maximum strength and the yield strength of masonry infill can be obtained by Eq. (3-14) and Eq. (3-15), respectively.

$$Q_{MI-max}=\frac{(\tau_0\times\beta_{MI})\cdot A_n}{1-\mu\cdot tan\,\theta} \qquad (3\text{-}14)$$

$$Q_{MI-y}=0.65Q_{MI-max} \qquad (3\text{-}15)$$

where β_{MI} is the reduction coefficient, which is equal to 0.54 for the maximum strength.

A comparison of the experimental results and the calculated results using Eq. (3-14) and (3-15) is represented in Fig. 3-37. The calculation results almost match the experimental results; thus, the calculation result is used in the following discussion.

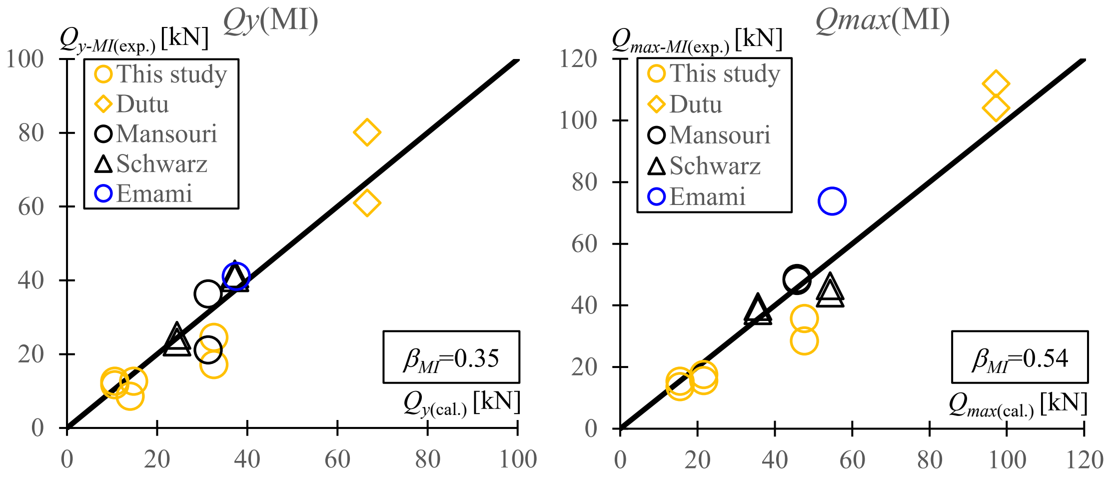

Fig. 3-37. Experimental results versus calculated results of Eqs. (3-14)-(3-15).

Regarding the balance of the force ABC shown in Fig. 3-36, the comparison of the vertical component of the diagonal force Q_d calculated by Eq. (3-11), with the dead load applied to the specimen, is shown in Fig. 3-38. [Fig. 3-38 (a)] For the specimen with a freely standing column, the column is compressed, and it is known from the calculation that the dead load applied to the specimen is greater than the calculated value, so there is no rigid body rotation for the specimens with the crack on the mortar joint. In [Fig. 3-38 (b)], for specimens with columns fixed to the foundation, the columns of specimens of Dutu et al. [3-15] and Emami et al. [3-25] are subjected to tensile forces, and the evaluation in Fig. 3-37 reveals that the calculated values do not differ much from the experimental values.

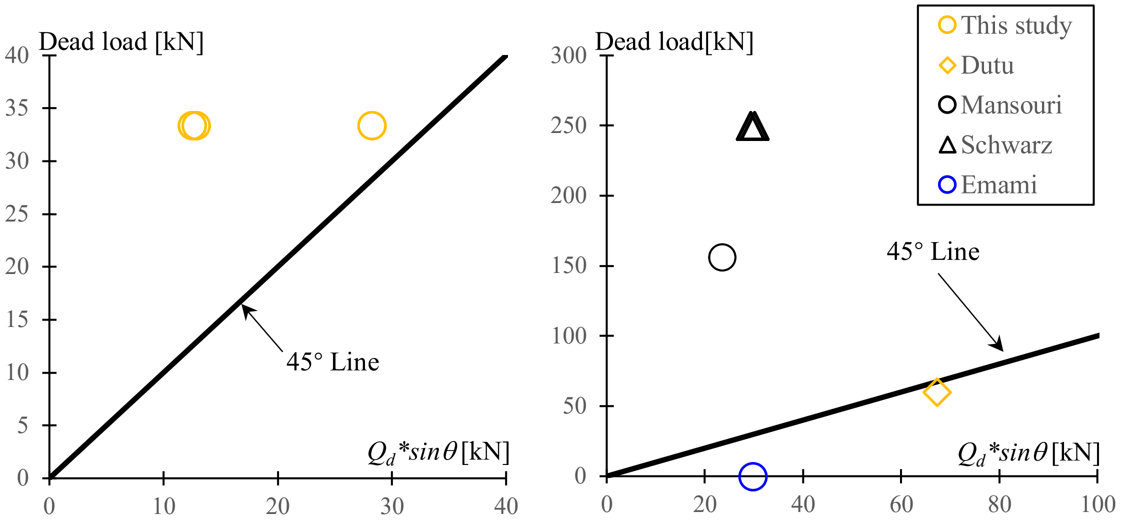

(a) Column base free

(b) Column base fixed

Fig. 3-38. Verification of the force in the vertical direction.

3.4.2 Estimate of the stiffness

According to Eq. (3-11), the horizontal force acting on the net area of the infill is provided by the horizontal component of the diagonal compressive force Q_d (see Fig. 3-23), the diagonal force is considered to be an equivalent strut in the masonry infilled frame, and the deformation of the strut is considered in Fig. 3-39.

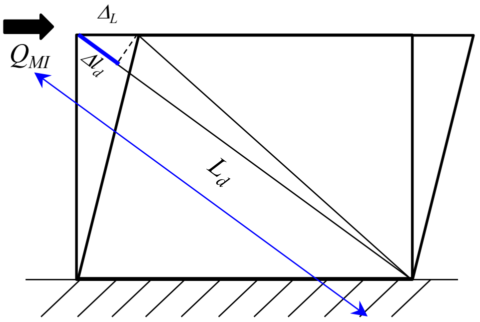

Fig. 3-39. The deformation of diagonal equivalent strut.

The stiffness can be calculated by the following equations.

Axis force of the strut $$Q_d = \frac{Q_{MI}}{\cos\theta}$$

Deformation of the strut $$\Delta L_d = \frac{Q_d \cdot L_d}{E_M \cdot A_d}$$

Effective area of the strut $$A_d = w \cdot t$$

Horizontal deformation of the infill $$\Delta_L = \frac{\Delta L_d}{\cos\theta}$$

Stiffness of the infill $$k_I = \frac{Q_{MI}}{d} = \frac{E_M A_d}{L_d}\cos^2\theta \tag{3-16}$$

where t is the thickness of masonry infill.

w is the effective width of the diagonal strut (see Fig. 3-40).

E_M is the elasticity modulus of masonry prism.

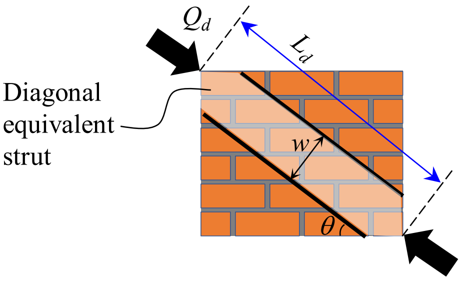

Fig. 3-40. Effective width of the diagonal strut.

There are many equations that are used to calculate the width of the equivalent diagonal strut *w*. Most of these equations are empirical equations from experimental studies that are employed to obtain the relationship between the width w and the length of the infill in the diagonal direction. The equations are presented in the following review.

According to Stafford smith [3-31], a dimensionless parameter λ_H, expressing the relative stiffness of the infill panel to the frame, is listed as follows.

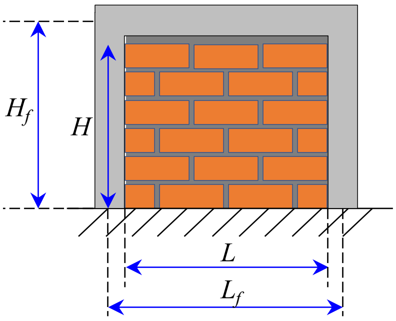

Fig. 3-41. Definition of the geometric parameter.

$$\lambda_H = H_f \sqrt[4]{\frac{E_M \cdot t \cdot \sin 2\theta}{4E_{FC} I_C H}} \qquad (3\text{-}17)$$

where H is the height of the infill wall .(see Fig. 3-41)

E_{FC} is the elasticity modulus of the frame.

I_C is the moment of inertia of the columns.

This equation is developed based on the 'characteristic λ' used in beams on elastic foundation theory [Eq. (3-18)]. The term sin2θ in the parameters of Eq. (3-17) is obtained considering the full length of diagonal strut *w** in Fig. 3-42. The relative stiffness *p* between the frame and infill using term sin2θ is shown in [Eq. (3-19)].

Eq. (3-17) may be simplified assuming that H_f=H and sin2θ=1 by Riddington et al.[3-32]. Thus Eq. (3-20).

$$\lambda_H = H_f \sqrt[4]{\frac{p}{4E_{FC} I_C}} \qquad (3\text{-}18)$$

$$p = E_M \cdot t \cdot \sin 2\theta / H \qquad (3\text{-}19)$$

$$\lambda_H = \sqrt[4]{\frac{E_M \cdot t \cdot H^3}{4E_{FC} I_C}} \qquad (3\text{-}20)$$

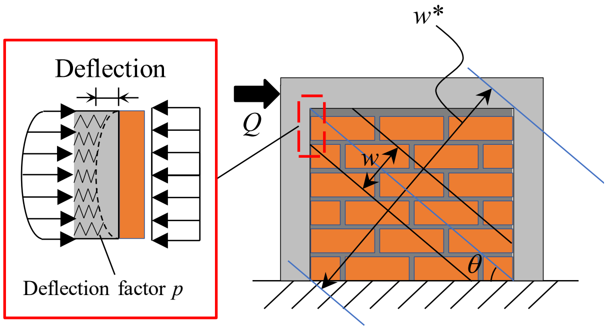

Fig. 3-42 Deflection of frame based on elastic foundation theory.

The typical values for λ_H range from 3 to 10 according to Crisafulli F. [3-18]. The smaller values reveal that the frame is much stiffer than the infill panel, and the higher value indicates that the frame is much more flexible than the infill panel. Initially, the parameter λ_H was proposed for steel frames, but it has also been used for concrete frames.

Mainstone[3-33] carried out a series of experiments on masonry panels surrounded by steel frames. The size of the infill wall ranged from 406 mm to 3100 mm, most of them were on a small scale, and the specimen was surrounded by a steel frame, diagonally loaded in compression. The following empirical expression was obtained from these tests.

$$w = 0.175(\lambda_H)^{-0.4} \cdot L_d \qquad (3\text{-}21)$$

In an analysis of previous experimental data obtained from steel frames infilled with mortar with height/span length ratios varying from 0.67 to 1.0, Liauw and Kwan [3-34] considered that the effective width of masonry infill is related to half of the height and half of the span length of the infill (see Fig. 3-43). These authors provided the following approximate equation with λ_H from Stafford Smith :

$$\frac{w}{H \cdot cos\,\theta} = \frac{0.95}{\sqrt{\lambda_H}} \qquad (3\text{-}22)$$

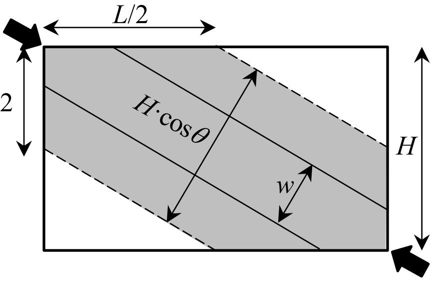

Fig. 3-43. The effective width of masonry infill (figure modified according to Liauw and Kwan[3-34])

In addition to using the factor λ_H, the other approach is to assume the effective width of the strut based on the length of the infill's diagonal length L_d. Paulay and Priestley [3-17] noted that a potentially high value of w will result in a stiffer structure as well as a higher seismic response. These researchers suggested the following conservative value for design proposals:

$$w = 0.25 \cdot L_d \qquad (3\text{-}23)$$

A lateral force of 50% of the ultimate capacity is recommended using this equation.

The relevant parameters of each frame and the λ_H derived by Eq. (3-20) are noted in Table 3-7. It is worth noting that the modulus of elasticity of two concrete frames is not documented in their paper, so Eq. (3-24)[3-35] is used to estimate it. Eq. (3-24) can be used for specimens under concrete compression at 36 MPa.

Table 3-7. Material properties of the surrounding frame.

Study	Frame	σ_C	E_C	I_C	λ_H
		MPa	N/mm^2	cm^4	Thin wall / Thick wall
This study	Timber	25.92	3870	4098	7.6 / 9.2
Dutu et al. [3-15]	Timber	5.1	11920	1728	6.1
Mansouri et al. [3-23]	RC	21.9	23423*	13300	1.7
Schwarz et al. [3-24]	RC	28.8	26861*	1667	3.9
Emami et al. [3-25]	Steel	-	185000	2510	2.5

*： Calculated by Eq. (3-24)

$$E_C = 21000 \times \left(\frac{\gamma}{23}\right)^{1.5} \times \sqrt{\frac{\sigma_C}{20}} \qquad (3\text{-}24)$$

where σ_C is the compression strength of the column of the surrounding frame.

γ is the weight of concrete per volume, equal to 24 for concrete σ_C under 36 MPa.

The stiffness of the extracted infill is calculated and compared to experimentally approximate values using Eqs. (3-21) to (3-23), and the following findings are obtained (Fig. 3-44). By comparison, Mainstone's equation provides an accurate estimate of the approximate initial stiffness, while the other two equations provide values considerably higher than the experimental value. However, the λ_H value of some of the specimens exceeded the range of the empirical equations (λ_H=2~6) originally obtained.

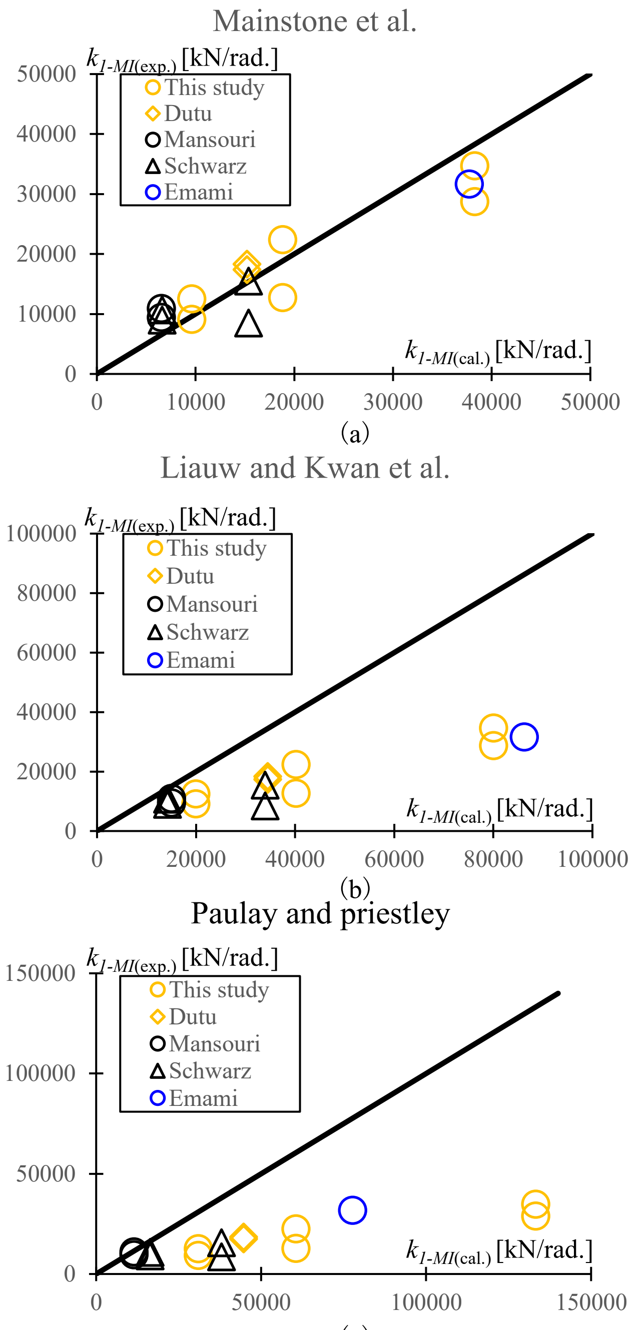

Fig. 3-44 Comparison between experimental value and calculated value of approximate initial stiffness: (a) Mainstone's equation[3-33], (b) Liauw and Kwan's equation[3-34], (c) Paulay and Priestley's equation[3-17].

The line between yield strength Q_y and the maximum strength Q_u is determined as the secondary contact stiffness *k2*. The secondary contact stiffness is determined by the maximum ratio of the calculated initial stiffness to the experimental value of the secondary stiffness (Fig. 3-45) (i.e.,: k_2=0.28k_1). A stiffer secondary stiffness results in a lower drift ratio of the maximum strength.

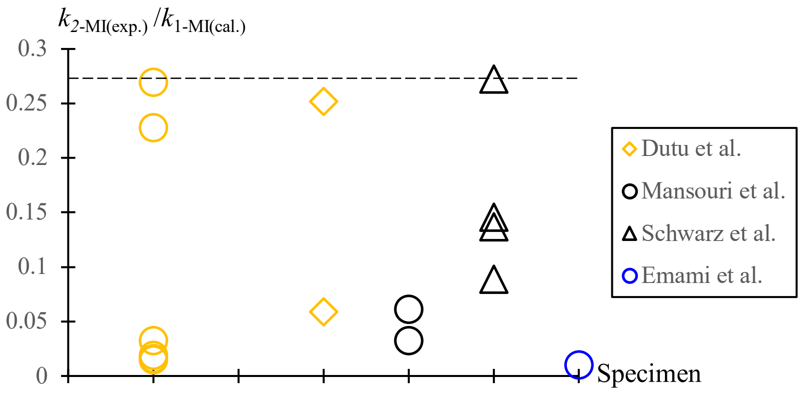

Fig. 3-45. Evaluation of secondary stiffness.

As a result, the equation of initial stiffness and secondary stiffness of masonry infill can be listed as follows.

$$k_{1-MI} = 0.175E_M \cdot (\lambda_H)^{-0.4} \cdot t \cdot cos^2\,\theta \qquad (3\text{-}25)$$

$$k_{2-MI} = 0.28k_{1-MI} \qquad (3\text{-}26)$$

3.4.3 Estimate of the story drift ratio

An extracted infill wall is considered elastic until the specimen reaches its yield strength; thus, its drift ratio at yield strength and maximum strength are considered to be derived using Eq. (3-27) and (3-28), respectively.

$$R_{MI-y} = \frac{Q_{MI-y}}{k_{1-MI}} \tag{3-27}$$

$$R_{MI-max} = R_{MI-y} + \frac{Q_{MI-max}}{k_{2-MI}} \tag{3-28}$$

where $Q_{MI\text{-}y}$ is the yield strength of the extracted infill, obtained from Eq. (3-15)

$k_{1\text{-}MI}$ is the initial stiffness of the extracted infill, obtained from Eq. (3-25)

$Q_{MI\text{-}max}$ is the maximum strength of the extracted infill, obtained from Eq. (3-14)

$k_{2\text{-}MI}$ is the secondary stiffness of the extracted infill, obtained from Eq. (3-26)

The experimental and calculated drift ratios at yield strength and maximum strength are illustrated in [Fig. 3-46(a) and (b)]. The results indicate that the equation can accurately calculate the drift ratio for deformation at the yield point. However, due to the stiffer secondary stiffness, the corresponding drift ratio is relatively lower for the deformation at the maximum force point, and Eq. (3-28) is deemed to be capable of evaluating the deformation within a safe side.

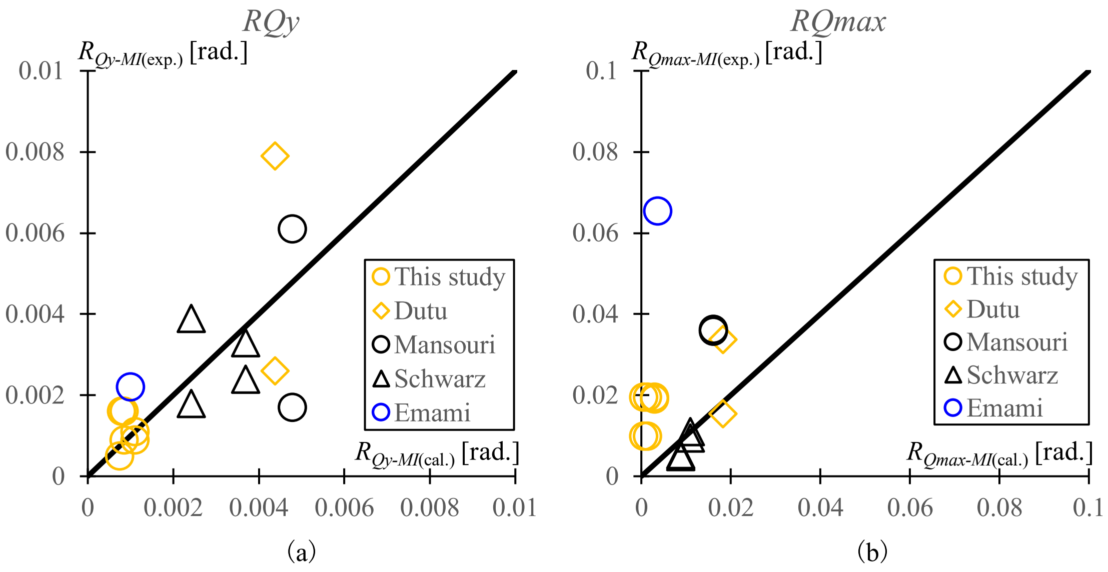

Fig. 3-46. Comparison between experimental value and calculated value of story drift ratio: (a) at yield strength, (b) at maximum strength.

3.4.3 Performance level of extracted infill

The limit state definition is based on the extracted infill performance and is defined by the results of in-plane cycle tests on various infilled frames (Fig. 3-47). As a result of the increasing extent of infill damage caused by in-plane actions, three limit states are introduced here:

(DS1) The infill wall can be used continually. This range extends from the origin to the infill's yield strength. Within this range, the infill wall is considered undamaged or has developed only a very small crack that does not require repair. As a result, the infill does not require repair and can continue to be used within this range.

(DS2) The infill wall should be retrofitted. The infill panel is expected to be damaged because of diagonal cracks that deform both joints and masonry units [Fig. 3-16(a)]. However, the infill can be effectively and economically retrofitted.

(DS3) The infill panel should be replaced. As the story drift increases, the frame keeps squeezing the infill panel in it until the panel is not able to be repaired [Fig. 3-16(c)]. During this limit, the infill wall is considered to be in danger of falling partly due to the squeezing, thus threatening the life safety of the building users.

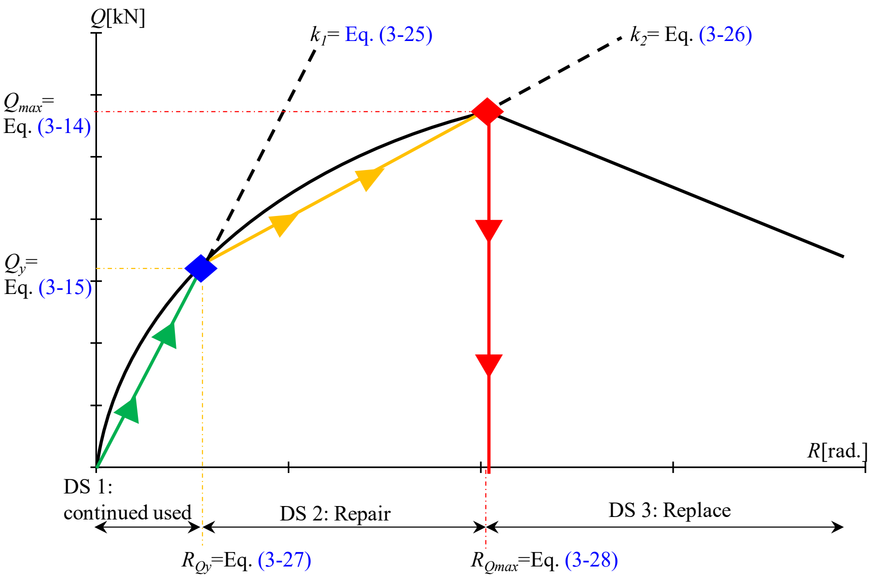

Fig. 3-47. Performance levels for masonry infill wall.

This study can be used to evaluate the damage state of masonry infill. Specifically, after the field investigation of the dimensions and material strength of the constructed masonry infill, the maximum story drift ratio and the corresponding horizontal load capacity can be calculated using the evaluation method developed in this study, and based on the story drift ratio of the surrounding structural components obtained from the investigation, a recommendation can be made regarding whether the masonry infill requires repair.

It is worth noting that although the in-plane performance level of infill is stated here, the damage caused by out-of-plane effects of the infill and frame failure should also be considered in practical applications.

To further verify the applicability of the equations for the performance level, the results of the calculation were applied to the hysteresis curves of the specimens, as illustrated in Fig. 3-48. As can be seen, the calculated curves closely match the hysteresis curves.

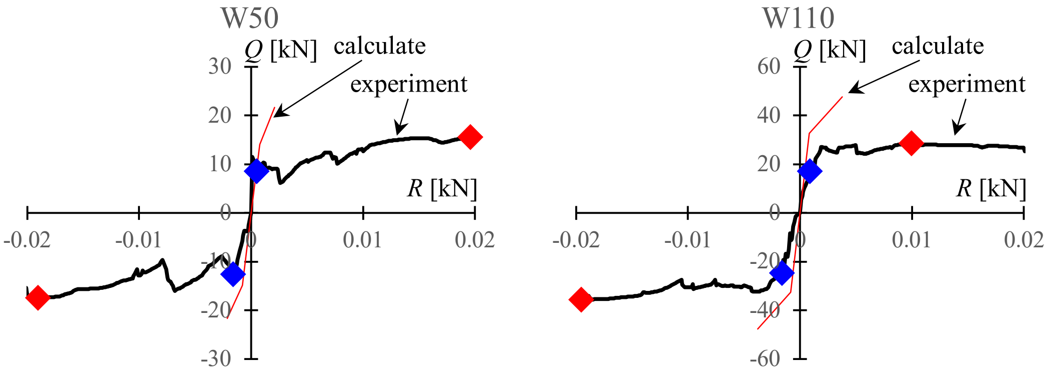

Specimen W50

Specimen W110

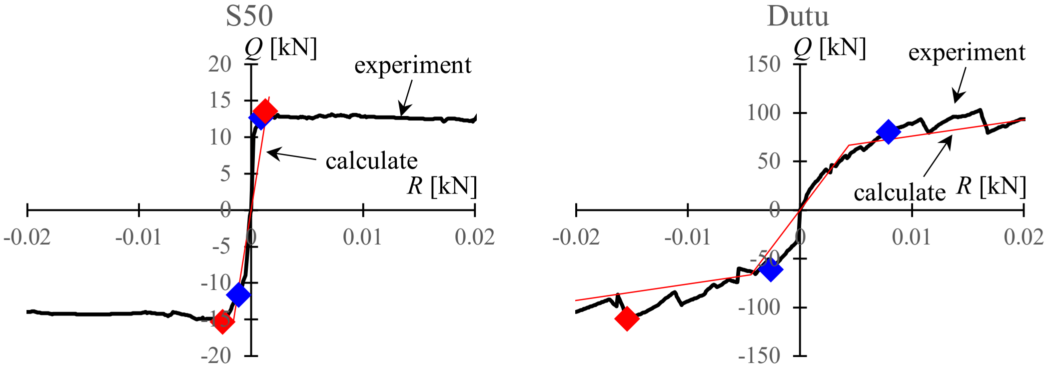

Specimen S50

Dutu et al.'s result[3-15]

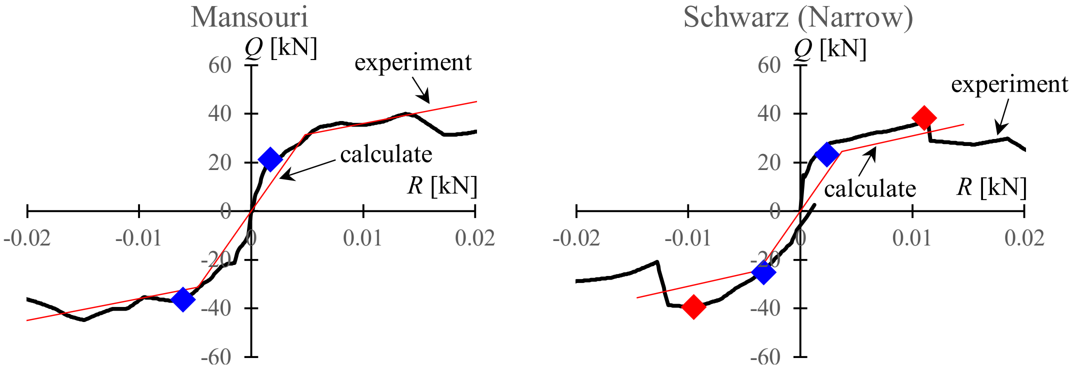

Mansouri et al.'s result[3-23]

Schwarz et al.'s result[3-24]

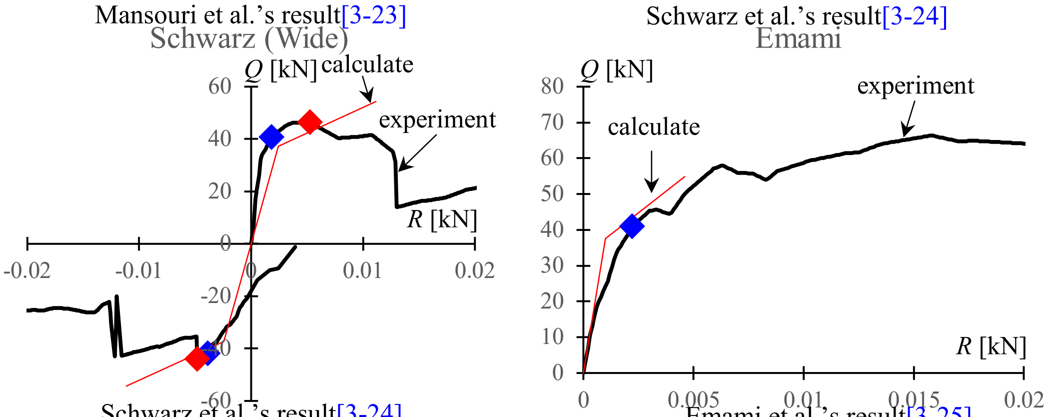

Schwarz et al.'s result[3-24]

Emami et al.'s result[3-25]

Fig. 3-48. Performance levels for specimens.

3.5 Summary and conclusions

An experimental test was conducted on Chuandou timber frames with masonry infills, which are a traditional timber structural system that continues being widely used for detached houses in South China. The current study is focused on the experimental investigation that conducted on solid brick masonry infills. Several full-scale Chuandou timber frame subassemblage specimens of various aspect ratios and masonry infill thicknesses were subjected to lateral cyclic loading. The following conclusions are drawn based on the test results.

The bare timber frames sustained up to 10% lateral drift ratio without losing its vertical stability to prevent collapse, while their lateral strength and stiffness are negligibly small compared to the masonry infills. Specifically, the initial stiffness of the masonry-infilled specimens were more than 100 times larger than that of the bare frame specimens even if the masonry infill was a shiner system. The lateral strength of infilled specimens was 3.7 to 10 times that of the bare frame specimens depending on the thickness and damage pattern of infill.

Although the timber frame and the masonry infill are responsible for two separate sets of loads, i.e., timber frame for gravity load and masonry infill for lateral load, there are complicated interactions between the two parts of the structural system. In particular, the slip at the free-standing timber column bases was found to be primarily attributed to the expansion of the masonry panel when it cracked in shear. A bare timber frame or an infill timber frame whose deformation was predominated by global rocking motion is not likely to sustain considerable slip at its column bases.

Depending on the relationship between their shear strength and rocking strength, the masonry-infilled Chuandou frames may fail in three different modes: rocking, shear and combined rocking and shear. The masonry panels of a shiner bond, which has become the most commonly-seen infill type in a Chuandou frame, are very likely to deform in the out-of-plane direction solely because of the in-plane shear and then collapse at an approximately 4% drift ratio. Either a stretcher system should be used or full-span embedded ties be provided for the masonry panels to prevent the premature collapse of the infills which may cause casualties.

A particular attention has been placed on the analysis of infill panel performance, resulting in identifying characteristic failure modes of the panel and the definition of performance levels to judge the limitation of retrofit. A series of equations were proposed to predict the strength, stiffness, and drift ratio of each characteristic point of the damage limit states. The observed damage during the test is reported and correlated with the respective damage limit states. Finally, although the attention of this study is mainly concentrated on the in-plane response of the infill panel, it is important to consider the possible additional limit states specific for the frame elements and the out-of-plane action on the infill panel.

Reference

[3-1] Qu Z, Dutu A, Zhong J, Sun J. Seismic damage to masonry-infilled timber houses in the 2013 M7.0 Lushan, China, Earthquake. Earthq Spectra 2015;31:1859-74.

[3-2] Chang W-S, Hsu M-F, Komatsu K. Rotational performance of traditional Nuki joints with gap I: theory and verification. J Wood Sci 2006;52:58-62.

[3-3] Chen C-J. The study on improved mechanical properties of reinforced traditional Chuan-Dou timber joints in Taiwan. J Cult Prop Conserv 2008;1:5-14.

[3-4] Huang H, Wu Y, Li Z, Sun Z, Chen Z. Seismic behavior of Chuan-Dou type timber frames. Eng Struct 2018;167:725-39.

[3-5] GB/T 1936.1-2009. Method of testing in bending strength of wood. Beijing, China: Standardzation Administration of China; 2009.

[3-6] GB/T 1935-2009. Method of testing in compressive strength parallel to grain of wood. Beijing: China’ National Standard; 2009.

[3-7] GB 50009-2012, Load code for the design of building structures, 2012.

[3-8] Wang T., Historical Chinese timber construction exploration. Beijing: Cultural Relic Press, 1992. p.14-19, p.158-162.

[3-9] ISO. Timber structures – joints made with mechanical fasteners – Quasi-static reversed-cyclic test method. ISO/TC 165 WD 16670. Canada: Secretariat, Standards Council of Canada; 2003.

[3-10] Ali Q, Schacher T, Ashraf M, Alam B, Naeem A, Ahmad N et al. In-plane behavior of the Dhajji-Dewari structural system (Wooden braced frame with masonry infill). Earthq Spectra 2012;28:835-58.

[3-11] Poletti, E., & Vasconcelos, G. Seismic behaviour of traditional timber frame walls: experimental results on unreinforced walls. Bulletin of Earthquake Engineering 2015, 13(3), 885–916.

[3-12] Sakata H, Yamazaki Y, Ohashi Y. A study on moment resisting behavior of mortise-tenon joint with dowel or split wedge. In: 15th World Conference on Earthquake Engineering, Lisbon, Portugal; 2012.

[3-13] FEMA. NEHRP guidelines for seismic rehabilitation of buildings. FEMA 273. Redwood City, CA: Applied Technology Council; 1997.

[3-14] GB 50003-2011. Code for design of masonry structures, 2011.

[3-15] Dutu A, Sakata H, Yamazaki Y, Shindo T. In-plane behavior of timber frames with masonry infills under static cyclic loading. J Struct Eng 2016;142:04015140.

[3-16] Xie Q., Tong Y., Zhang L., Li S. and Wang L., Seismic Behavior of Chinese Traditional Timber Frames with Masonry Infill Wall: Experimental Tests and Hysteretic Model, International Journal of Architectural Heritage, DOI: 10.1080/15583058.2019. 1665140

[3-17] T. Paulay and M.J.N Priestley Seismic design of reinforced concrete and masonry buildings, John Wiley & Sons, Inc., 1992, p.565, pp. 589-590.

[3-18] F. J. Crisafulli, Seismic behavior of reinforced concrete structures with masonry infills, doctoral thesis of University of Canterbury Christchurch, New Zealand.

[3-19] Riddington J., Ghazali M., Shear strength of masonry walls, proceedings of the eighth international brick and block masonry conference, Dublin, Republic of Ireland, September, 1988, Vol. 1, pp. 548-558

[3-20] Kobayashi S., Shindo T., Dutu A., Sakata H., Yamazaki Y., Analytical Study on Mechanical behavior of Timber Framed Masonry Wall, Summaries of Technical Papers of Architectural Institute of Japan Annual Conference Sep. 2014, pp.883-884. (in Japanese)

[3-21] G. H. Nalon, C. F. R. Santos, L. G. Pedroti, J. C. L. Ribeiro, G. S. Veriussimo and F. A. Ferreira, Strength and failure mechanisms of masonry prisms under compression, flexure and shear: Components' mechanical properties as design constraints, Journal of Building Engineering 28 (2020) 101038. https://doi.org/10.1016/j.jobe.2019.101038

[3-22] Kaushik, H. B., D. C. Rai, and S. K. Jain. 2007. "Stress-strain characteristics of clay brick masonry under uniaxial compression." J. Mater. Civ. Eng. 19 (9): 728–739. https://doi.org/10.1061/(ASCE)0899-1561(2007)19:9(728).

[3-23] A. Mansouri, M. S. Marefat,and M. Khanmohammadi, Experimental evaluation of seismic performance of low-shear strength masonry infills with openings in reinforced concrete frames with deficient seismic details, Struct. Design Tall Spec. Build. 23, 1190–1210 (2014), DOI: 10.1002/tal.1115

[3-24] S. Schwarz, A. Hanaor, D.Z. Yankelevsky, Experimental Response of Reinforced Concrete Frames With AAC Masonry Infill Walls to In-plane Cyclic Loading, Structures 3 (2015) 306–319, https://doi.org/10.1016/j.istruc.2015.06.005

[3-25] S. M. M. Emami and M. Mohammadi, Effect of frame connection rigidity on the behavior of infilled steel frames, Earthquakes and Structures, Vol. 19, No. 4 (2020) 227-241 DOI: https://doi.org/10.12989/eas.2020.19.4.227

[3-26] Morandi P., Hak S., Magenes G., Performance-based interpretation of in-plane cyclic tests on RC frames with strong masonry infills, Engineering Structures, Volume 156, 1 February 2018, pp. 503-521

[3-27] Hak S., Morandi P., Magenes G. Evaluation of infill strut properties based on in-plane cyclic tests. Gradevinar 2013;65(6):509-22

[3-28] Xie X., Zhang L., Qu Z., A Critical Review of Methods for Determining the Damage States for the In-plane Fragility of Masonry Infill Walls, Journal of earthquake engineering, Oct 2020. DOI: https://doi.org/10.1080/13632469.2020.1835749.

[3-29] T. Turgay, M. C. Durmus, B. Binici, G. Ozcebe, Evaluation of the Predictive Models for Stiffness, Strength, and Deformation Capacity of RC Frames with Masonry Infill Walls, Journal of Structural Engineering, Volumn 140 Issue 10 - October 2014, DOI: 10.1061/(ASCE) ST.1943-541X.0001069

[3-30] M. Minotto, N. Verlato, M, Donà, F. Porto, Strengthening of In-Plane and Out-of-Plane Capacity of Thin Clay Masonry Infills Using Textile and Fiber-Reinforced Mortar, journal of Composites for Construction, Volumn 24 Issue 6 - December 2020, DOI: https://doi.org/10.1061/(ASCE)CC.1943-5614.0001067

[3-31] Stafford Smith, B. and Carter, C., A method of analysis for infilled frames, Proceeding of the Institution of Civil Engineers, Vol.44, 1969, pp. 31-48.

[3-32] Riddington J.R. and Stafford Smith B. Analysis of Infilled Frames Subjected to Racking with Design Recommendations. The structural engineer, vol.55, No.6, 1977, pp.263-268

[3-33] Mainstone R. J., On the stiffnesses and strengths of infilled frames, Proceedings of the institution of civil engineers, 1971, Supplement IV, pp. 57-90.

[3-34] Liauw, T. C. and Kwan, K. H., Nonlinear behaviour of Non-integral infilled frames, computers & structures, Vol.18, No.3, 1984, pp.551-560

[3-35] AIJ standard for Structural Calculation of Reinforced Concrete Structures, Architectural Institute of Japan; 2018. Maruzen Publishing, 2018. pp.55-64.

Appendix I

When the specimens is assembled, the clearance of each point in Fig. AI-1 was measured and recorded in Table AI-2. It should be noted that for the five specimens: L12.5*1, L12.5*1(dp100), L12.5*1(V), L21*1, and L12.5*4@455, although their clearances are managed during the assembly, the specific clearances were not measured, and only their design values are shown here.

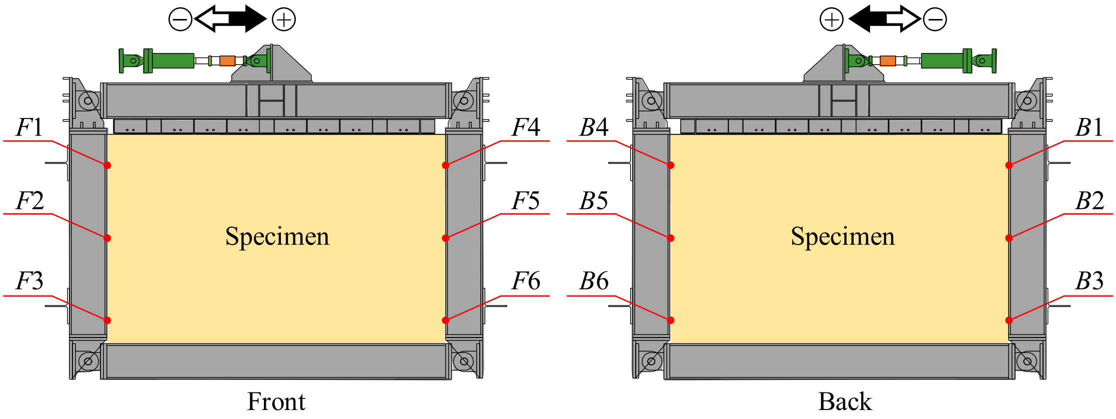

Fig. AI-1. Measurement of clearance.

Table AI-1. Measured clearance

		F1	F2	F3	F4	F5	F6	R1	R2	R3	R4	R5	R6
S12.5*1	Inner	6	6	6	5	5	8						
	Outer												
S12.5*2	Inner	6	5	6	4	6	6						
	Outer	6	5	5	5	5	7						
S12.5*4	Inner	7	5	5	5	5	6	6	5	5	5	5	5
	Outer	6	4	5	5	5	6	5	5	6	5	5	6
M12.5*1	Inner	5	5	6	5	6	7						
	Outer												
M12.5*2	Inner	6	6	5	4	6	5						
	Outer	10	4	6	6	7	6						
M12.5*4	Inner	5	5	4	4	5	5	5	5	5	5	5	5
	Outer	10	5	5	5	5	5	5	6	5	5	5	5
L12.5*1#	Inner	5	5	5	5	5	5						
	Outer												
L12.5*1(dp100)#	Inner	5	5	5	5	5	5						
	Outer												
L12.5*1(V)#	Inner	5	5	5	5	5	5						
	Outer												
L12.5*2@455	Inner	5	6	5	6	6	7						
	Outer	4	5	6	5	5	6						
L12.5*2@303	Inner	7	8	7	5	5	5						
	Outer	5	5	5	5	5	6						
L12.5*4@455#	Inner	5	5	5	5	5	5	5	5	5	5	5	5
	Outer	5	5	5	5	5	5	5	5	5	5	5	5
L12.5*4@303	Inner	7	6	6	6	7	7	6	5	5	5	6	7
	Outer	6	7	7	6	5	5	5	5	5	7	5	6
L21*1#	Inner	5	5	5	5	5	5						
	Outer												
L21*2	Inner	5	5	6	5	5	5						
	Outer	5	5	6	6	5	6						

#: No measurement was performed, design values are shown in the table.

Appendix II

The damage development of specimen S12.5*2 are shown as follows.

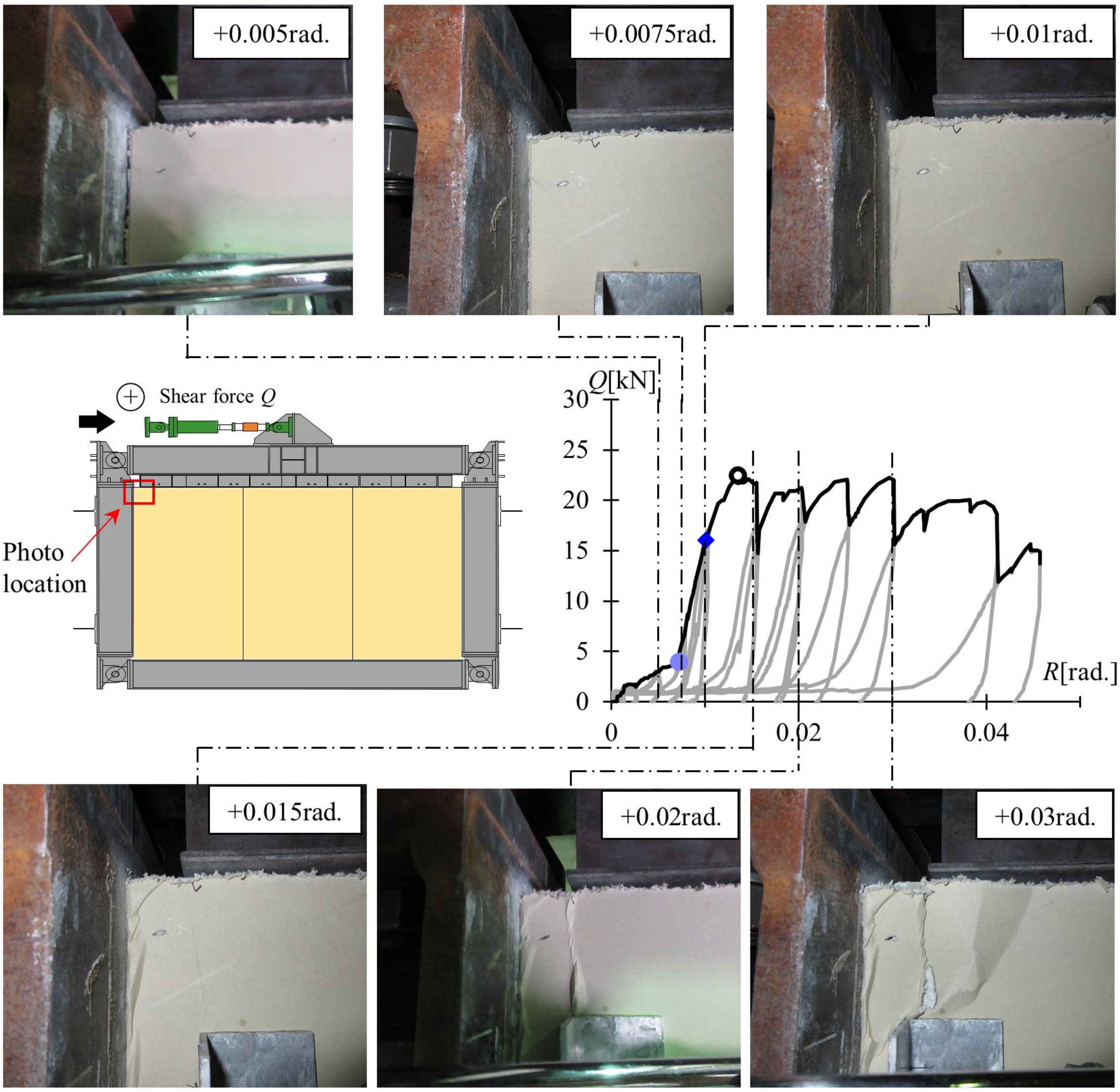

Fig. AII-1. Damage to the gypsum board at loading cycle from 0.005 rad to 0.03 rad (Specimen S12.5*2, top left corner).

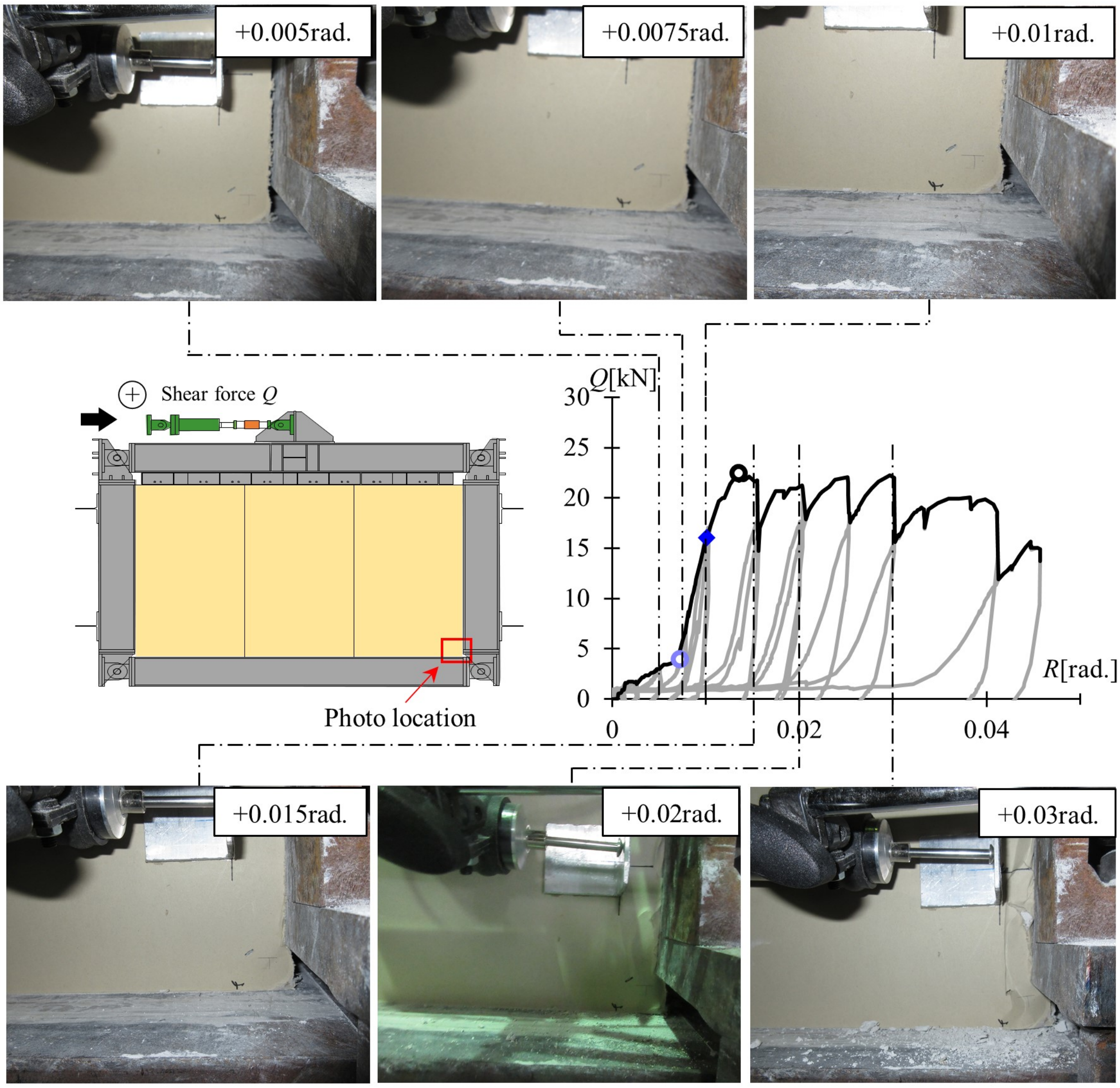

Fig. AII-2. Damage to the gypsum board at loading cycle from 0.005 rad to 0.03 rad (Specimen S12.5*2, lower right corner).

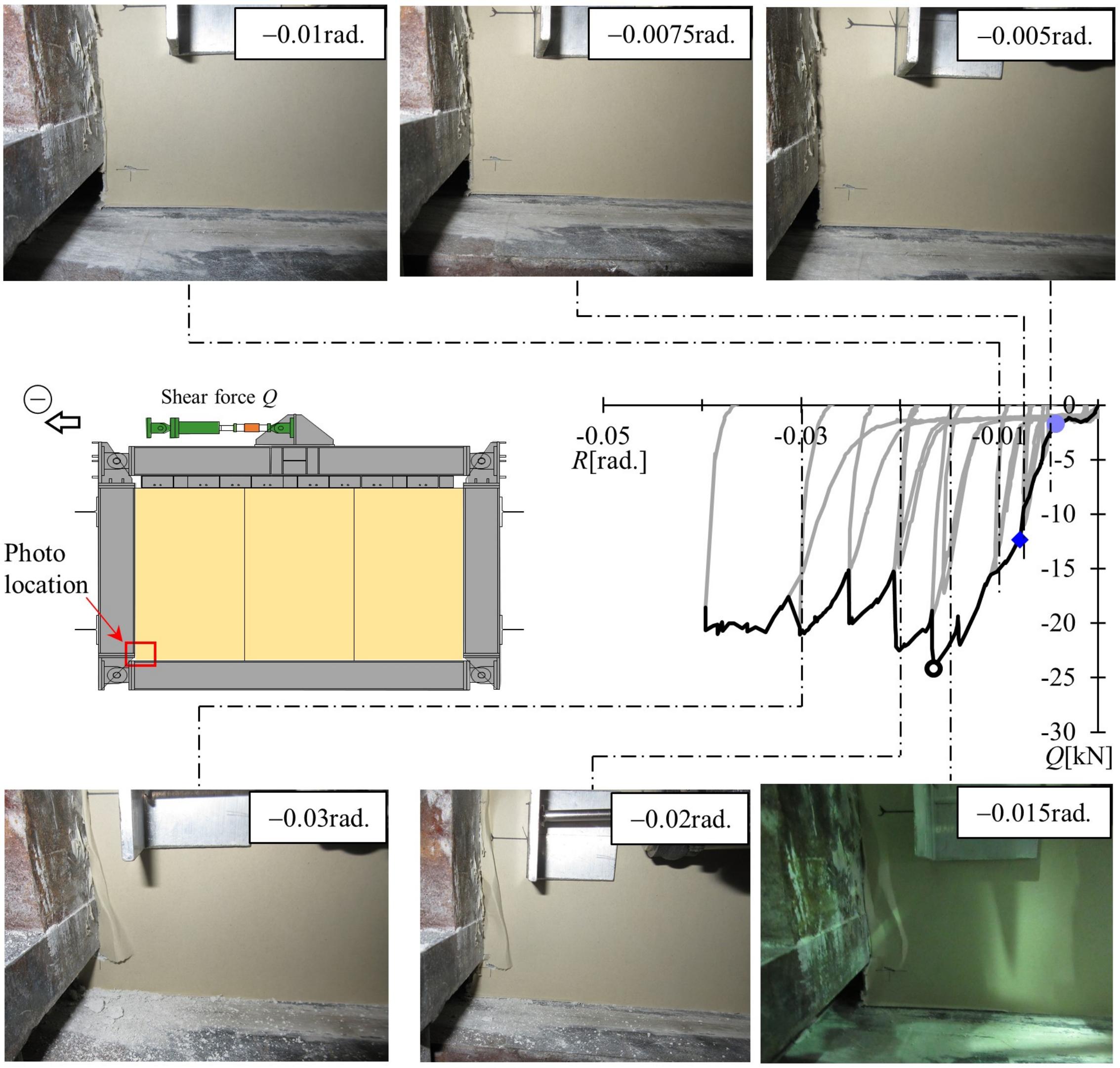

Fig. AII-3. Damage to the gypsum board at loading cycle from 0.005 rad to 0.03 rad (Specimen S12.5*2, lower left corner).

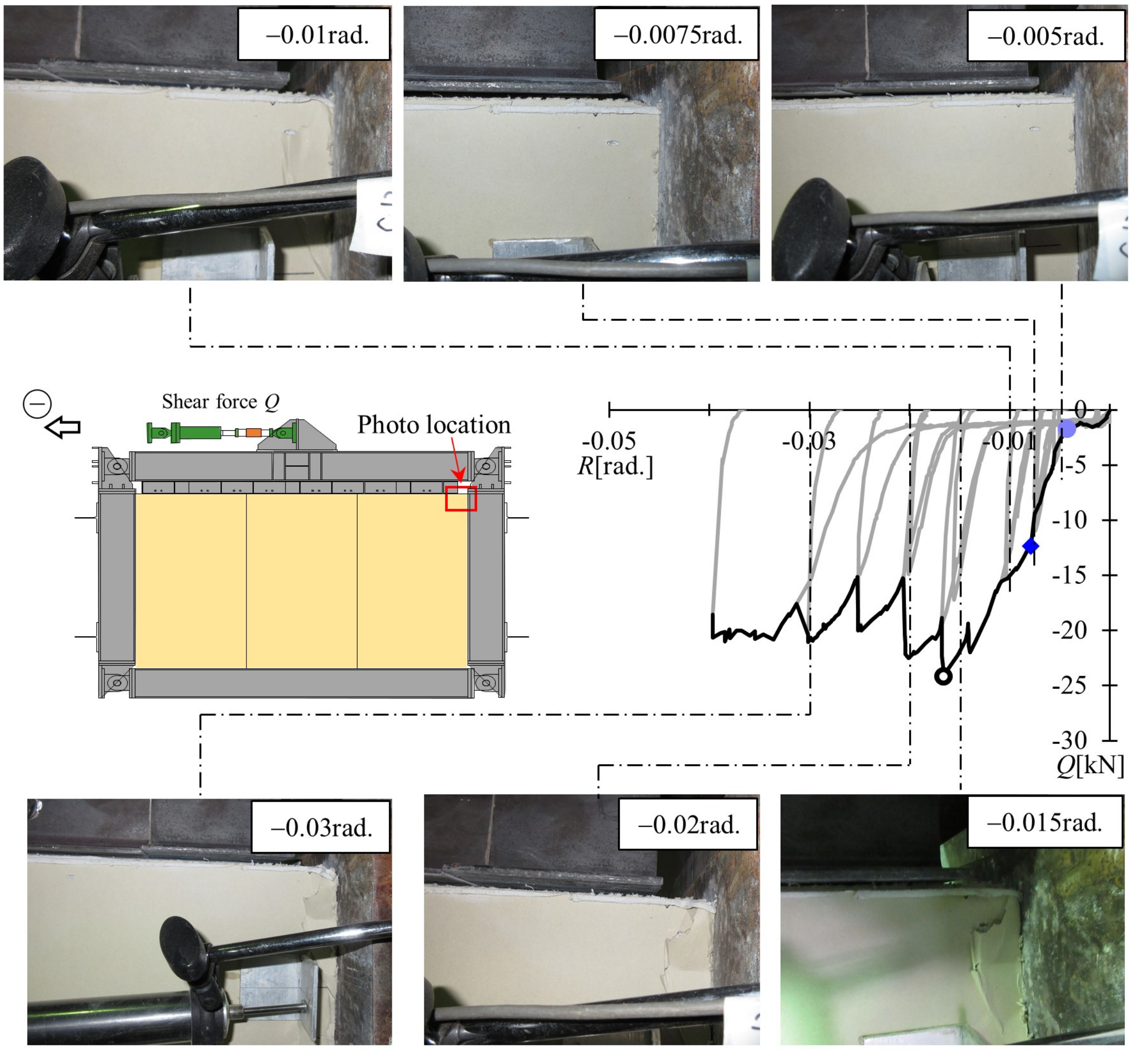

Fig. AII-4. Damage to the gypsum board at loading cycle from 0.005 rad to 0.03 rad (Specimen S12.5*2, top right corner).

The damage development of specimen S12.5*4 are shown as follows.

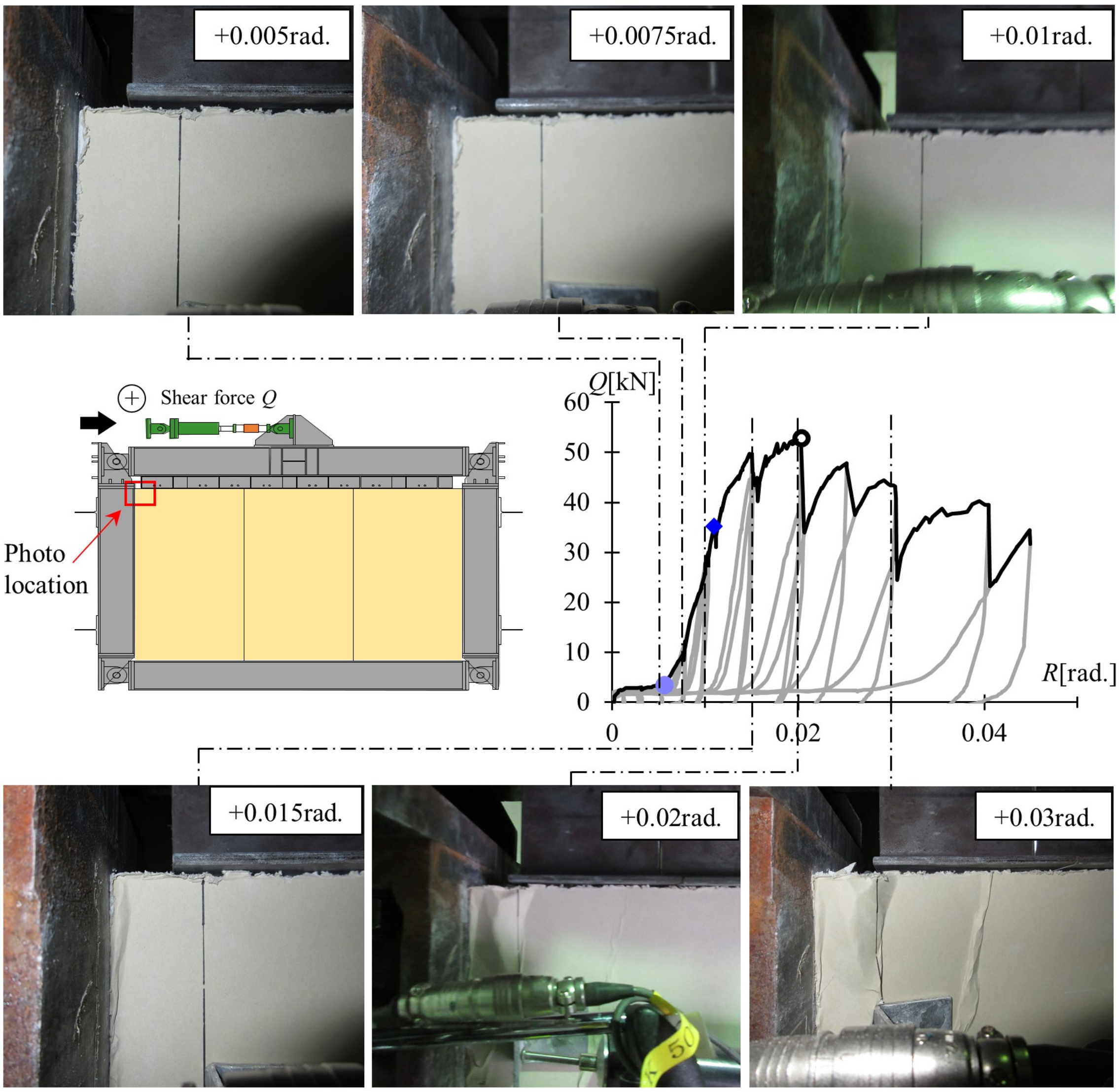

Fig. AII-5. Damage to the gypsum board at loading cycle from 0.005 rad to 0.03 rad (Specimen S12.5*4, top left corner, front).

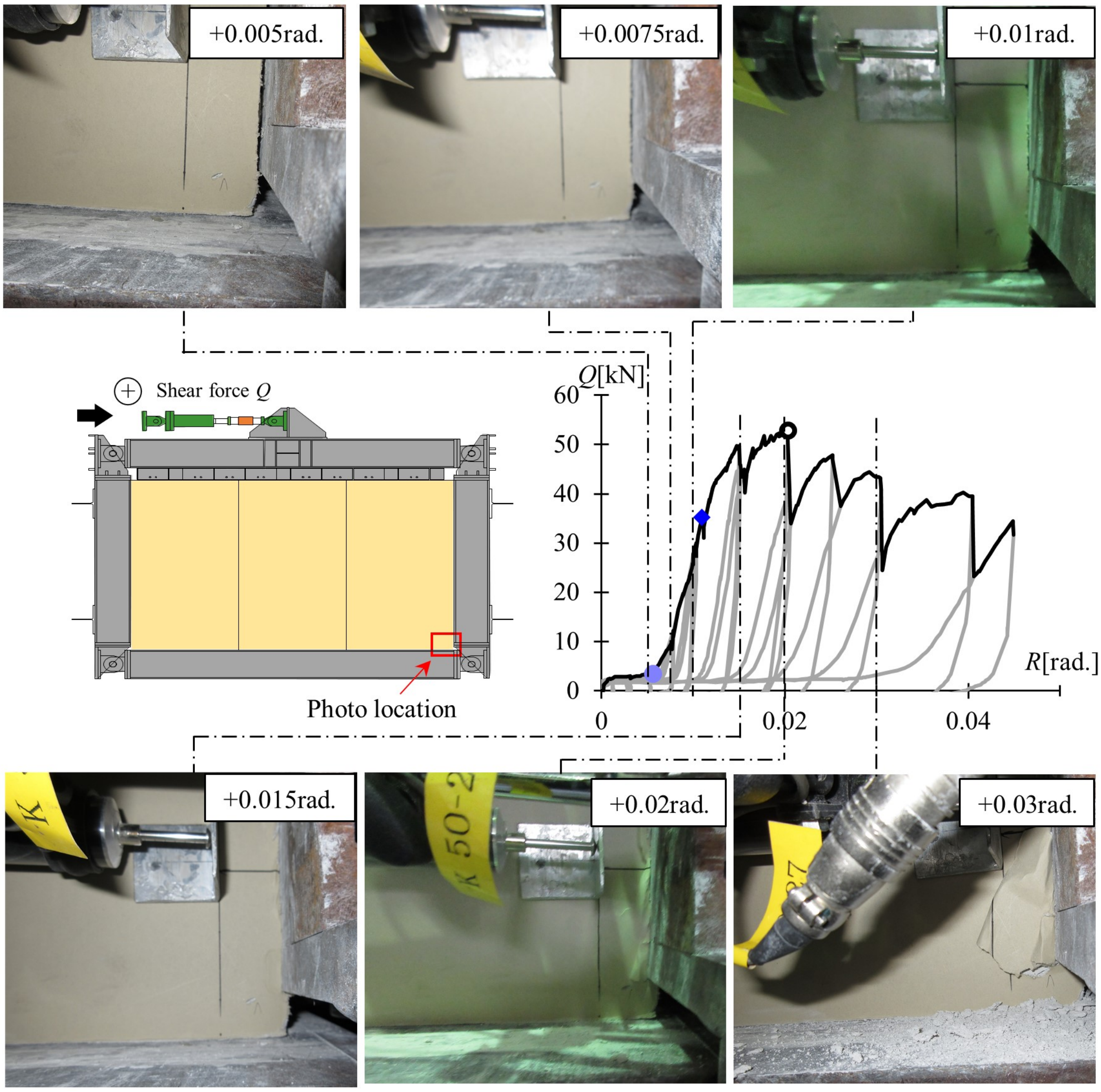

Fig. AII-6. Damage to the gypsum board at loading cycle from 0.005 rad to 0.03 rad (Specimen S12.5*4, lower right corner, front).

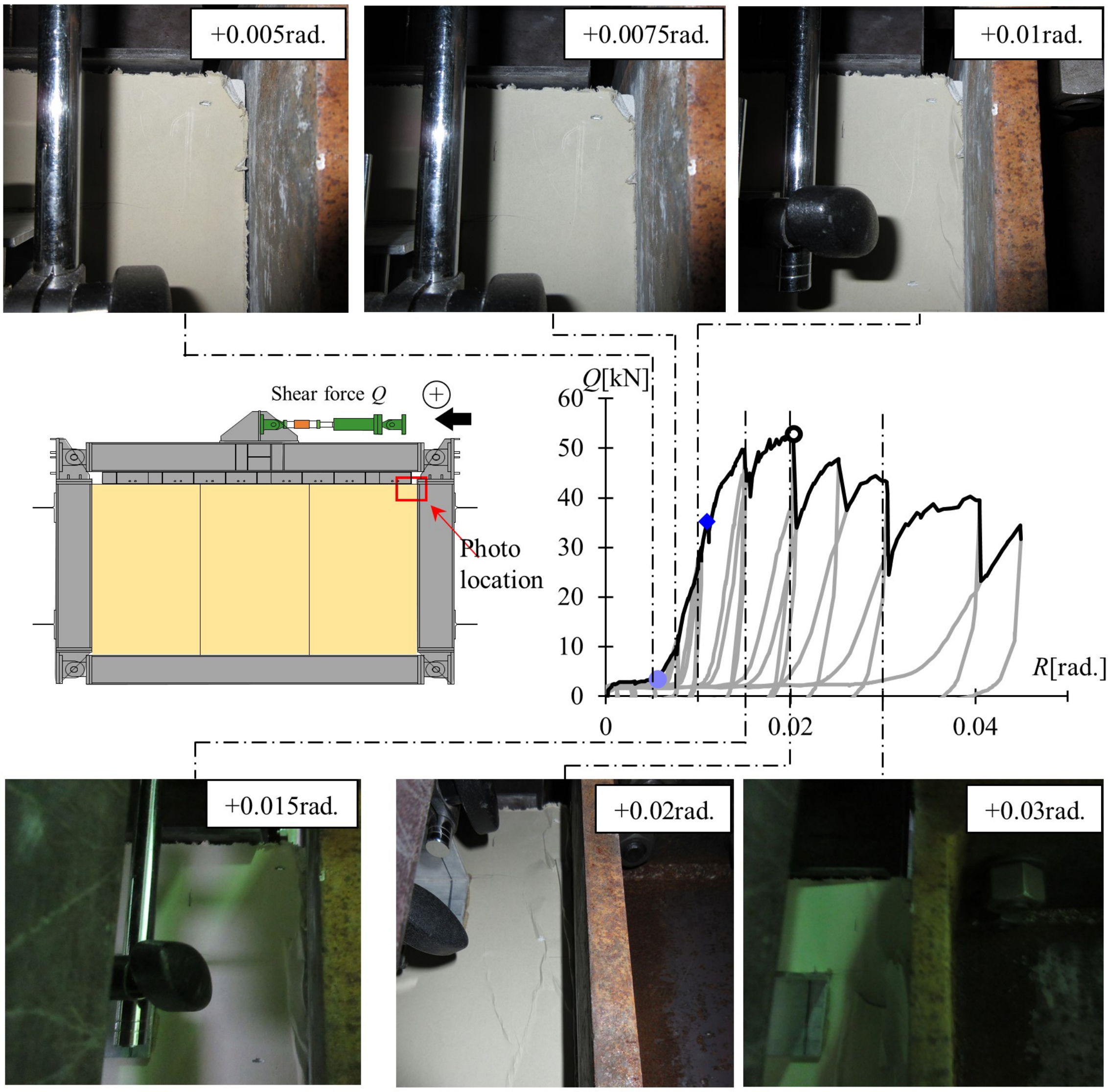

Fig. AII-7. Damage to the gypsum board at loading cycle from 0.005 rad to 0.03 rad (Specimen S12.5*4, top right corner, reverse).

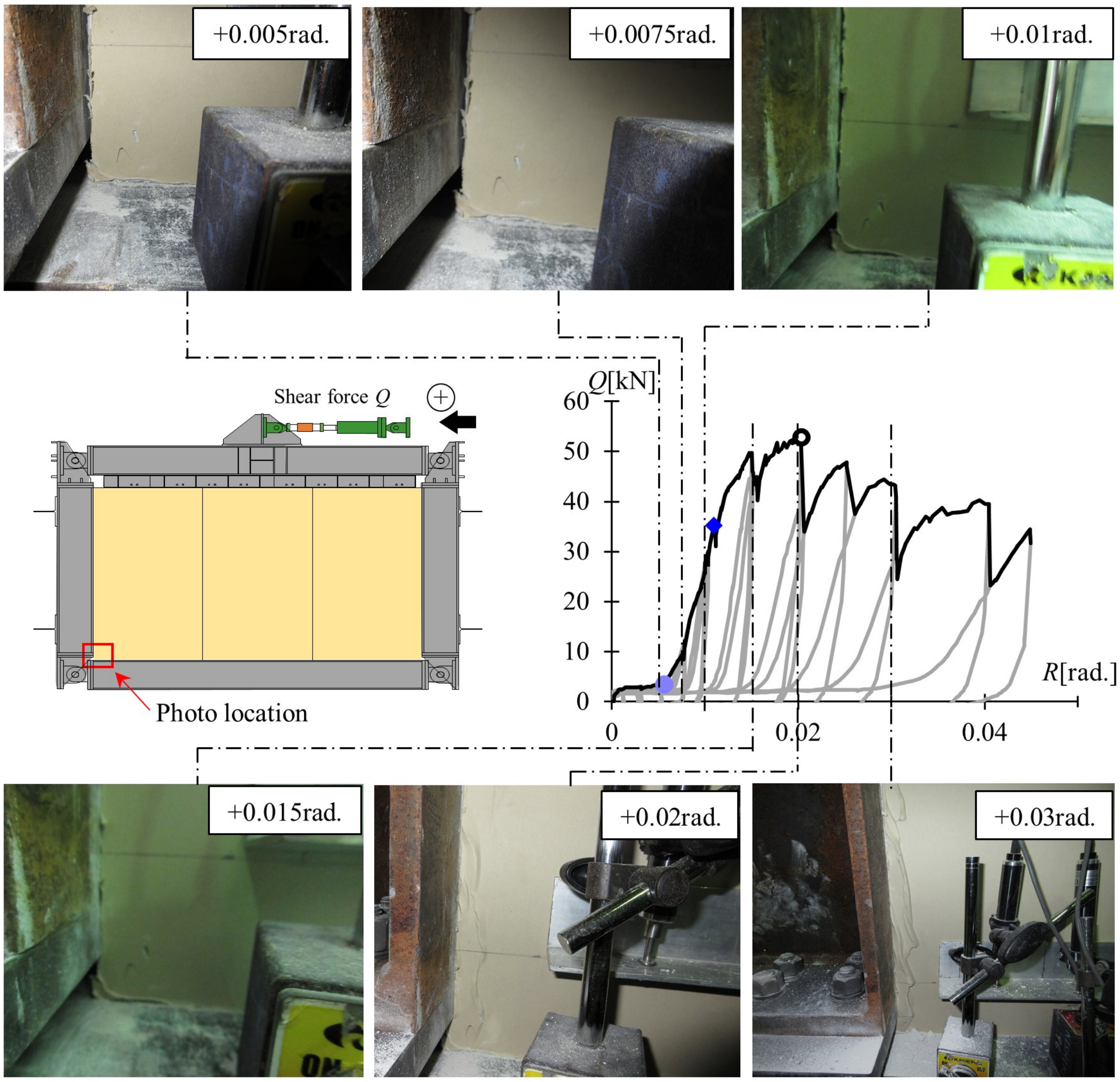

Fig. AII-8. Damage to the gypsum board at loading cycle from 0.005 rad to 0.03 rad (Specimen S12.5*4, lower left corner, reverse).

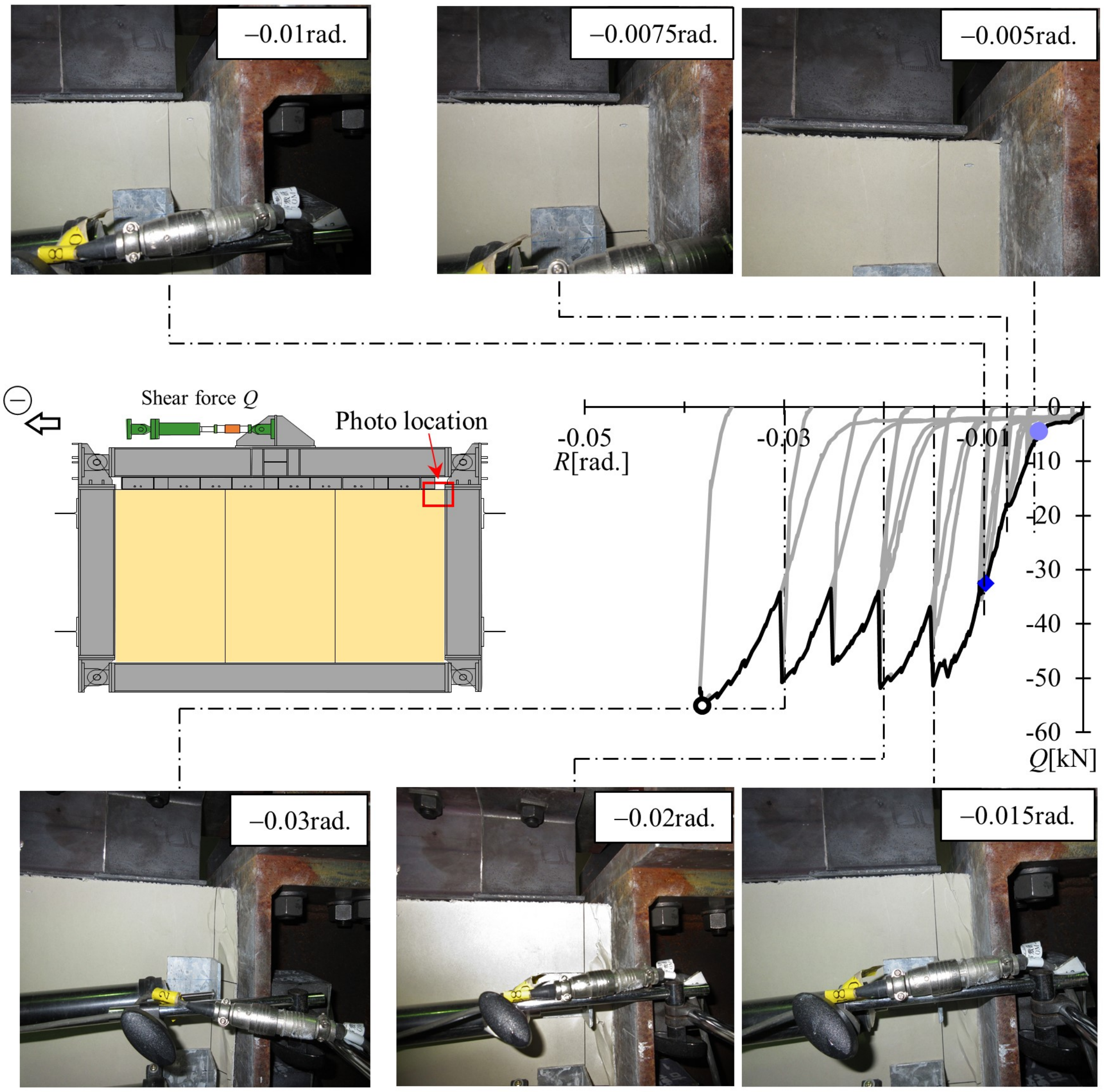

Fig. AII-9. Damage to the gypsum board at loading cycle from 0.005 rad to 0.03 rad (Specimen S12.5*4, top right corner, front).

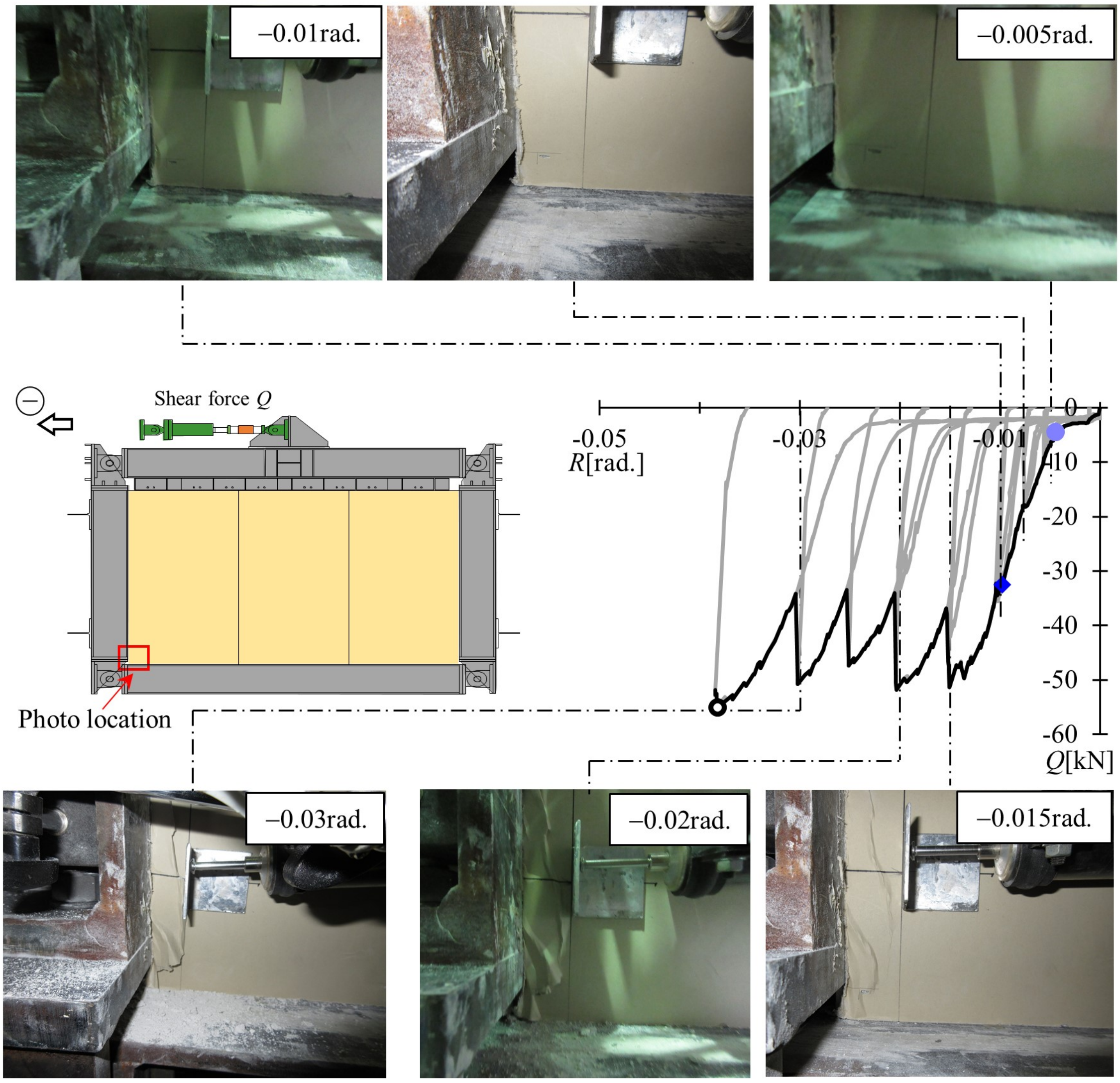

Fig. AII-10. Damage to the gypsum board at loading cycle from 0.005 rad to 0.03 rad (Specimen S12.5*4, lower left corner, front).

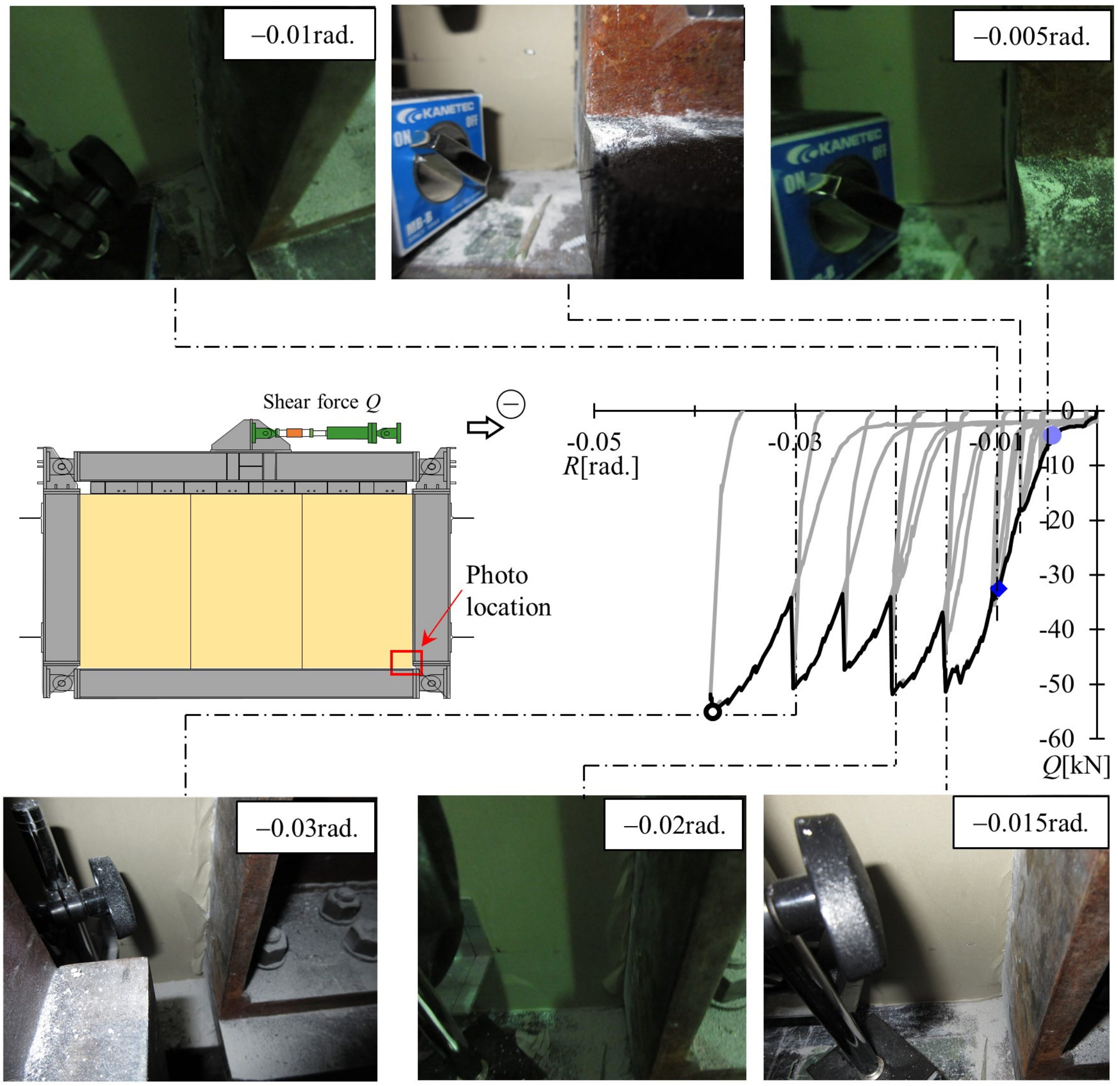

Fig. AII-11. Damage to the gypsum board at loading cycle from 0.005 rad to 0.03 rad (Specimen S12.5*4, lower right corner, reverse).

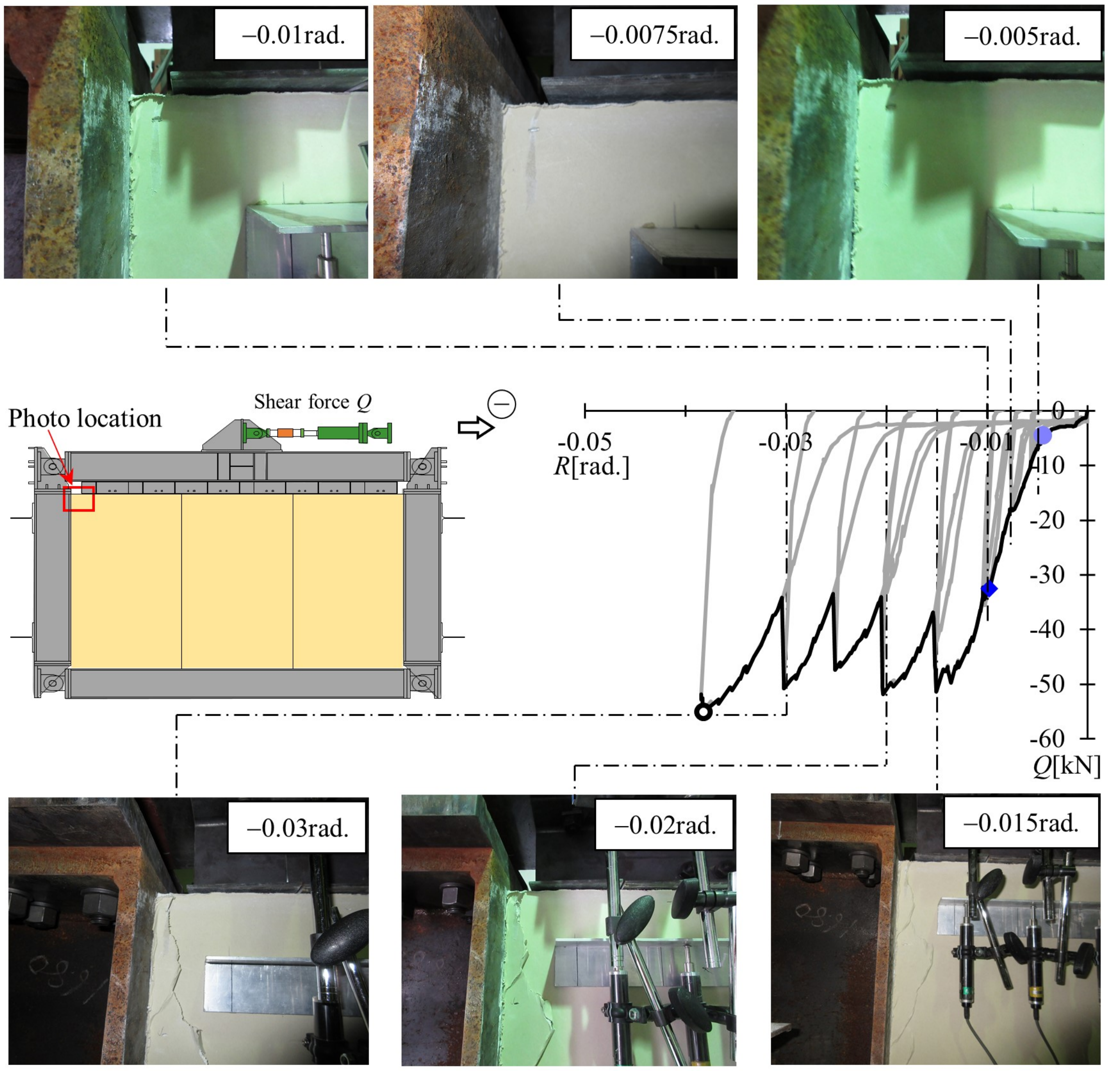

Fig. AII-12. Damage to the gypsum board at loading cycle from 0.005 rad to 0.03 rad (Specimen S12.5*4, top left corner, reverse).

Appendix III

In this experiment, the clearance between the specimen and the loading frame is set to 5mm, and as the story drift ratio R increases, the displacement when the loading frame is about to contact with the gypsum panel is considered as the sum of the the clearance value on the diagonal direction. The average clearance is calculated by summing the clearances on both diagonals of the specimen when there is gypsum panel on both sides of the specimen (i.e., n=4). To calculate the displacement at this moment, Eqs. AIII-1 is used.

＋ loading direction $$\mathit{\Delta}_S = 2c \approx \frac{(F1+F6)+(B1+B6)}{2} \qquad \text{(AIII-1a)}$$

－ loading direction $$\mathit{\Delta}_S = 2c \approx \frac{(F3+F4)+(B3+B4)}{2} \qquad \text{(AIII-1b)}$$

where $F1$,$F3$,$F4$,$F6$,$B1$,$B3$,$B4$,B6 is measured clearance when assembling the specimen, the measured location can refer to the Fig. AII-1.

The displacement $\mathit{\Delta}_S$ is obtained by multiplying the story drift ratio R, which was measured in the experiment, by the vertical distance ($H+H_P$) from the uppermost edge of the gypsum panel to the center of the lower pin (Fig.AIII-1). And $\mathit{\Delta}$ is calculated by Eq.AIII-2.

$$\mathit{\Delta}_S = R \times (H + H_P) \qquad \text{(AIII-2)}$$

R : story drift ratio, obtained by Eq.(2-3).

H : Height of gypsum panel.

H_P: Height of the center of lower pin to the lowermost edge of the gypsum panel.

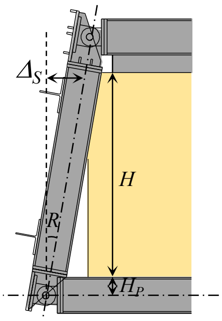

Fig. AIII-1. Calculation of displacement $\mathit{\Delta}_S$.

Replace the horizontal axis of Fig. 2-12 with Δ_S, and then represent the measured clearance value in Fig. AIII-3. As can be seen from the figure, after the displacement Δ_S reaches the clearance value, a significant force promotion can be identified. Therefore, based on the observed phenomena, it can be found that the specimen slides horizontally in the metal track at the initial loading cycles.

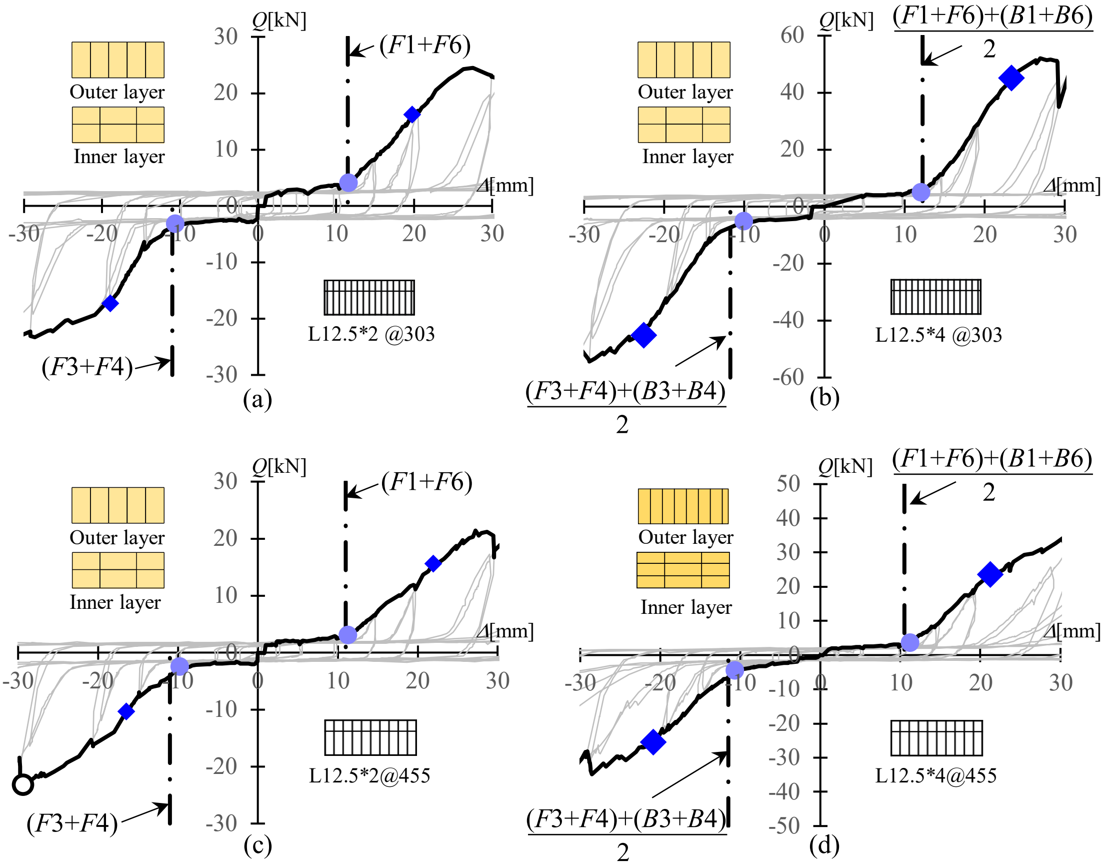

Figure continue on the next page.

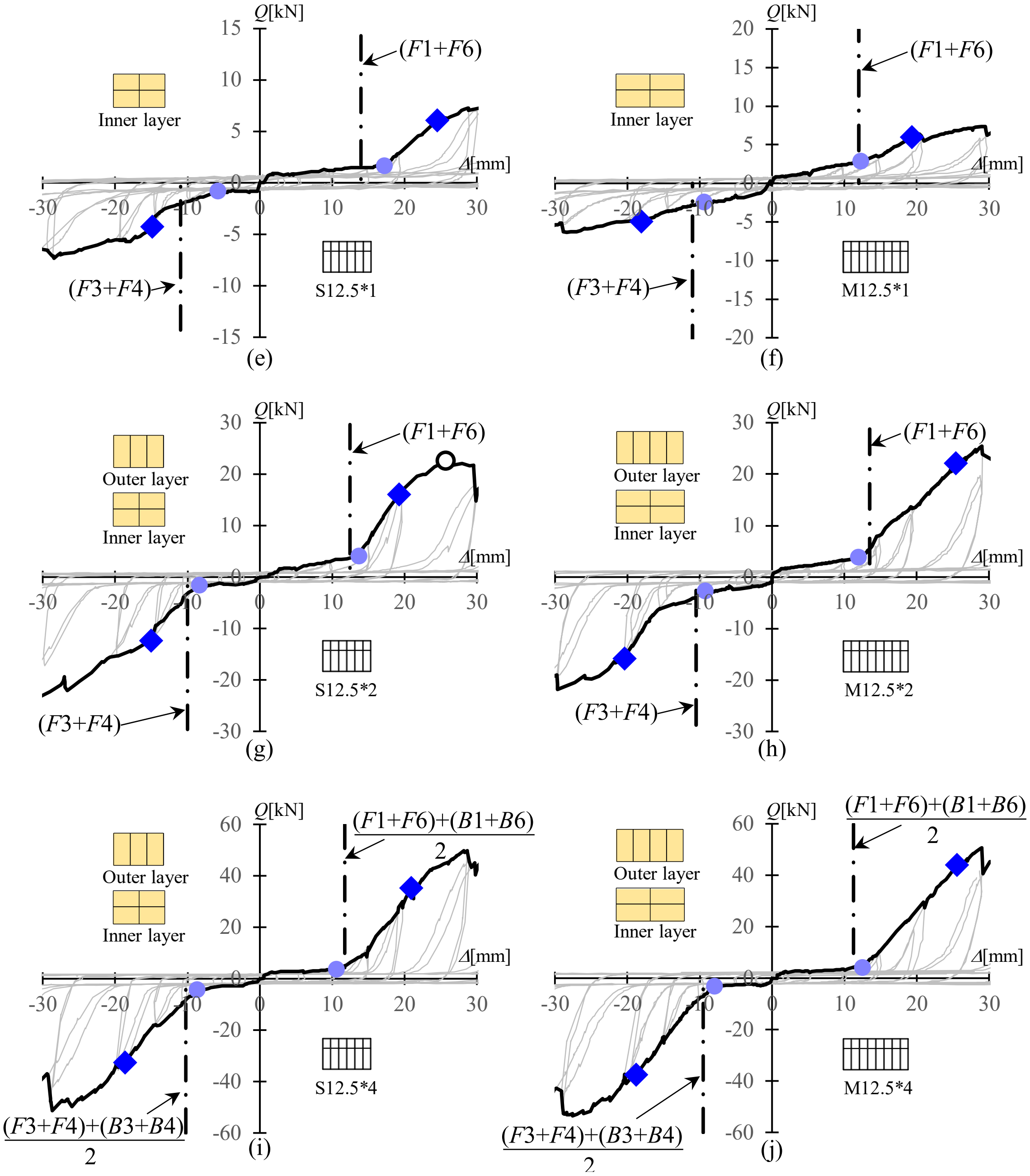

Fig. AIII-3. Hysteresis curves and clearance : (a) specimen L12.5*2@303, (b) specimen L12.5*4@303, (c) specimen L12.5*2@455, (d) specimen L12.5*4@455, (e) specimen S12.5*1, (f) specimen M12.5*1, (g) specimen S12.5*2, (h) specimen M12.5*2, (i) specimen S12.5*4, (j) specimen M12.5*4.

Appendix IV

The stress-strain relationships for the gypsum boards used in this study were based on material tests on gypsum boards conducted by Sato Y. et al. [IV-1], who performed compressive material tests on gypsum boards produced by two companies commonly used in the Japanese building materials market. For each company's gypsum boards, they were distinguished by long and short edges into parallel-grain direction and perpendicular-grain direction. However, for LGS wall, the inner layer and the outer layer are usually placed with crisscross configuration, thus the author considers that the average value of the parallel-grain direction and perpendicular-grain direction should be used for calculating the compressive capacity of the LGS wall. According to the above analysis, there are three different compressive strengths (i.e.: parallel-grain direction, perpendicular-grain direction, and the average) and modulus of elasticity for each company of gypsum board, totaling two companies, i.e., there are six different stress-strain relationships for gypsum board with 12.5 mm thickness. In addition, Sato Y. et al. conducted material tests for 21 mm gypsum board. All the results are recorded in Table AIV-1.

It is worth noting that gypsum board is a brittle material, only very few gypsum boards can still see a decreasing trend after reaching its maximum strain according to Sato Y. 's experiments [IV-1] (see R-12.5-P-B in Fig. AIV-1), and in this study, the ultimate strain for all boards is assumed to be 1.5 times the strain in Table AIV-1.

Table AIV-1 Data of material test [IV-1]

Type	Direction	Company	Compression strength [MPa]	strain	Modulus of elasticity [N/mm2]
GB-F12.5	P	A	4.88	0.002	2440.00
GB-F12.5	O	A	4.36	0.002	2180.00
	Average	A	4.62	0.002	2310.00
GBF12.5	P	B	6.05	0.0026	2326.92
GBF12.5	O	B	5.47	0.0028	1953.57
	Average	B	5.76	0.0027	2140.25
GBF21	P	A	5.24	0.003	1746.67
GBF21	O	A	4.52	0.0024	1883.33
	Average	A	4.88	0.0027	1815.00
GBF21	P	B	5.73	0.0026	2203.85
GBF21	O	B	4.54	0.0021	2161.90
	Average	B	5.14	0.0024	2182.88

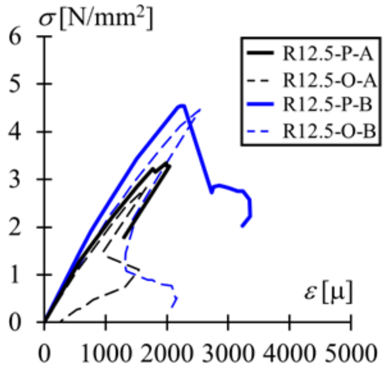

Fig. AIV-1. Example of material test data of [IV-1].

The calculation-experimental relationship and the parametrically analyses are shown below.

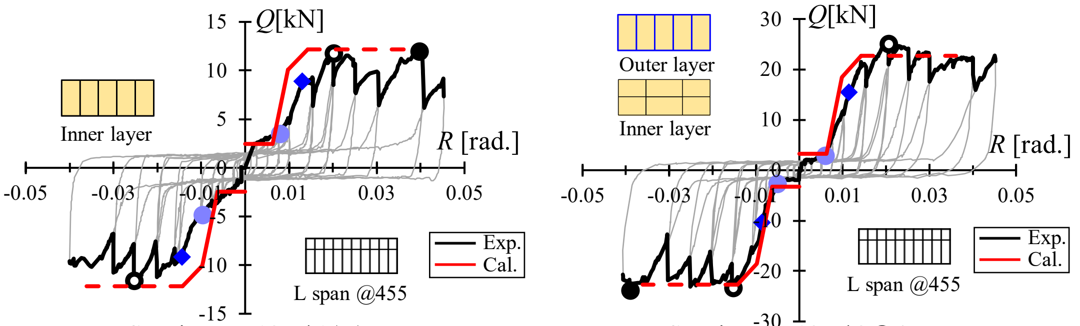

Specimen L12.5*1(V)   Specimen L12.5*2@455

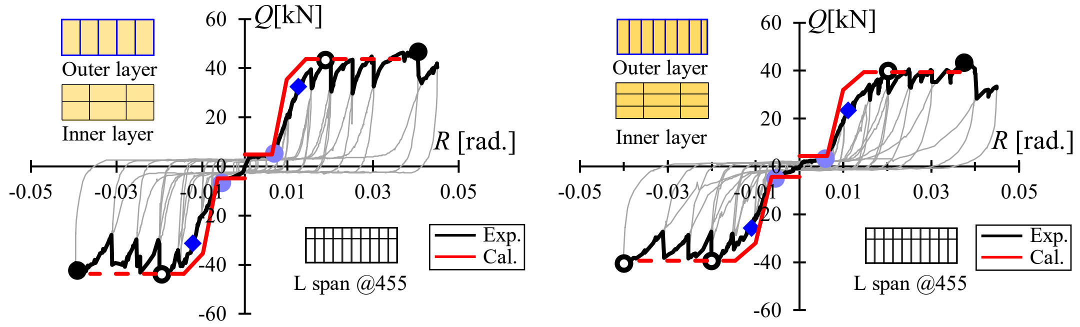

Specimen L12.5*4@455   Specimen L21*2

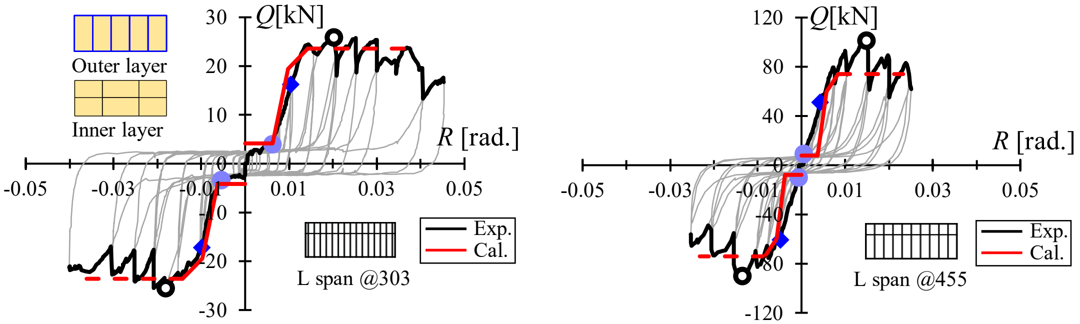

Specimen L12.5*4@303   Specimen No.1 (Isoda et al.[IV-2])

Fig. AIV-2. Verification of material test data board OA of [IV-1].

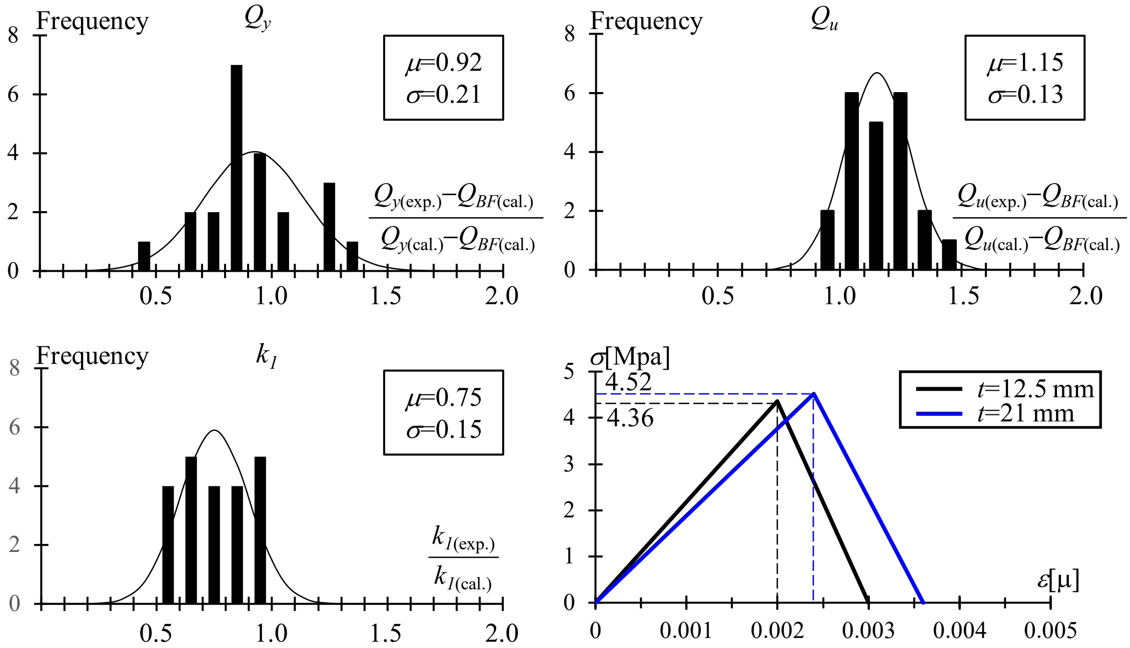

Fig. AIV-3. Parametrically analyses of board OA of [AIV-1].

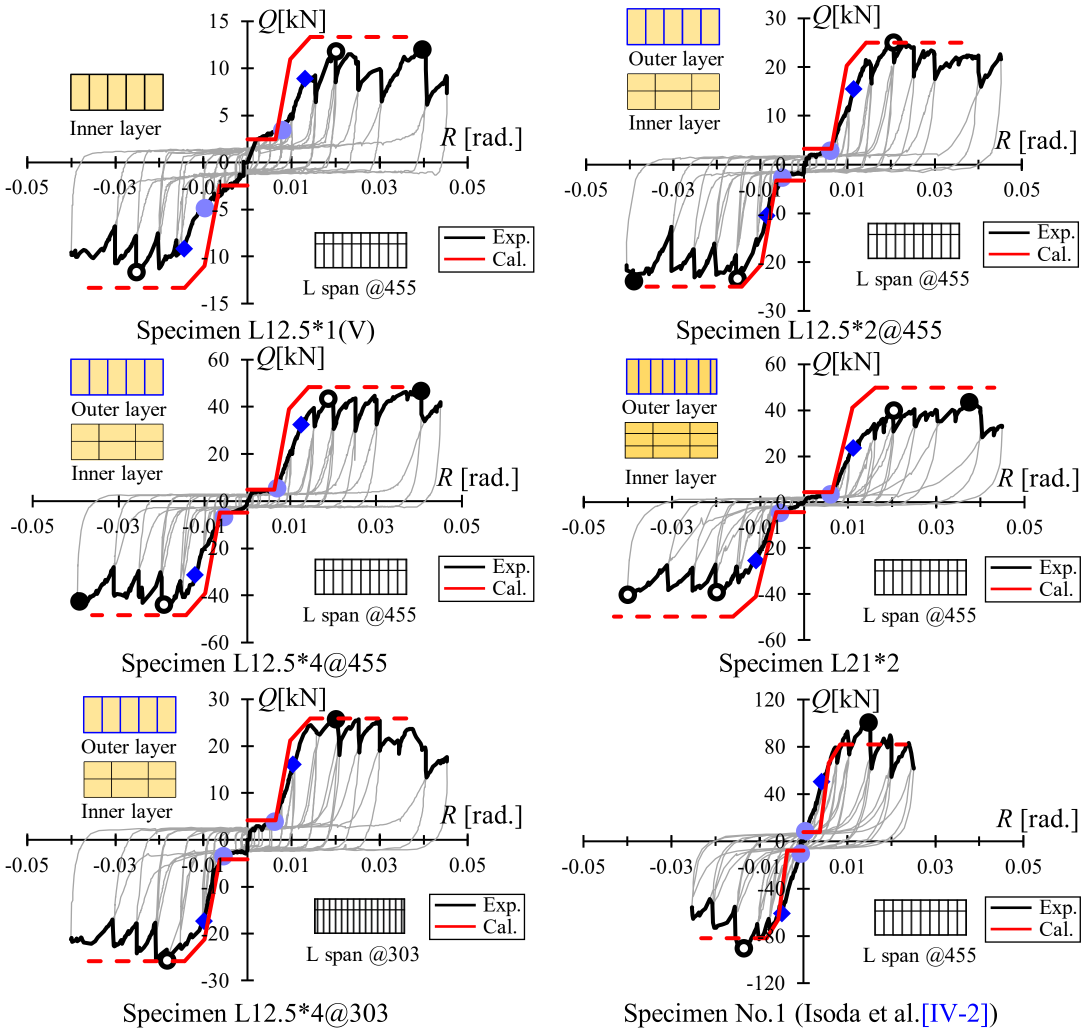

Specimen L12.5*1(V)

Specimen L12.5*2@455

Specimen L12.5*4@455

Specimen L21*2

Specimen L12.5*4@303

Specimen No.1 (Isoda et al.[IV-2])

Fig. AIV-4. verification of material test data board PA of [IV-1].

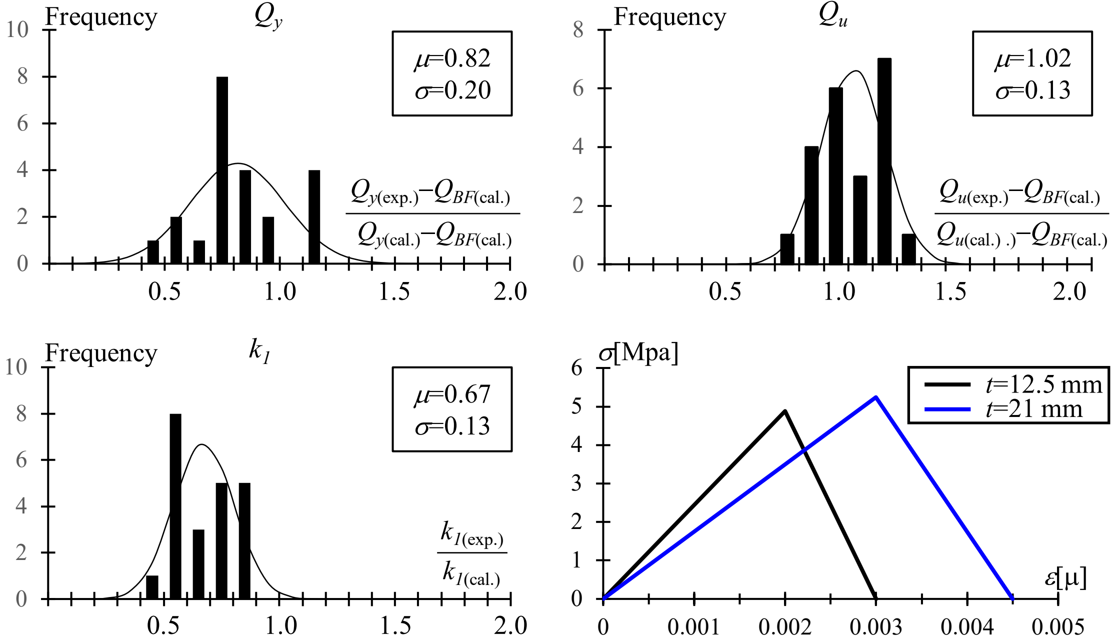

Fig. AIV-5. Parametrically analyses of board PA of [AIV-1].

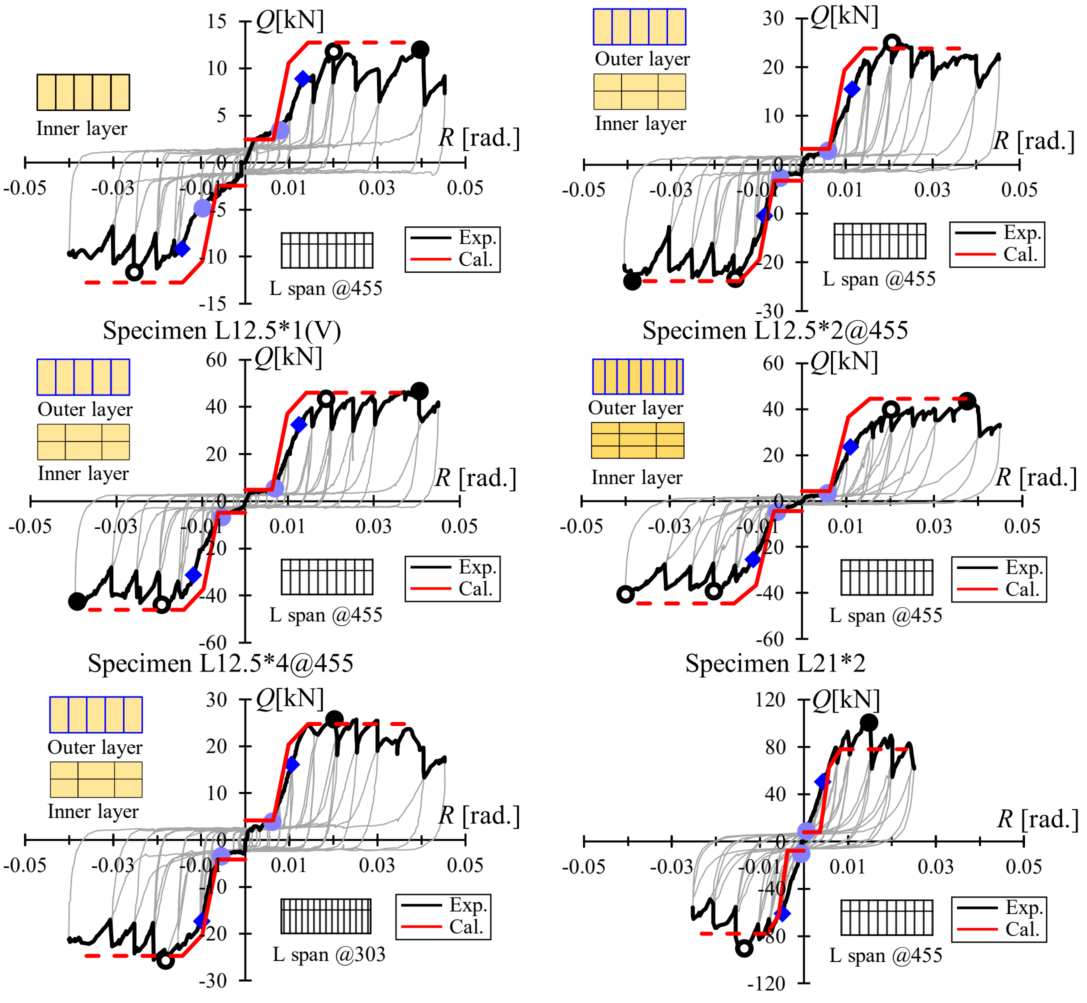

Specimen L12.5*1(V)

Specimen L12.5*2@455

Specimen L12.5*4@455

Specimen L21*2

Specimen L12.5*4@303

Specimen No.1 (Isoda et al.[IV-2])

Fig. AIV-6. verification of material test data board A of [IV-1].

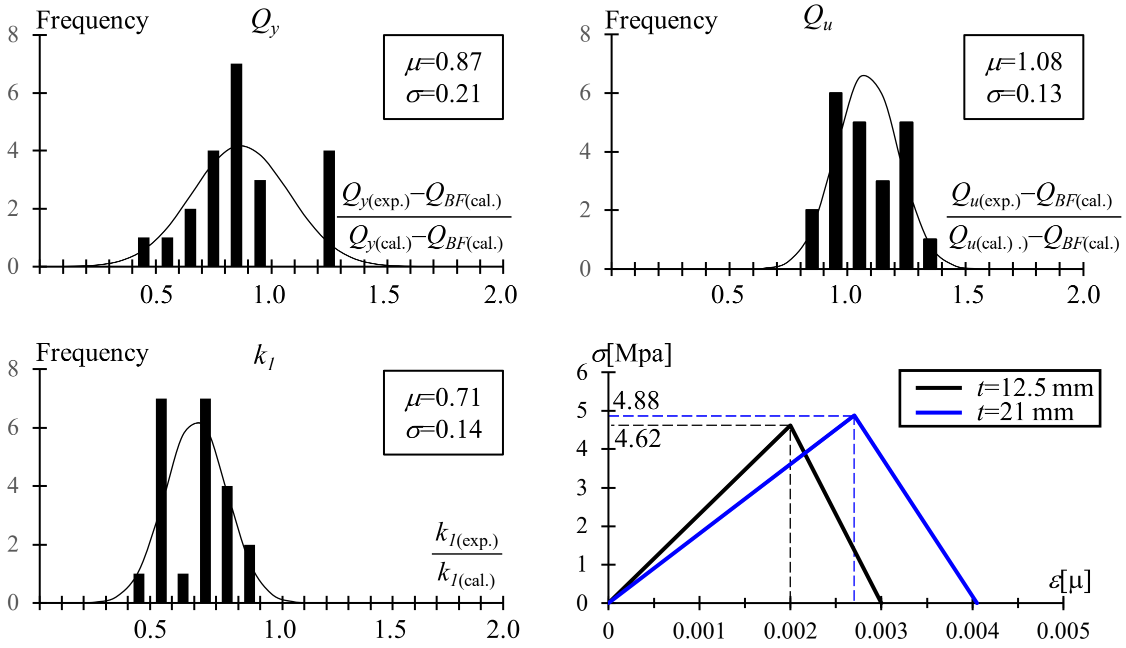

Fig. AIV-7. Parametrically analyses of board A of [IV-1].

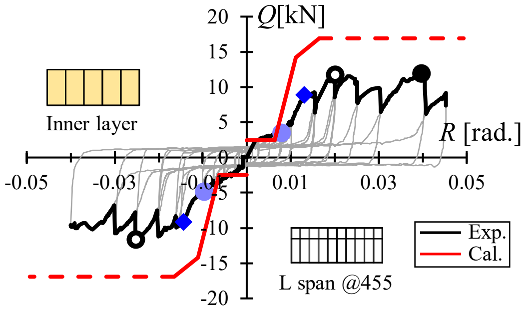

Specimen L12.5*1(V)

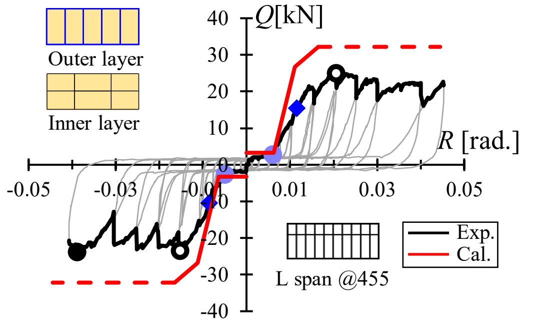

Specimen L12.5*2@455

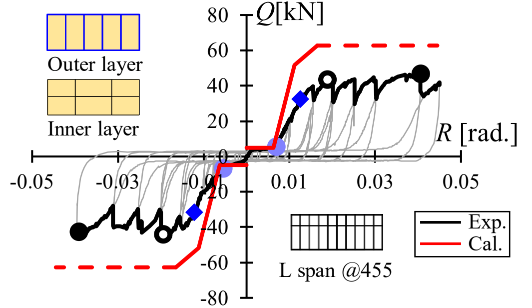

Specimen L12.5*4@455

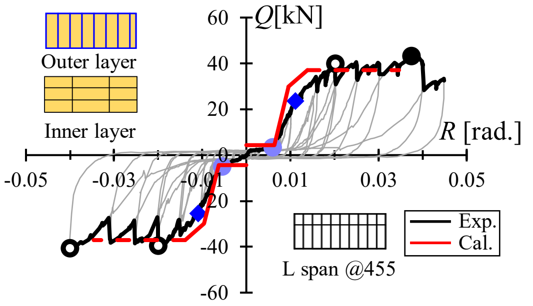

Specimen L21*2

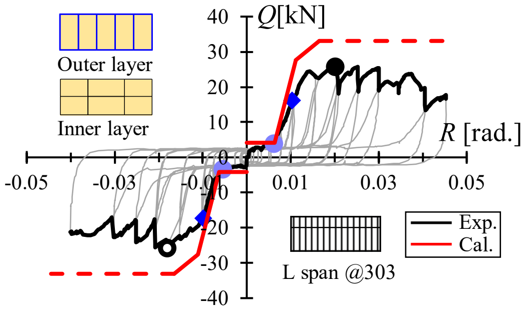

Specimen L12.5*4@303

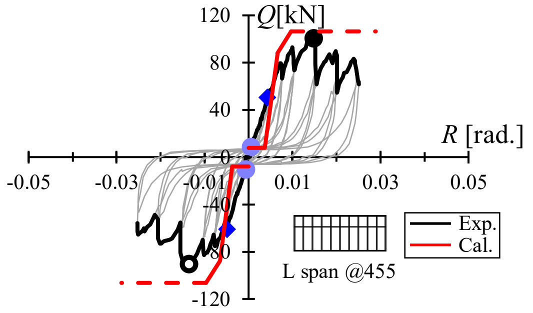

Specimen No.1 (Isoda et al.[IV-2])

Fig. AIV-8. verification of material test data board OB of [IV-1].

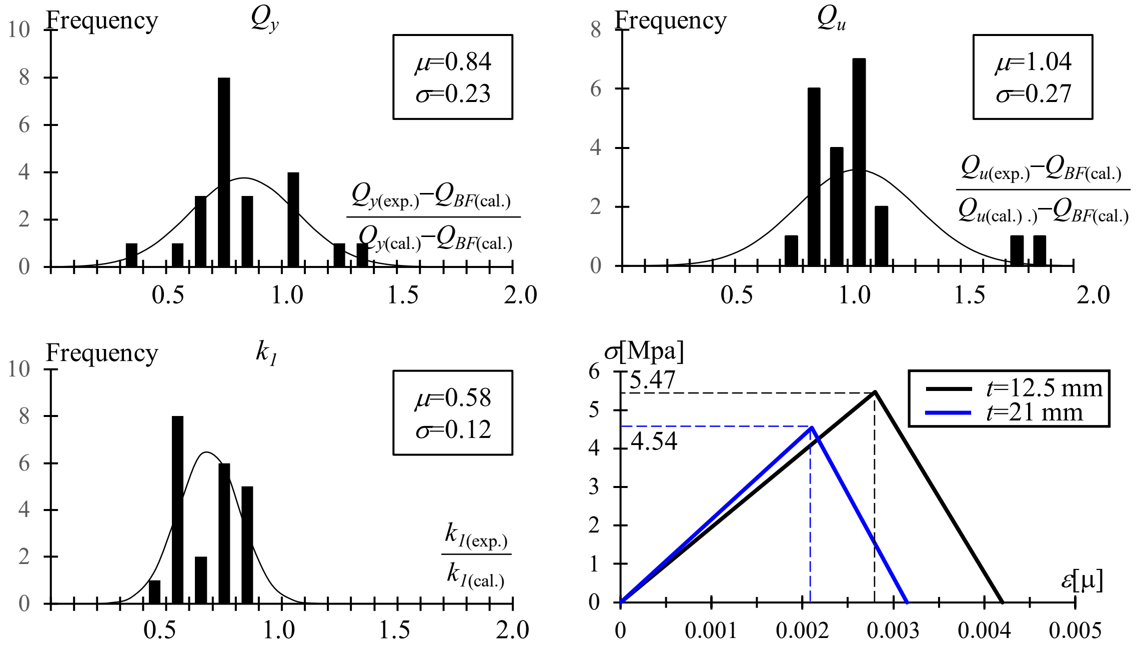

Fig. AIV-9. Parametrically analyses of board OB of [IV-1].

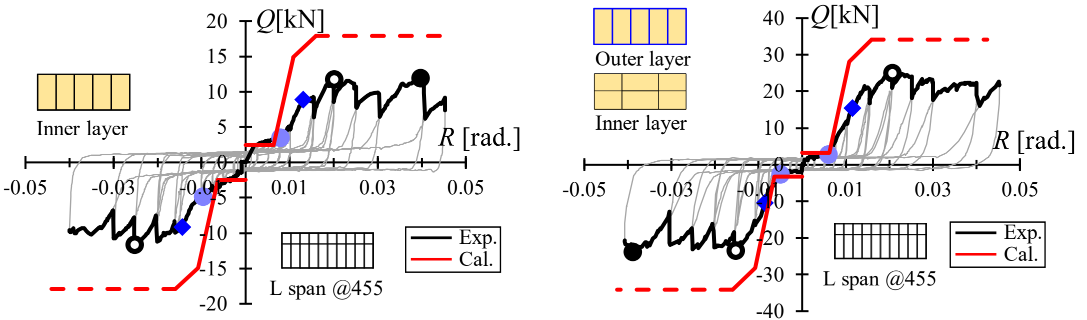

Specimen L12.5*1(V)

Specimen L12.5*2@455

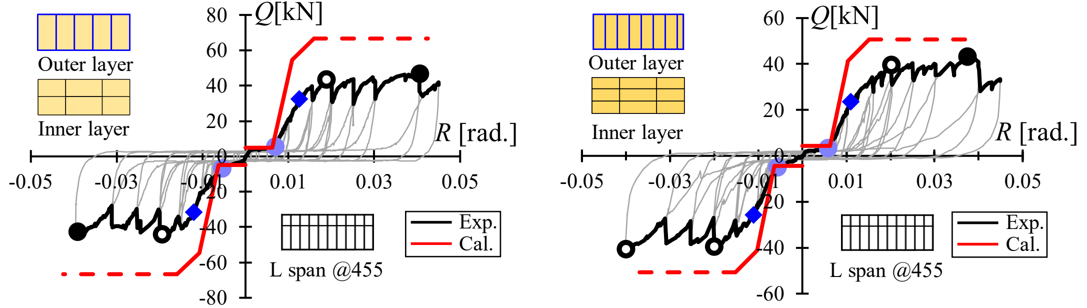

Specimen L12.5*4@455

Specimen L21*2

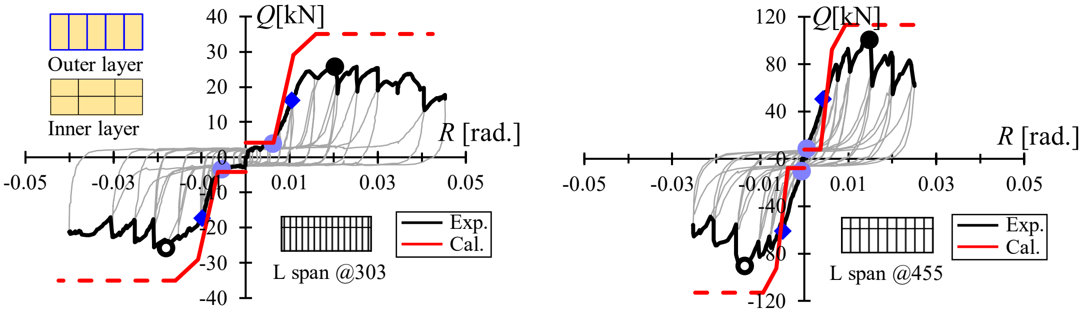

Specimen L12.5*4@303

Specimen No.1 (Isoda et al.[IV-2])

Fig. AIV-10. verification of material test data board PB of [IV-1].

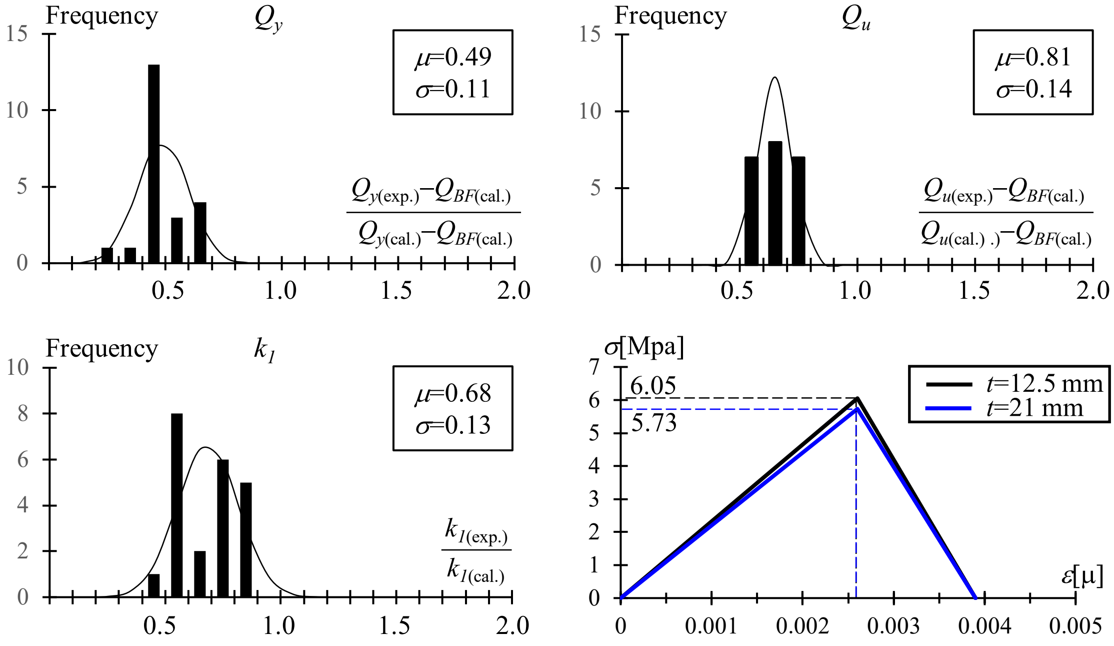

Fig. AIV-11. Parametrically analyses of board PB of [IV-1].

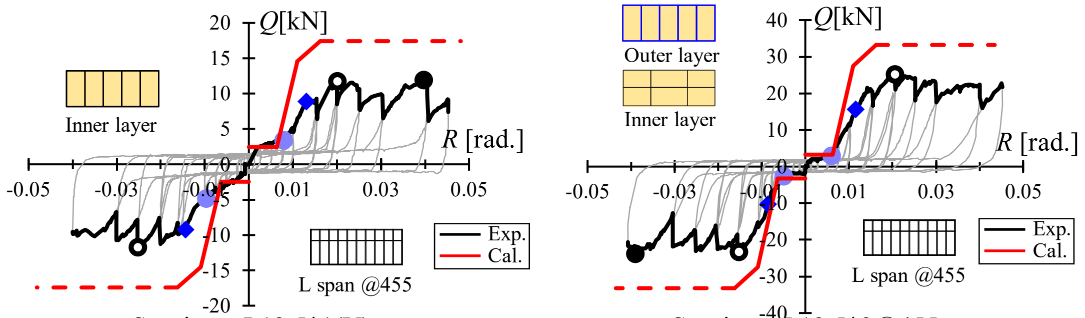

Specimen L12.5*1(V)

Specimen L12.5*2@455

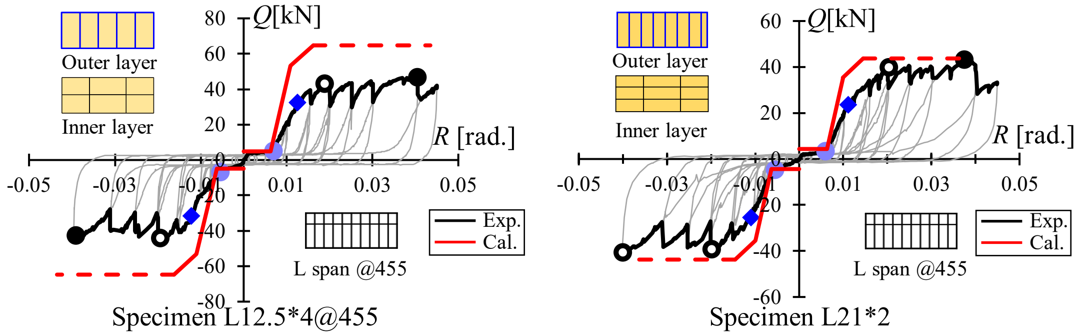

Specimen L12.5*4@455

Specimen L21*2

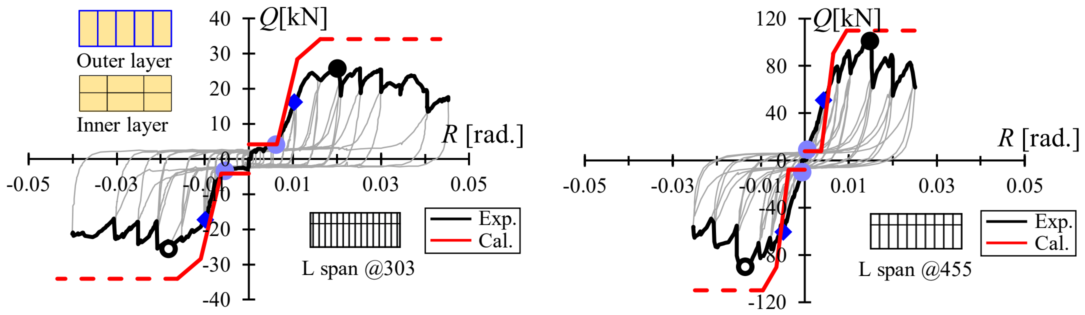

Specimen L12.5*4@303

Specimen No.1 (Isoda et al.[IV-2])

Fig. AIV-12. verification of material test data board B of [IV-1].

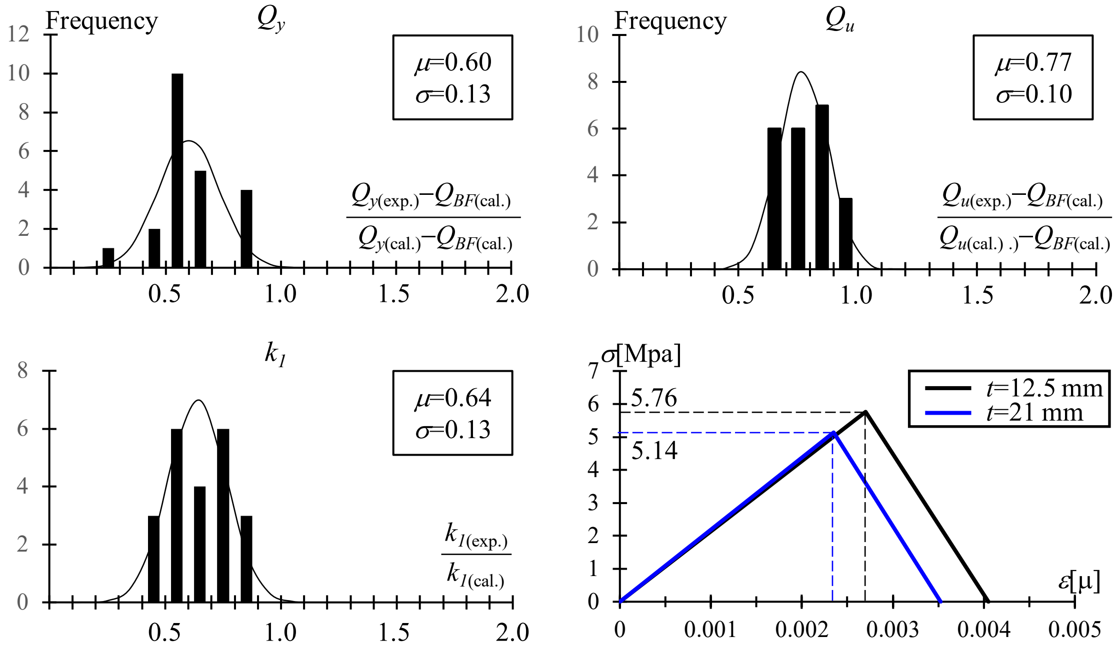

Fig. AIV-13. Parametrically analyses of board B of [IV-1].

In terms of the mean and standard deviation of the force and stiffness, the material test results of Company A are closer to 1 (i.e., the calculated value is closer to the experimental value). Considering the crisscross configuration of LGS walls, it is more appropriate to use the average value for evaluation.

Reference

[IV-1] Sato Y., Ogawa M., Hatori T., Motoyui S., Development of Reduction Method for Seismic Damage to LGS Partition Wall, Part6. Study on the material property of gypsum board. Academic proceedings of Architectural Institute of Japan (AIJ) annual national meeting, pp.1419-1420, Hokuriku, Japan; 2019. (in Japanese)

[IV-2] Isoda M., Oki Y., Tatsumi N., Kishiki S., Ishihara T., Behavior of LGS partition walls against in-plane relative displacements and out-of-plane inertial forces. Proceeding of constructional steel Vol.29, Japanese Society of Steel Construction, Tokyo, 2021. (In Japanese)

Appendix V

An analysis of a case study is conducted in order to compare the two research subjects in this study. To provide more specific design recommendations. The case–study building model is a four storey steel office building designed in accordance with Japanese building standard law [AV-1]. The plan of its standard floor is shown in Fig. AV-1. Considering the application range of masonry infill walls in this study, the shorter span is selected between column 2-B and 2-C of Fig. AV-1. With a 2850 mm length and 2850 mm height for the infill walls. Its structural frame information is listed in Table AV -1, the detail is shown in Fig. AV-2.

Fill the space with LGS partition and masonry infill, respectively. Based on Sato Y. et al. 's [AV-2] material tests, the LGS partition walls are assumed to be constructed of the same materials and in the same constructed method as in this study. For the masonry infills, the material strength of Emami's [AV-3]specimen with steel frame in Chapter 3 is used, where Young's modulus and bond strength are calculated according to Eqs. (AV-1) [AV-4] and (AV-2) [AV-5], which are described in detail in Section 3.4.1.It is worth noting that although the thickness of the gypsum board is only 50 mm, adding the width of its base frame of approximately 65 mm increases the thickness of the entire wall to 115 mm, which is considered to be the same thickness as the masonry wall used for comparison. Their details are recorded in Table AV-1 for LGS partition, and Table AV-2 for masonry infill.

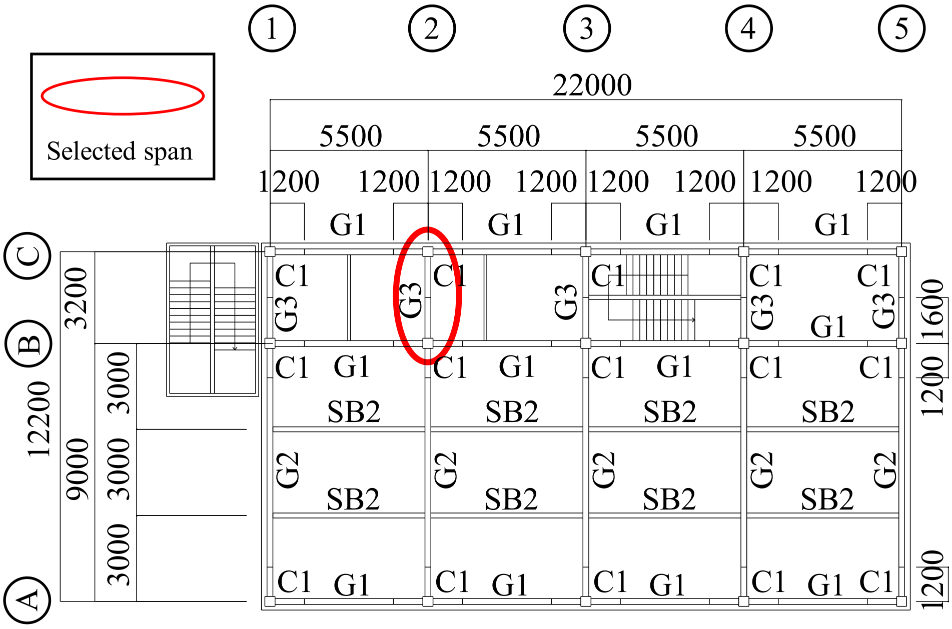

Fig. AV-1. Plan view of standard floor.

Table AV-1. Detail of the frame of the building.

Component ID	Shape	Material	Young’s modulus (N/mm^2)	Moment of inertia of area (cm^4)
G3	H-500×200×10×16	SN400B	205000	42400
C1	□-350×350×19	BCP325	205000	46800

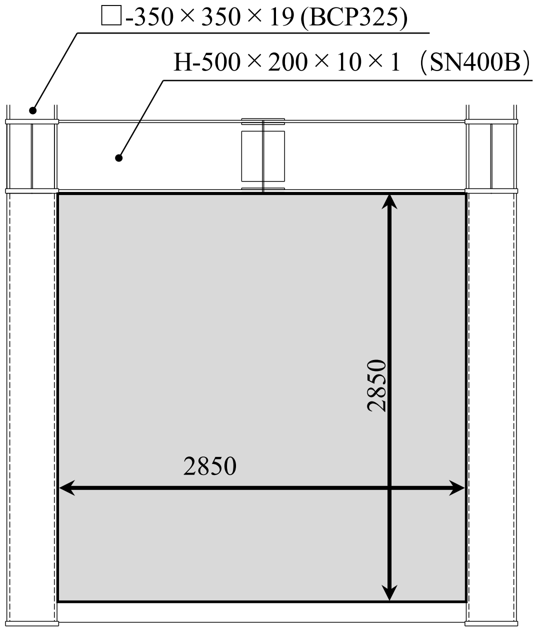

Fig. AV-2. Detail of the surrounding frame.

Table AV-2. Assumed properties of LGS partition

Assumed properties	
$L \times H$	2850×2850 mm^2
$t = t_B \times n$	$50 = 12.5 \times 4$ mm
c	5 mm
le	1365 mm
σ_y	4.6 MPa
E	2300 MPa

Table AV-3. Assumed properties of masonry infill

Assumed properties	
$L \times H$	2850×2850 mm^2
H/L	1
t	115 mm
σ_m	8.3 MPa
σ_M	9.5 MPa
E_M*	5225 MPa
τ_0*	0.4 MPa

*:Calculated results

$$\tau_0 = 0.0471 \times \sigma_m \qquad \text{(AV-1)}$$

$$E_M = 550 \times \sigma_M \qquad \text{(AV-2)}$$

The estimate envelope curves (Fig. AV-3) calculated by the material properties with the equations of the characterize points obtained in **Chapters 2** and **3**. Combined with the degree of damage of its corresponding story drift ratio. Taking the Japanese building seismic design limit of 1/200 rad. as example, the LGS wall is hardly damaged within the design limit due to the setting of clearance, and the wall can be used continually. In contrast, masonry infill is even susceptible to collapse at seismic limits. However, it can be seen that masonry infill exhibits higher initial stiffness. In view of this, it is considered that masonry infill is more suitable for use as seismic resistant elements. In addition, it is suggested to use stronger bricks and mortar to increase their initial stiffness, i.e. increase its resistance to deformation. On the other hand, if masonry infills are used as partition wall, some specific measures for the damage control are recommended such as set clearance between the panel and the frame. In this way, the contact between the frame and the panel is delayed, resulting in increased ductility.

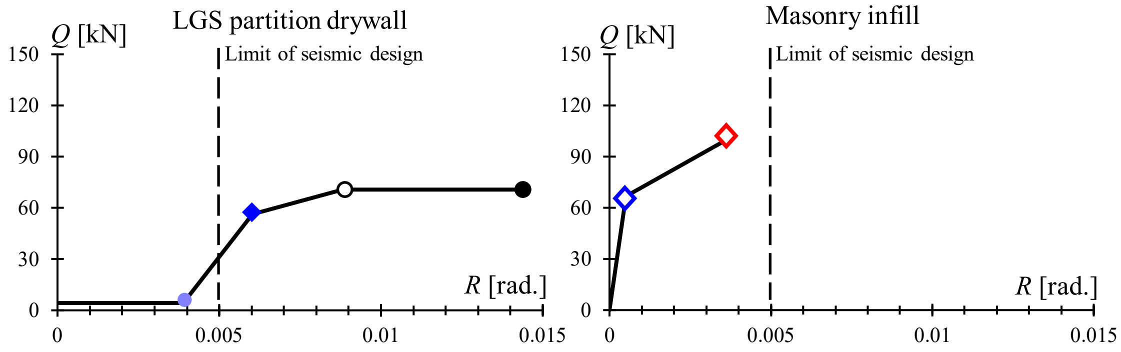

Fig. AV-3. Comparison between LGS partition and masonry infill.

Reference

[V-1] Japanese society of steel construction, わかりやすい鉄骨の構造設計, Gihodo Shuppan Co. Ltd., 2009. (in Japanese)

[V-2] Sato Y., Ogawa M., Hatori T., Motoyui S., Development of Reduction Method for Seismic Damage to LGS Partition Wall, Part6. Study on the material property of gypsum board. Aca demic proceedings of Architectural Institute of Japan (AIJ) annual national meeting, pp.1419-1420, Hokuriku, Japan; 2019. (in Japanese)

[V-3] S. Emami and M. Mohammadi, Effect of frame connection rigidity on the behavior of infilled steel frames, Earthquakes and Structures, Vol. 19, No. 4 (2020) 227-241 DOI: https://doi.org/10.12989/eas.2020.19.4.227

[V-4] G. H. Nalon, C. F. R. Santos, L. G. Pedroti, J. C. L. Ribeiro, G. S. Veriussimo and F. A. Ferreira, Strength and failure mechanisms of masonry prisms under compression, flexure and shear: Components' mechanical properties as design constraints, Journal of Building Engineering 28 (2020) 101038. https://doi.org/10.1016/j.jobe.2019.101038

[V-5] Kaushik, H. B., D. C. Rai, and S. K. Jain. 2007. "Stress-strain characteristics of clay brick masonry under uniaxial compression." J. Mater. Civ. Eng. 19 (9): 728–739. https://doi.org/10.1061/(ASCE)0899-1561(2007)19:9(728).

Publication related to this study

Peer-reviewed international journal

1) Zhe QU, Xiang FU, Shoichi KISHIKI, Yao CUI. Behavior of Masonry Infilled Chuandou Timber Frames Subjected to In-Plane Cyclic Loading. *Engineering Structures*, Volume 211, 15 May 2020, 110449.

2) 付翔、吉敷祥一、巽信彦、磯田充樹、軽量鉄骨下地間仕切り壁とコンクリートスラブの接合部に関する実験、鋼構造年次論文報告集第28巻 pp.496-502, 2020年11月.

3) Shoichi KISHIKI, Xiang FU, Nobuhiko TATSUMI. Seismic Performance Evaluation of Non-structural Light-gauge Steel Frame Drywall Partition Subjected to In-Plane Cyclic Loading. *Thin-walled structures*. (Submitted)

4) Xiang FU, Shoichi KISHIKI. Seismic Performance Evaluation of Ductile Frame with Masonry Infill Subjected to In-Plane Cyclic Loading. *Structures*. (Preparing for submission)

Peer-reviewed international conference paper
(poster or oral presentation)

1) X. FU, Z. QU, S. KISHIKI, Y. CUI, Q. Tang. Cyclic loading test of masonry infilled Chuandou timber frames for residences in South China, 11th U.S. National Conference on Earthquake Engineering(11NCEE), ID 1553, Los Angeles, United States of America.
2) X. FU, Z. QU, S. KISHIKI, Y. CUI. Cyclic loading test of Chuandou timber frames with masonry infill for residential house in south China, 5th Pacific Timber Engineering Conference (PTEC 2019), Brisbane, Australia.

Domestic conference paper

(Oral presentation)

1) 付翔，吉敷祥一，曲哲，崔瑶. Cyclic loading test of masonry infilled Chuandou timber frames in China (part 1~2), 日本建築学会大会学術講演梗概集（関東支部）pp.325-332, 2018 年 3 月.

2) 付翔，吉敷祥一，曲哲，崔瑶. Cyclic loading test of masonry infilled Chuandou timber frames in China (part 3~4), 日本建築学会大会学術講演梗概集 pp.513-516, 2018 年 9 月.

3) 付翔，吉敷祥一. Comparison study of seismic behavior between different types of traditional timber frame with masonry infill structure (part 1), 日本建築学会大会学術講演梗概集（関東支部）pp. 293-296, 2019 年 3 月.

5) 付翔，吉敷祥一. Cyclic loading test of masonry infilled Chuandou timber frames in China (part 5), 日本建築学会大会学術講演梗概集 pp.167-168, 2019 年 9 月.

6) 付翔，吉敷祥一，巽信彦　など. 軽量鉄骨下地乾式間仕切り壁の地震時損傷抑制に関する研究(その 15-17) , 日本建築学会大会学術講演梗概集 pp.1215-1220, 2020 年 9 月.

7) 付翔，吉敷祥一，巽信彦. Behavior of Light Gauge Steel (LGS) Partition Wall Subjected to In-plane Cyclic Loading (part 1), 日本建築学会大会学術講演梗概集（関東支部）pp.173-176, 2021 年 3 月.

8) 付翔，吉敷祥一，巽信彦　など. 軽量鉄骨下地乾式間仕切り壁の地震時損傷抑制に関する研究（その 23~24), 日本建築学会大会学術講演梗概集, 2021 年 9 月.